Advances in Concurrent Motion and Field-Inhomogeneity Correction in Functional MRI

by

Teck Beng Desmond Yeo

A dissertation submitted in partial fulfillment
of the requirements for the degree of
Doctor of Philosophy
(Electrical Engineering: Systems)
in The University of Michigan
2008

Doctoral Committee:

Professor Jeffrey A. Fessler, Co-chair
Assistant Research Professor Boklye Kim, Co-chair
Professor Charles R. Meyer
Professor Thomas L. Chenevert
Assistant Professor Clayton D. Scott

To my parents, Robert Kim Chye Yeo and Julia Khin Neo Lee, my wife, Patricia Yoke Hiang Loh, and our little girl, Skylar.

ACKNOWLEDGEMENTS

I am glad I am finally able to officially thank the wonderful people who have been indispensable in the completion of my doctorate. I wish to thank my advisors, Professors Jeffrey Fessler and Boklye Kim, for their mentorship, encouragement, and kindness. As my EECS research advisor, Prof. Fessler has been nothing short of inspirational, not only because of his brilliant technical guidance, but also because of his commitment to his students. I recall him driving to my apartment once to help review my qualifying examination slides on a day when the buses stopped running unexpectedly. It is difficult to forget something like that. Prof. Kim has been a stellar example of maintaining balance between technical research and clinical relevance. She has provided excellent alternative perspectives of different technical challenges, and has managed to steer me away from developing technical tunnel vision. I am also very grateful to Prof. Chuck Meyer for having agreed to interview me five and a half years ago. I would never have had the opportunity to study in Ann Arbor if he and Prof. Kim had not taken a chance on a bright-eyed student looking to transit into a different research field. I would also like to thank Prof. Thomas Chenevert for his advice, clinical insights, and for being a great source of support for all our MRI scans, especially those in the wee hours of the day. I would also like to express my sincere gratitude to Prof. Clayton Scott for his invaluable time and advice in reviewing my dissertation, and to Prof. Douglas Noll for his very helpful and timely counsel.

I am thankful to colleagues and friends including Roshni Bhagalia, Hyunjin Park, Bing Ma, Ted Way, Somesh Srivastava, Saradwata Sarkar, Peyton Bland, Gary Laderach, Ramakrishnan Narayanan, Kalyanakrishnan Vadakkeveedu, and Mukundakumar Rajukumar for the good-spirited camaraderie and interesting hallway discussions.

I am very grateful to my parents who selflessly endured our years of absence from Singapore, while encouraging us to pursue our dreams. I would also like to thank my wife, Patricia Loh, for standing steadfastly with me through our good and bad times. You are truly my better half. Last, but most importantly, I would like to thank God for giving a *kampong* (village) boy opportunities that he could only dream of, and the strength and ability to harness them.

This work was supported in part by the National Institute of Health grants 1P01 CA87634 and 8R01 EB00309.

TABLE OF CONTENTS

LIST OF FIGURES

Figure

LIST OF TABLES

Table

ABSTRACT

ADVANCES IN CONCURRENT MOTION AND FIELD-INHOMOGENEITY CORRECTION IN FUNCTIONAL MRI

by

Teck Beng Desmond Yeo

Co-Chairs: Jeffrey A. Fessler and Boklye Kim

Head motion and static magnetic field (B_0) inhomogeneity are two important sources of image intensity variability in functional MRI (fMRI). Ideally, in MRI, any deviation in B_0 homogeneity in an object occurs only by design. However, due to imperfections in the main magnet and gradient coils, and, magnetic susceptibility differences in the object, undesired B_0 deviations may occur. This causes geometric distortion in Cartesian EPI images. In addition to spatial shifts and rotations of images, head motion during an fMRI experiment may induce time-varying field-inhomogeneity changes in the brain. As a result, correcting for motion and field-inhomogeneity effects independently of each other with a static field map may be insufficient, especially in the presence of large out-of-plane rotations. Our primary concern is the correction of the combined effects of motion and field-inhomogeneity induced geometric distortion in Cartesian EPI fMRI images. We formulate a concurrent field-inhomogeneity with map-slice-to-volume motion correction, and develop a motion-robust dual-echo bipolar gradient echo static field map estimation method. We also propose and evaluate a penalized weighted least squares approach to

dynamic field map estimation using the susceptibility voxel convolution method. This technique accounts for field changes due to out-of-plane rotations, and estimates dynamic field maps from a high resolution static field map without requiring accurate image segmentation, or the use of literature susceptibility values. Experiments with simulated data suggest that the technique is promising, and the method will be applied to real data in future work.

In a separate clinical fMRI project, which is independent of the above work, we also formulate a current density weighted index to quantify correspondence between electrocortical stimulation and fMRI maps for brain presurgical planning. The proposed index is formulated with the broader goal of defining safe limits for lesion resection, and is characterized extensively with simulated data. The index is also computed for real human datasets.

CHAPTER 1

Introduction

Functional magnetic resonance imaging (fMRI) is a dynamic imaging method that is widely used to map the function of the human brain non-invasively. In a typical fMRI experiment, the subject is scanned with a fast MR imaging protocol while subjected to a time-controlled set of stimuli. Image intensity differences over time, induced by local magnetic susceptibility changes due to cerebral blood flow (CBF) changes, are analyzed statistically to determine if a region of the brain is activated in response to the given stimuli. Since fMRI is essentially a dynamic study of this Blood Oxygenation Level Dependent (BOLD) contrast, fast MR imaging protocols must be used to achieve adequate temporal resolution.

Echo-planar imaging (EPI) [1] is a group of fast imaging protocols that is commonly used in fMRI studies. A popular protocol in this family is the single-shot Cartesian blipped EPI protocol that acquires almost uniformly spaced *k*-space samples in a Cartesian grid, which allows for efficient image reconstruction using the inverse fast Fourier transform (FFT). Unfortunately, in the presence of inhomogeneity in the main magnetic field B_0, artifacts such as geometric distortion [2] and blurring are observed in blipped EPI and spiral EPI images respectively when an inverse FFT is applied directly to the re-gridded *k*-space samples for image reconstruction. This is due to the inadvertent field-inhomogeneity induced phase accrual in the MR signal during the long readout time following every radio frequency (RF) pulse. The main sources of field-inhomogeneity include eddy currents induced by the switching gradient fields, imperfect gradient fields, main magnet imperfections and the interaction of B_0 at the boundaries of tissues of different magnetic susceptibility values. The latter is particular significant because it is object-specific and may change non-linearly with object motion. In addition to geometric distortion and blurring, field-inhomogeneity also causes signal loss due to in-plane and through-plane intra-voxel dephasing. Another artifact that is often ignored is the susceptibility induced slice profile warp which, if severe enough, can map activated voxels onto incorrect slice locations in an anatomically correct structural scan and thus yield misleading results.

1.1 Thesis Outline

Parts of this thesis focus on susceptibility-induced geometric distortion correction for a single shot blipped EPI protocol. To perform geometric distortion correction, some form of field-inhomogeneity map is often assumed to be available [2-8]. A field map is said to be static if it is acquired at only one time point in the fMRI experiment and thus does not track the field-inhomogeneity changes when the head moves. A dynamic field map is a set of temporal field maps that tracks the field-inhomogeneity changes with head motion and is usually acquired together with the EPI data [9,10]. A static field map may suffer from errors induced by motion between the acquisitions of the two gradient echo datasets required to estimate the field map. The dual-echo fast gradient recalled echo (DEFGRE) field map acquisition method [11] in Chapter 3 attempts to reduce field map estimation errors due to such motion between the two echo signals.

Head motion is another source of image intensity variation that can severely curtail activation detection accuracy. Motion correction techniques generally use an affine transformation model, of which the rigid body model is a special case, or a non-linear transformation model, which is computationally more expensive. If geometric distortion correction for blipped EPI is not performed, rigid body registration techniques generally do not have sufficient degrees of freedom to accurately reposition all the EPI slices into a structural scan, and thus, non-linear registration techniques are required. In addition, head motion may change the angles between B_0 and tissue interfaces which in turn can cause the field-inhomogeneity to vary non-linearly with head motion. Thus, correcting for head motion and field-inhomogeneity separately with only a static field map may yield significant errors. The concurrent field map and map-slice-to-volume motion correction (CFMMSV) method [13] in Chapter 4 attempts to estimate a pseudo-dynamic field map to perform geometric distortion correction and uses map-slice-to-volume (MSV) motion correction parameters to compute an updated field map from a static field map. This correction method may have limitations for large out-of-plane rotations and thus, in Chapter 5, we propose a novel penalized weighted least squares approach to field map estimation to account for such motion. We present preliminary results of the proposed approach to estimating dynamic field maps from a measured high resolution 3D static field map using a statistical version of the deterministic susceptibility voxel convolution method. The proposed method does not require head image segmentation, or the associated assignment of literature magnetic susceptibility values to voxels of the brain.

In Chapter 6, we propose a current density weighted index to quantify the correspondence between fMRI and electrocortical stimulation (ECS) maps for brain lesion presurgical planning.

ECS is the current gold standard for brain functional mapping in presurgical planning, but it is highly invasive. The definition of a systematic and physiologically relevant correspondence index is a first step to evaluating fMRI as a non-invasive alternative to ECS for presurgical planning. In this work, various techniques, including non-linear registration, rigid body slice-to-volume registration, fMRI time series analysis, and subdural electrode current density computation, are employed to facilitate the definition of the proposed correspondence index.

In summary, Chapters 1 and 2 of this report provide the necessary background information for the remaining chapters. Chapters 3 and 4 describes work already done [11,13], while Chapters 5 and 6 present preliminary results with suggestions for future work. Fig. 1.1 provides an organizational overview of this thesis.

1.2 Contributions

The main contributions of this work are:

- The problem formulation and development of an affine phase error correction technique that facilitates motion robust static field map estimation using a dual-echo bipolar gradient recalled echo protocol [11]. Validation of the technique is performed using phantom and human data.
- The development of a concurrent motion and field inhomogeneity correction framework for EPI time series images [13]. The concurrent field-map MSV (CFMMSV) method employs iterative field-corrected quadratic penalized least squares (QPLS) image reconstruction [5] followed by a field map approximation procedure to enhance the MSV rigid body motion-correction scheme, therefore accounting for field inhomogeneity changes with inter-slice head motion.
- The formulation of a novel regularized 3D image restoration approach to dynamic susceptibility map estimation by solving the inverse susceptibility voxel convolution problem. Using realistically simulated noisy 3D field maps of a spherical air compartment in water, preliminary results suggest that the proposed method may yield more accurate dynamic field map estimates compared to simpler methods, while requiring less prior information. In fMRI, this may potentially improve dynamic field map estimates and hence, geometric distortion correction accuracy.
- The definition and evaluation of a new set of current density weighted indices to quantify the correspondence between subdural electrocortical stimulation and fMRI maps [58]. Simulated datasets are used to characterize the indices in detail, after which, they were computed for several patient datasets.

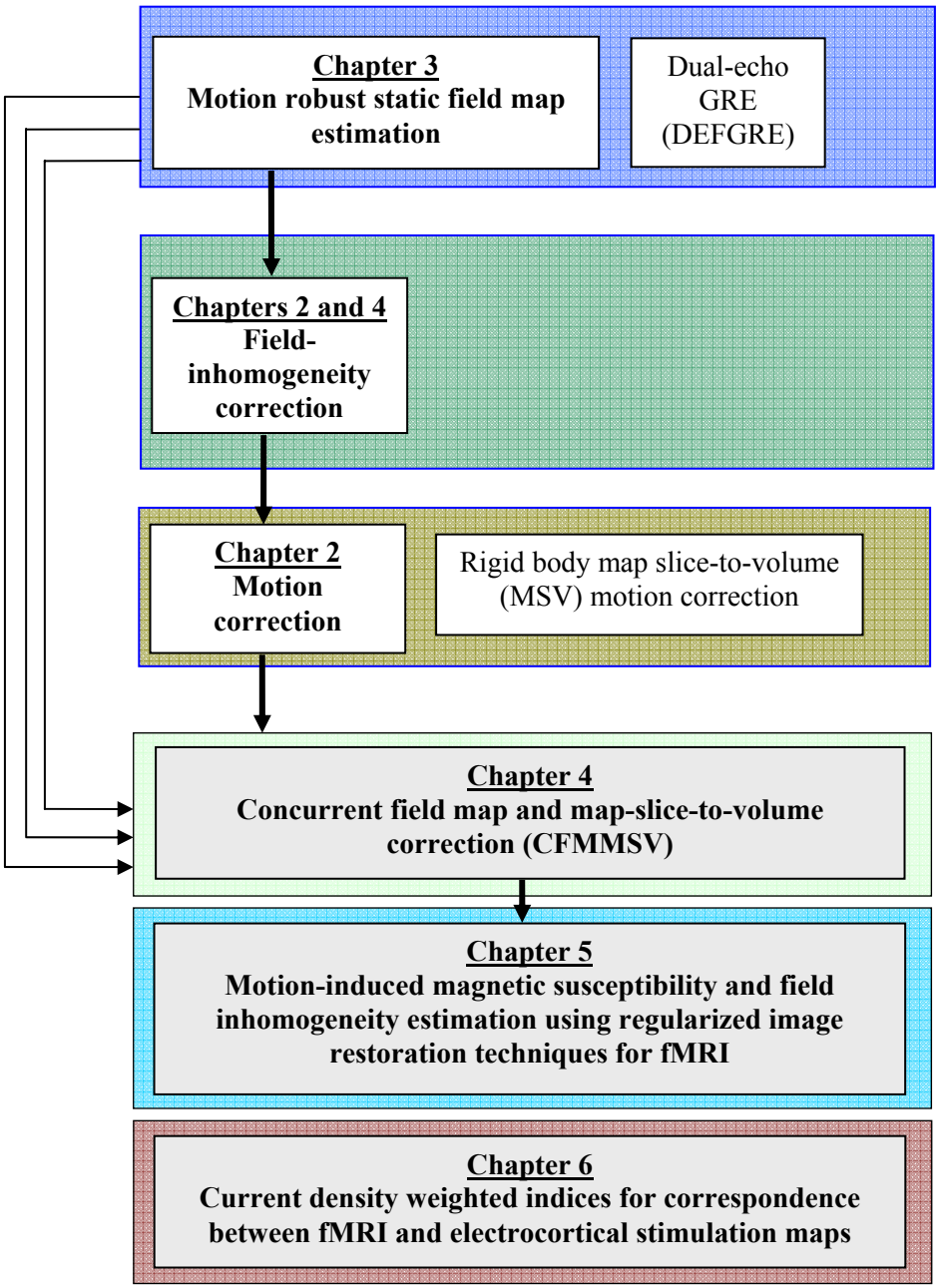

Figure 1.1: Organizational overview of this thesis with respect to a field-inhomogeneity and motion correction framework for fMRI. Chapter 6 is independent of previous chapters.

CHAPTER 2

Background

2.1 MRI Physics and Data Acquisition

An MR image is a map of an object's spatially varying net transverse (*x*-*y* plane component) magnetization generated by atomic nuclei that exhibit the nuclear magnetic resonance (NMR) phenomenon. The hydrogen nucleus, which is abundant in human soft tissue, is the predominant NMR-active nucleus imaged in brain MR images. The NMR phenomenon occurs when the NMR-active nucleus is placed in an external magnetic field, B_0, and excited by an applied RF pulse B_1 that is orthogonal to B_0. An NMR-active nucleus spins and behaves like a bar magnet with a small magnetic field referred to as the magnetic moment, $\vec{\mu}$. A nucleus-specific gyromagnetic ratio γ constant quantifies the ratio of the nucleus' angular momentum to its magnetic moment.

A hydrogen nucleus (single proton) placed in a homogenous magnetic field, B_0 is magnetized and will align itself either parallel (low energy state) or anti-parallel (high energy state) to B_0. Besides spinning on its own axis, each proton will also precess or rotate about the B_0 axis like a spinning top at the Lamor frequency, ω, as shown in Fig. 2.1 and described by Eq. (2.1).

$$\omega = \gamma B_0 \tag{2.1}$$

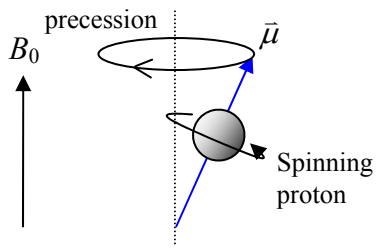

Figure 2.1: Single proton precessing in a B_0 magnetic field and spinning about its own axis.

The aggregate sum of the magnetic moments of the nuclei in a closed volume shown in Fig. 2.2 form the net magnetization, $\vec{M}$. At thermal equilibrium without the RF pulse, the spins do not precess in phase and thus cancel out each others transverse components. Thus $\vec{M}$ does not precess and is aligned with B_0 as shown in Fig. 2.2.

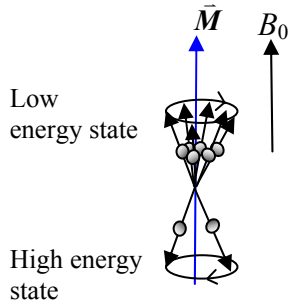

Figure 2.2: Distribution of proton energy states when a group of protons are placed in a magnetic field B_0

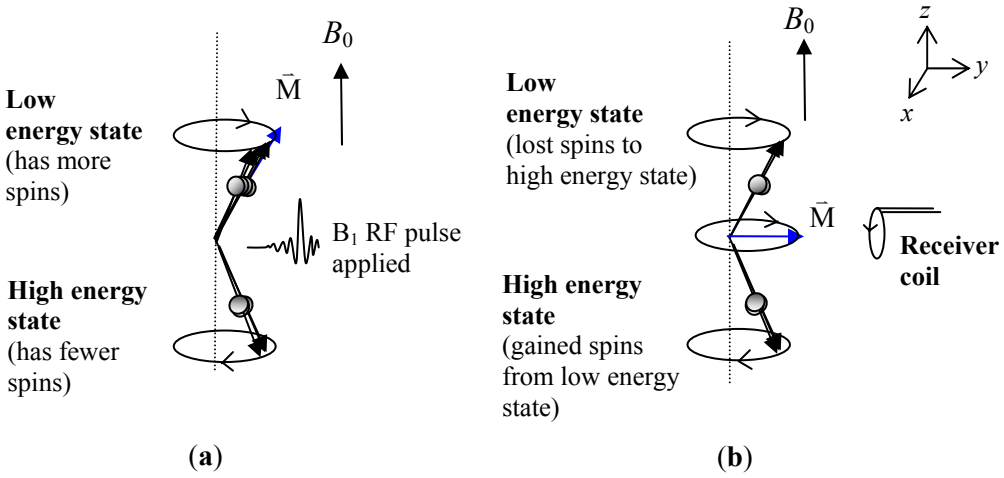

Figure 2.3: Net magnetization, $\vec{M}$ is tipped 90º downwards and precesses after applying a 90º RF excitation pulse. (**a**) Spins begin to precess in phase when B_1 is just applied. $\vec{M}$ starts to tip downwards and precesses. (**b**) $\vec{M}$ tips 90º downwards and precesses after 90º RF pulse is removed. Receiver coil measures induced voltage (MR signal).

When an RF pulse oscillating at the proton Lamor frequency is applied perpendicular to B_0, all proton spins begin to precess in phase with each other. Some spins in the low energy state make a transition into the higher energy state by absorbing energy from the RF pulse and this causes the net magnetization to tip towards the transverse plane. This is the NMR phenomenon. An αº RF pulse is one that has sufficient energy to tip $\vec{M}$ by αº. Fig. 2.3 shows the net magnetization, $\vec{M}$, after applying a 90º RF pulse to a group of protons. The precessing net

transverse magnetization $\vec{M}_{xy}$ is used to induce a voltage across a receiver coil according to Faraday's Law of Induction as shown in Fig. 2.3(b). The induced voltage constitutes the measured MRI signal $s(t)$.

After the RF pulse is removed, three main processes cause the received signal $s(t)$ to decay with time: spin-lattice energy loss caused by thermal perturbations (characterized by T_1), dephasing due to spin-spin interactions (characterized by T_2) and field-inhomogeneity induced dephasing (characterized by T_2^*). Assuming the field-inhomogeneity has a Lorentzian distribution, the signal decays with a time-constant T_2^* where $T_2^* = 1/T_2 + 1/T_{\Delta B}$ and $T_{\Delta B} \approx (\gamma \Delta B)^{-1}$. $T_{\Delta B}$ is the time-constant for the decay that occurs due to magnetic field-inhomogeneity ΔB. Field-inhomogeneity is often expressed in parts per million of the main magnetic field, i.e. $\Delta B_{ppm}=(\Delta B/B_0)*10^6$), and usually varies spatially.

Spatial localization in MRI is typically achieved by applying magnetic field gradients in three orthogonal directions to encode spatial information about the object as shown in Fig. 2.4.

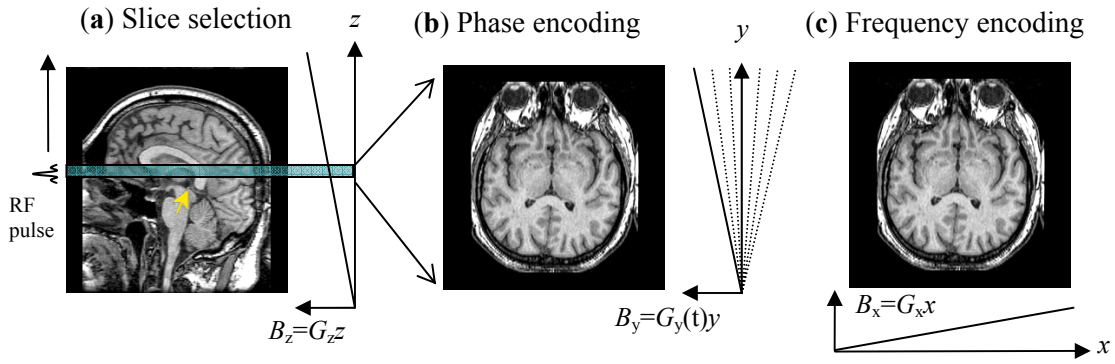

Figure 2.4: (**a**) Slice selection gradient G_z, (**b**) phase encode gradient strength $G_y(t)$ varies for different readout cycles, (**c**) readout gradient G_x constant for readout cycles.

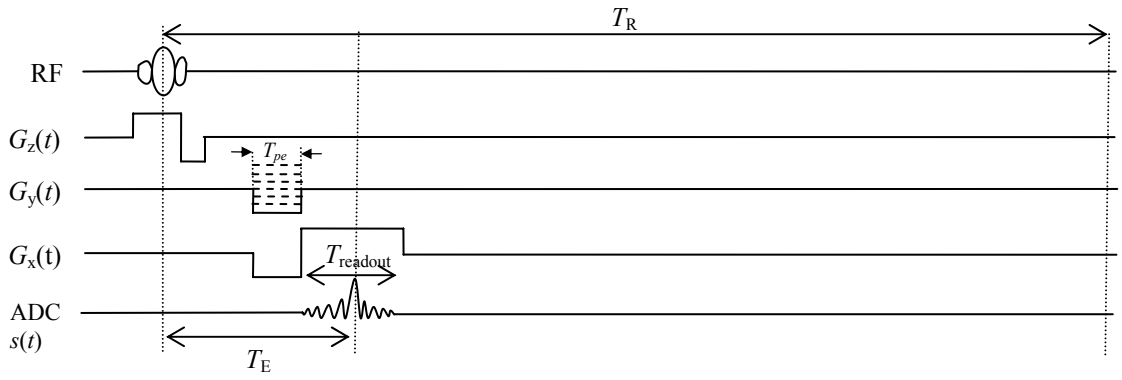

Figure 2.5: Basic gradient echo pulse sequence.

As an example, a basic multi-slice gradient echo pulse sequence is shown in Fig. 2.5. A slice-selection gradient $G_z(t)$ is first applied to set up a linear Lamor frequency variation in the z direction as shown in Fig. 2.5. A B_1 pulse with a bandwidth that covers the Lamor frequency range of the slice of interest is then applied. All subsequent data measurements pertain only to this slice. After a slice has been selected, a phase encode field gradient $G_y(t)$ is applied in the y direction for T_{pe} seconds. This causes a linearly varying spin phase accrual $\left[\gamma \int_0^{T_{pe}} G_y(\tau)d\tau\right] y$ in the y direction. The term $\gamma \int_0^{T_{pe}} G_y(\tau)d\tau$ is also known as the y-direction spatial frequency, $k_y(t)$. The gradient strength of $G_y(t)$ changes for each cycle of the pulse sequence so that data at different values of $k_y(t)$ can be measured. No signal is read during the application of the phase encode pulse $G_y(t)$. For each readout cycle with a constant $G_y(t)=G_y$, k_y is just $\gamma G_y T_{pe}$ cycles/ mm.

Following the phase encode pulse, a readout pulse $G_x(t)$ is applied during which the signal $s(t)$ is read off the receiver coil. A constant $G_x(t)$ pulse causes the Lamor frequency to vary linearly with x. As time passes, the phase accrual per unit length in the x direction $k_x(t) = \gamma \int_0^t G_x(\tau)d\tau$ gets larger. Physically, the net magnetization gets rotated by $e^{-jk_x(t)x}$ for each value of x at time t The MR signal $s(t)$, which is the sum of all the rotated spins' magnetization at time t, is sampled for various values of $k_x(t)$ as t increases. After the signal is acquired, the spins are allowed to relax for T_R seconds before the next RF pulse is applied. Recall that the Fourier transform $F(\omega)$ of a one dimensional function $f(x)$ can be viewed as a weighted integral of $f(x)$ where the weights are spatially linear phase terms $e^{-j\omega x}$. In other words, the Fourier transform at a specific frequency ω_i is the integral over x of $f(x)$ rotated by a spatially linear phase term $e^{-j\omega_i x}$. Since this is what happens physically to the magnetization when linear localization gradients are applied, the MR signal $s(t)$ or $s(k_x(t),k_y(t))$ of an infinitely thin slice in the z direction can be expressed as the Fourier transform of the imaged object $f(x,y)$ with spatial frequencies $k_x(t)$ and $k_y(t)$,

$$s(t) = s(k_x(t),k_y(t)) = \int_{-\infty}^{\infty}\int_{-\infty}^{\infty} f(x,y)e^{-j2\pi(k_x(t)x+k_y(t)y)}\,dxdy\,. \qquad (2.2)$$

The map of k_x and k_y (and k_z for 3D imaging) is known as k-space in MRI literature. The relationship between t, $k_x(t)$ and $k_y(t)$ is expressed in the k-space trajectory, which shows the

chronological order in which samples of *k*-space $s(k_x(t), k_y(t))$ are acquired. The *k*-space trajectory is determined by how the spatial localization gradients are applied.

2.2 Cartesian Blipped EPI in Functional MRI

Fig. 2.6 shows the *k*-space trajectory of the basic gradient echo pulse sequence of Fig. 2.5 and the blipped gradient echo EPI pulse sequence. Gradient echo EPI yields images that are sensitive to local susceptibility changes due to blood oxygenation level variations in fMRI experiments. However, in the presence of macroscopic field-inhomogeneity, especially that induced by magnetic susceptibility differences at tissue boundaries, the longer readout time $T_{readout}$ in EPI (typically about 30-100 ms) induces significant levels of undesirable phase accrual. If uncorrected, the extra phase accrued leads to geometric distortion in the reconstructed EPI images which will yield incorrect fMRI activation detection results.

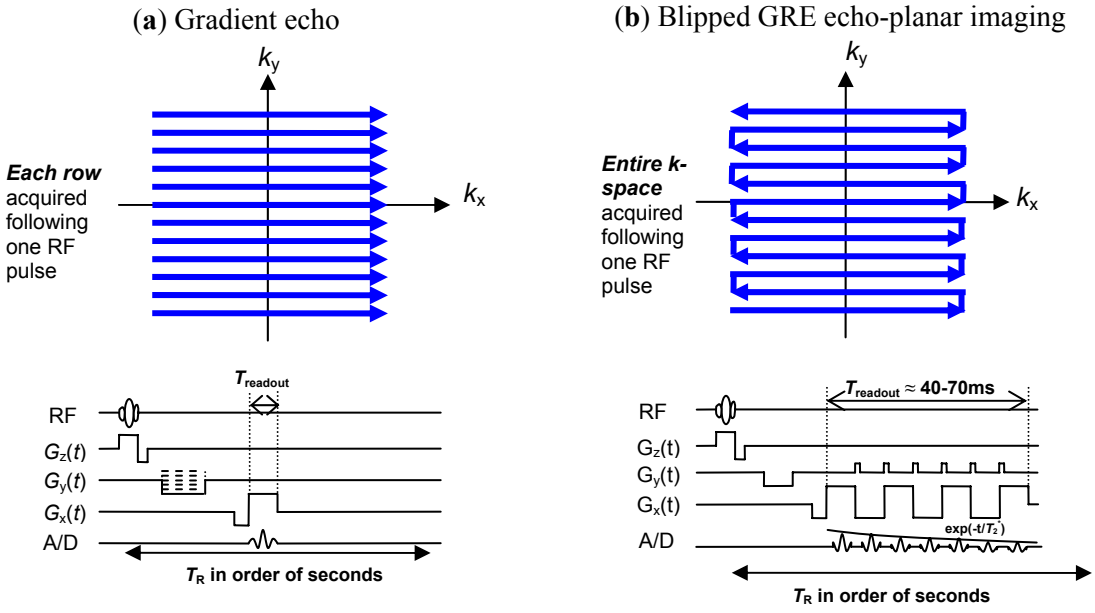

Figure 2.6: Single slice *k*-space trajectories for (**a**) basic gradient echo and (**b**) single-shot blipped GRE echo-planar imaging protocols.

2.3 B0 Field-Inhomogeneity Map Estimation

The field-inhomogeneity map or off-resonance map, represented by the symbols $\Delta B(\vec{r}\,)$ and $\Delta\omega(\vec{r}\,)=2\pi\gamma\Delta B(\vec{r}\,)$ respectively, quantifies the deviation of the magnetic field in the MR scanner from the applied magnetic field. Some authors refer to the two maps simply as the field map. Field-inhomogeneity in MRI may be induced by object-specific causes such as tissue

susceptibility differences or by scanner-specific causes such as main B_0 or gradient field variations. The use of shimming techniques can reduce the field-inhomogeneity over a human head to smaller than 1 ppm everywhere except the anterior frontal lobe and the inferior temporal lobes. These regions have significant susceptibility-induced field-inhomogeneities due to the presence of air-tissue and bone-tissue interfaces. Ideally, the magnetic field in an object in a homogenous B_0 field should be B_0. However, due to magnetic susceptibility χ, the actual field is $B=(1+\chi)B_0$ instead. At a boundary of two tissues with significant susceptibility difference, there is a local change in the magnetic field and thus the spins' Lamor frequencies are no longer homogeneous.

Many proposed field map estimation methods revolve around taking the phase difference between two gradient recall echo (GRE) scans of the same object, each acquired at a different echo time [14-17]. These methods assume that all the phase accrual occurs at the respective echo times. The echo time difference is typically chosen to be small to prevent phase wrapping. In the context of fMRI time-series imaging, a field map acquired at a single time point in the course of the experiment is known as a static field map. Section 3.1.2 describes a conventional static field map estimation method in greater detail. Field maps acquired at multiple time points during the fMRI experiment form a set of dynamic field maps that tracks some of the the field-inhomogeneity changes for the duration of the experiment [9,18]. A static field map is generally higher in spatial resolution but prone to motion-induced errors. These errors may arise due to motion in-between the two echoes acquired for field map estimation and to motion in–between field map acquisition and time-series data acquisition. Dynamic field maps are more impervious to motion-induced field map errors but generally suffer from lower field map resolution [9], increased complexity in the estimation process [10,12] or the need for pulse sequence modification [9].

2.4 B0 Field-Inhomogeneity in Cartesian Blipped EPI

2.4.1 Overview of Field-Inhomogeneity Artifacts

This magnetic field variation can cause four artifacts [19] of which the first is the main topic of interest in this report:

i) in-plane 2D geometric distortion,

ii) signal loss due to in-plane (i.e. echo-shifting effect) intra-voxel dephasing,

iii) signal loss due to through-plane intra-voxel dephasing,

iv) slice selection profile warp.

2.4.2 Two-Dimensional Geometric Distortion

Geometric distortion is readily observed at locations where the magnetic susceptibility varies significantly across material boundaries. Table 2.1 shows the three main types of materials present in a human head – water or soft tissue, bone and air. The largest susceptibility difference occurs at the boundary of soft tissue and air (-9.05 ppm/cm^3) followed by the boundary of bone and air (-8.86 ppm/cm^3). As such, in brain imaging, susceptibility-induced field-inhomogeneities often occur around the petrous bone where the ear structures are located, and the region surrounding the sinuses (air/ tissue interface) which lead to distortion in the temporal lobes and anterior frontal regions respectively [2]. Changing the orientation of the susceptibility interface with B_0 (out-of-plane rotations) will change the field map. Translations and in-plane rotation are less likely to change the susceptibility-induced component of the field map since the tissue interface-B_0 orientation remains the same.

Table 2.1: Magnetic susceptibility values with respect to air [19].

B_0=1.5T, FOV=240mm, 32 kHz, G_z = 3.13 mT/m, 256 pixels	
Material	**χ (ppm / cm^3)**
H_2O (soft tissue)	-9.05
Bone	-8.86
Air	0.0

It is useful to quantify how geometric distortion arises in EPI images in the presence of field-inhomogeneity. To do that, the point spread function (PSF) of the EPI imaging process in the presence of field-inhomogeneity can be derived [3]. Ignoring relaxation effects, the signal equation for a 2D MRI slice with field-inhomogeneity is

$$s(t) = s(k_x(t), k_y(t)) = \int_{-\infty}^{\infty}\int_{-\infty}^{\infty} f(x,y) e^{-j2\pi\gamma[\Delta B(x,y)t(k_x,k_y)]} e^{-j2\pi(k_x(t)x + k_y(t)y)}\, dxdy\,, \qquad (2.3)$$

where $\Delta B(x,y)$ is the field-inhomogeneity at location (x,y), $t(k_x,k_y)$ is the acquisition time-point for k-space sample at (k_x,k_y) and $f(x,y)$ is the imaged object. Note that in the presence of the field-inhomogeneity term, $s(t)$ is no longer the Fourier transform of $f(x,y)$. This is because the field-inhomogeneity term varies with time. The data acquisition time in EPI is negligible in the k_x direction and thus an approximation $t(k_x, k_y) \approx t(k_y)$ can be made as suggested in [3]. The first exponential term in Eq. (2.3) is now independent of k_x and thus the 1D inverse Fourier transform of $s(t)$ can be evaluated with respect to k_x as in

$$\hat{s}(x_i, k_y(t)) = \int_{-\infty}^{\infty} f(x_i, y) e^{-j2\pi\gamma[\Delta B(x_i,y)t(k_y)]} e^{-j2\pi(k_y(t)y)}\, dy\,, \tag{2.4}$$

where $\hat{s}$ is an approximation of s, and x_i is a specific value of x. The problem of finding $f(x,y)$ is now broken down into a set of 1D problems as shown in Fig. 2.7. Each 1D equation $\hat{s}(x_i, k_y(t))$ is the true object profile along x_i deformed by a 1D linear transformation operator $\int_{-\infty}^{\infty} e^{-j2\pi\gamma[\Delta B(x,y)t(k_y)]} e^{-j2\pi(k_y(t)y)}\, dy$.

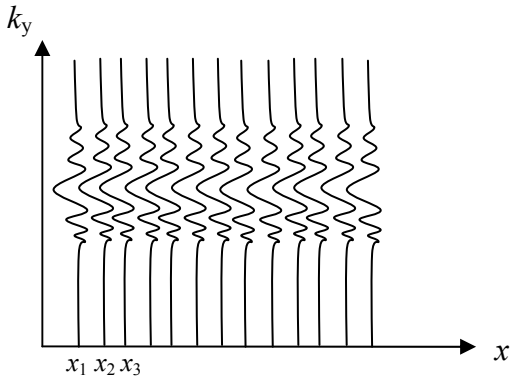

Figure 2.7: 2D signal equation reduced to a set of 1D problems.

The impulse response of the EPI imaging process can be derived by passing an impulse function $f(x,y)=\delta(x-x_i,\ y-y_j)$ with field-inhomogeneity $\Delta B(x_i,y_j)$ into Eq. (2.4). Using the relationship $t(k_y) = k_y/(\gamma G_y)$ for single-shot blipped EPI, Eq. (2.4) can be written as

$$\begin{aligned} h(x, k_y(t)) &= \int_{-\infty}^{\infty} \delta(x - x_i, y - y_j) e^{-j2\pi\gamma[\Delta B(x_i,y)t(k_y)]} e^{-j2\pi k_y(t)y}\, dy \\ &= e^{-j2\pi\gamma[\Delta B(x_i,y_j)t(k_y)]} e^{-j2\pi k_y(t)y_j} \\ &= e^{-j2\pi\gamma[\Delta B(x_i,y_j)(k_y(t)/\gamma G_y(t))]} e^{-j2\pi k_y(t)y_j} \\ &= e^{-j2\pi k_y(t)[\Delta B(x_i,y_j)/G_y(t)+y_j]} \end{aligned}$$

The 1D impulse response can now be evaluated by taking the inverse Fourier transform of $h(x, k_y(t))$ with respect to k_y(t) using the Fourier frequency shift property

$$h(x, y) = \delta\left(x - x_i, y - y_j - \frac{\Delta B(x_i, y_j)}{G_y(t)} \right). \tag{2.5}$$

Eq. (2.5) indicates that a point object with a point field-inhomogeneity located at (x_i,y_j) will cause that point object to shift in the y direction. The amount of shift is proportional to the point field-

inhomogeneity and inversely proportional to the phase encode gradient strength. It is more useful to see Eq. (2.5) in terms of pixel shifts.

From Nyquist sampling theorem, the sampling interval Δy of a 1D bandlimited signal must be at least $1/2k_{y(\max)}$ to prevent aliasing. If the time duration in which $s(t)$ is acquired is T_{readout} and if rectangular phase encode gradient pulses are used in the blipped EPI sequence, then the y-direction spatial resolution Δy can be expressed as

$$\Delta y = \frac{1}{2k_{y(\max)}} = \frac{1}{\gamma \int_0^{T_{\text{readout}}} G_y(\tau) d\tau} = \frac{1}{\gamma G_y T_{readout}} \Rightarrow G_y = \frac{1}{\gamma T_{readout} \Delta y}. \tag{2.6}$$

Substituting Eq. (2.6) into Eq. (2.5), we obtain

$$h(x, y) \approx \delta(x - x_i, y - y_j - \gamma \Delta B(x_i, y_j) T_{readout} \Delta y). \tag{2.7}$$

Since Δy is the y-direction pixel size, Eq. (2.7) shows that the point object at (x_i, y_j) with point field-inhomogeneity shifts in the y-direction by $\gamma \Delta B(x_i, y_j) T_{\text{readout}}$ pixels. The term $1/T_{\text{readout}}$ is also known as the pixel bandwidth in the phase encoded direction. The bandlimited k-space is actually a truncated Fourier space and thus $s(k_x(t), k_y(t))$ is actually multiplied by a window function $\text{rect}(k_x(t)/2k_{x(\max)}, k_y(t)/2k_{y(\max)})$. Thus, the final impulse response is Eq. (2.7) convolved with a $\text{sinc}(2k_{x(\max)}x, 2k_{y(\max)}y)$ function. In other words, the final impulse response is a space variant shift-and-blur operation. The space-variant pixel shift in the phase encode direction causes geometric distortion, intensity accumulation and/ or intensity spread, which adversely affect fMRI activation detection.

2.4.3 Two-Dimensional Geometric Distortion Correction

Most field-correction methods that undo the geometric distortion due to field-inhomogeneity use field maps [2-8]. The field maps have been used to directly shift pixels in the distorted images back to its estimated original positions based on Eq. (2.7) [2], and also to perform field-compensated reconstructions from the MRI measured data to obtain the geometrically correct images [3,5,7,8]. Pixel shift methods are simple to implement and useful for quick evaluations but sub-optimal in distortion-correction performance because it cannot separate the individual contribution of several pixels that map into the same pixel during the distortion process. A popular field-corrected reconstruction method, the conjugate phase technique, tries to compensate for the off-resonance phase accrual at each time point. It should perform better than the pixel-shift method but its performance degrades when the field map is spatially not smooth. This is unfortunate since susceptibility-induced field-inhomogeneities are typically not smoothly

varying. An iterative model-based field-corrected reconstruction method [5] that does not require a smooth field map will be discussed in this section.

The process of estimating the true unknown object $f(\vec{r})$ from the sampled *k*-space data $s(t_i)$ constitutes the MRI image reconstruction problem. The first step in formulating the problem is to parameterize the image into pixels and treat each pixel value as an unknown. Then a system of linear equations can be set up according to the parameterized MR signal equation with additive Gaussian noise. Finally, the system of equations is solved by non-iterative or iterative algorithms. The system of linear equations can be represented in the matrix form. In the notation used here, matrices are printed as upper-case bold characters (e.g. **A**) and column vectors are labeled with an arrow above the variables (e.g. $\vec{k}, \vec{r}$).

Ignoring spin relaxation and assuming spatially invariant receiver coil sensitivity, the non-parameterized MR signal equation for a selected slice in the presence of field-inhomogeneities is

$$s(t_i) = \int_{\infty}^{\infty} f(\vec{r}) e^{-j\Delta\omega(\vec{r})t_i} e^{-j2\pi(\vec{k}(t_i)\cdot\vec{r})}\, d\vec{r}\,, \tag{2.8}$$

where $s(t_i)$ is the baseband signal sample at time t_i during the readout, $\Delta\omega(\vec{r})$ is the spatially variant field-inhomogeneity and $f(\vec{r})$ is a continuous-space function of the net transverse magnetization of the object. Eq. (2.8) can be represented as the result of a linear operator $\mathcal{A}$ applied to the true object *f*. This is a continuous-to-discrete mapping which is inherently ill-posed and under-constrained. There are many potential solutions to $f(\vec{r})$ for any single set of $s(t_i)$ values due to the smoothing effect of the integral operator.

The dominant noise in MRI is from the thermal vibrations of ions and electrons and is conventionally modeled as a white Gaussian noise [20]. Thus, the sampled signal y_i includes $s(t_i)$ and an additive complex independent and identically distributed (i.i.d.) white Gaussian noise ε that can be expressed [5] as

$$\begin{aligned} &y_i = s(t_i) + \varepsilon_i \qquad i = 1.....n_d \qquad \text{or} \\ &\mathbf{y} = \mathcal{A}\mathbf{f} + \boldsymbol{\varepsilon} \end{aligned}. \tag{2.9}$$

To limit the number of parameters to be estimated, the continuous object *f* and field map is parameterized into a sum of n_p weighted rect basis functions $b(\vec{r} - \vec{r}_n)$ as follows.

$$\begin{aligned} f(\vec{r}) &\approx \sum_{n=0}^{n_p-1} f_n \, rect\left(\frac{\vec{r} - \vec{r}_n}{\Delta\vec{r}}\right) = \sum_{n=0}^{n_p-1} f_n b(\vec{r} - \vec{r}_n) \\ \Delta\omega(\vec{r}) &\approx \sum_{n=0}^{n_p-1} \Delta\omega_n \, rect\left(\frac{\vec{r} - \vec{r}_n}{\Delta\vec{r}}\right) = \sum_{n=0}^{n_p-1} \Delta\omega_n b(\vec{r} - \vec{r}_n) \end{aligned}. \tag{2.10}$$

Eq. (2.8) can now be written as a summation over space

$$s(t_i) \approx B(\vec{k}(t_i)) \sum_{n=0}^{n_p-1} f_n e^{-j\Delta\omega_n t_i} e^{-j2\pi(\vec{k}(t_i)\cdot\vec{r}_n)} . \tag{2.11}$$

where $B(\vec{k}(t_i))$ is the Fourier transform of $b(\vec{r})$ (a sinc) and f_n is the object intensity at location $\vec{r}_n$. The continuous-discrete model of Eq. (2.9) can now be written as a discrete-discrete model

$$\mathbf{y} = \mathbf{A}\mathbf{f} + \boldsymbol{\varepsilon} . \tag{2.12}$$

where **f** is the column-wise stacked vector of the parameterized object, ***y*** is the *k*-space data vector and **A** is the possibly ill-conditioned n_d-by-n_p system-object matrix with elements $a_{m,n} = B(\vec{k}(t_m))e^{-j\Delta\omega_n t_m} e^{-j2\pi(\vec{k}(t_m)\cdot\vec{r}_n)}$. The image reconstruction problem is now to estimate **f** given **y** and the system-object matrix **A** (which requires knowledge of $\Delta\omega$).

There are three main considerations in choosing the cost function and an algorithm to solve Eq. (2.12). First, **A** may be ill-conditioned and thus some form of regularization must be integrated into the cost function. Secondly, **A** is a huge matrix even for small image sizes. Thus computing the pseudo-inverse of **A** to find a solution for **f** will require extensive storage resources and computation time. Thus, an iterative approach is taken to solve for **f**. Thirdly, the solution must take into account MR Gaussian noise in **y**.

Most field-corrected reconstruction methods involve two steps: measuring a field map and using it to reconstruct a field-corrected image. Many non-iterative methods like the conjugate phase reconstruction technique [8] work better with a spatially smooth field map. This requirement may hold for field-inhomogeneities due to hardware imperfections but not for susceptibility-induced field-inhomogeneities which have higher order spatial variations. Model-based iterative reconstruction methods do not require a smooth field map and models the problem with noise more accurately. It has been reported [7] that iterative conjugate gradient methods outperform the conjugate phase method for EPI images. The conjugate phase estimator attempts to reconstruct the image by compensating for the phase accrual at each time point in Eq. (2.11). A weighting matrix is often included for non-uniformly sampled *k*-space data. Since the EPI *k*-space data is assumed to be uniformly sampled for simplicity, this weighting matrix is the identity matrix and the conjugate phase estimator becomes

$$\hat{f}_{CP}(\vec{r}) = \sum_{i=0}^{n_d-1} y_i e^{j\Delta\omega(\vec{r})t_i} e^{j2\pi(\vec{k}(t_i)\cdot\vec{r})} = \mathbf{A}^*\mathbf{y} = \mathbf{A}^*(\mathbf{A}\mathbf{f} + \boldsymbol{\varepsilon}) . \tag{2.13}$$

In [5], **f** is estimated directly from the *k*-space data ***y*** by minimizing a quadratic penalized least squares cost function using the conjugate gradient optimization algorithm. The reconstruction obtained from the density compensated non-iterative conjugate phase algorithm is used as the

initial guess of **f** in the conjugate gradient algorithm. In EPI, since the measured samples are assumed to be uniformly spaced, we can assign an identity matrix to the weighting matrix in [5]. The cost function and estimator can thus be written as

$$\psi_1(\mathbf{f}) = \frac{1}{2}\|\mathbf{y} - \mathbf{A}\mathbf{f}\|^2 + \frac{1}{2}\beta \mathbf{f}^T \mathbf{C}^T \mathbf{C}\mathbf{f} \,. \tag{2.14}$$

$$\hat{\mathbf{f}}_{QPLS} = \arg\min_f \psi_1(\mathbf{f}) = [\mathbf{A}^*\mathbf{A} + \beta\mathbf{R}]^{-1}\mathbf{A}^*[\mathbf{A}\mathbf{f} + \boldsymbol{\varepsilon}]. \tag{2.15}$$

where **C** is a n_p-1×n_p differencing matrix and $\mathrm{R} = \mathbf{C}^T\mathbf{C} = \begin{bmatrix} -1 & 1 & 0 & 0 & \cdots & 0 \\ -1 & 2 & -1 & 0 & \cdots & 0 \\ 0 & -1 & 2 & -1 & \cdots & 0 \\ \vdots & \vdots & \vdots & \vdots & \vdots & \vdots \\ 0 & 0 & \ldots & -1 & 2 & -1 \\ 0 & 0 & \ldots & 0 & -1 & 1 \end{bmatrix}$.

Since the dominant noise in MRI measurements is i.i.d. Gaussian, the least squares-based estimator is appropriate. Without regularization, the least squares estimator $\hat{\mathbf{f}}_{LS}$ given i.i.d. Gaussian measurements is also the maximum likelihood estimator. To lower the condition number of the matrix **A**, some form of regularization must be added. This adds bias to the estimator. The first term in Eq. (2.14) is the least squares data-consistency criteria in that it encourages a solution $\hat{\mathbf{f}}_{QPLS}$ that, when forward projected by **A**, is closest in the least squares sense to the measured data ***y***. The second term $\mathbf{f}^T\mathbf{C}^T\mathbf{C}\mathbf{f}$ is a regularization function **R**(**f**) which penalizes the roughness of the estimate and reduces the condition number of the potentially ill-conditioned matrix **A**. This regularization function has the effect of constraining the candidate solutions to those that are spatially smooth and acts like a low-pass filter. The regularization parameter β controls how smooth these candidate solutions are. A larger value of β will reduce the spatial resolution of the reconstructed image and introduce a greater bias to the estimate $\hat{\mathbf{f}}_{QPLS}$. β is chosen small enough such that the resultant point spread function of the reconstructed image is not too much greater than the natural resolution associated with the EPI *k*-space trajectory.

The iterative conjugate gradient (CG) method is an efficient way to minimize Eq. (2.14) especially when **A** is large and sparse. The conjugate gradient algorithm operates exactly like the iterative steepest descent algorithm except that instead of searching in the direction of the steepest gradient, the n^{th} search direction is **A**-orthogonal to all previous search directions. Theoretically, the CG algorithm converges in at most *m* iterations where *m* is the number of eigenvalues of **A**. In the implementation, the CG algorithm uses the conjugate phase reconstructed image as the initial guess of **f**.

As stated previously, the signal equation with field-inhomogeneity is no longer the Fourier transform of the object because the off-resonance term $e^{-j\Delta\omega_n t}$ depends on t. Otherwise, the term can be treated as a constant and be absorbed into the object $f(\vec{r})$ and Eq. (2.3) becomes a Fourier transform expression again. This problem is handled in [5] by dividing the acquisition window into L+1 time segments of width τ such that $e^{-j\Delta\omega(\vec{r})t} \approx \sum_{l=0}^{L} a_l(t) e^{-j\Delta\omega_n \tau l}$. Substituting this expression of $e^{-j\Delta\omega(\vec{r})t}$ into Eq. (2.11), the time-segmented approximation to the signal equation is

$$\hat{s}(t) \approx B(\vec{k}(t)) \sum_{l=0}^{L} a_l(t) \sum_{n=0}^{n_p-1} \left[f_n e^{-j\Delta\omega_n \tau l} \right] e^{-j2\pi(\vec{k}(t)\cdot\vec{r}_n)} . \qquad (2.16)$$

where $a_l(t)$ is the interpolation coefficient for the l^{th} time-segmented point and is chosen such that the error in approximating $s(t_i)$ with $\hat{s}(t_i)$ is minimized. This is done using the min-max criterion described in [5]. Eq. (2.16) shows a weighted sum of DFTs for EPI data where the frequency samples are assumed to be uniformly spaced.

One of the greatest limitations of EPI occurs when a local field gradient causes a phase change of about 2π or more across a voxel. In this case the signal from that voxel is not displaced but lost all together due to signal dephasing. It was reported previously that it is not possible to correct for susceptibility induced signal loss using field mapping techniques [21].

2.4.4 Field-Inhomogeneity Induced In-Plane Signal Loss Correction

Field-inhomogeneity gradients in the phase encoded and frequency encoded directions give rise to echo shifts in *k*-space. The displacement of the echoes diminishes the image contrast information found in the lower frequency regions. If the field-inhomogeneity gradients are strong enough, the echoes may be shifted outside the MR signal acquisition window and thus lead to complete signal loss. Local field-inhomogeneity gradients will lead to decreased image intensity in the locality of the field-inhomogeneity gradients. To correct for such signal loss in the iterative reconstruction framework [5], the field map should be modeled with piece-wise linear or triangular basis functions to account for field gradients [48].

2.5 Retrospective Motion Correction Methods

2.5.1 Rigid Body Registration

Image registration involves determining a transformation **T** that relates the position of features in one image or coordinate space to another. Image registration can be done from 2D to 2D space, 3D to 3D space or 3D to 2D space. If the images to be registered generally differ only in their relative global positions, then we can describe the required transformation in terms of just rotations and translations. This is known as a rigid body transformation. This assumption works very well for brain images since the skull restricts the brain movement to less than 1 mm [22]. For this project, only 3D to 3D slice-to-volume rigid body registration is used.

For 3D to 3D rotate-translate rigid body registration, there are six degrees of freedom or six unknown transformation parameters shown in Fig. 2.8. They include the translation parameters t_x, t_y, t_z in the x, y and z directions and the rotation angles θ_x ,θ_y ,θ_z about the x, y, z axes respectively. This transformation can be represented in matrix form as a series of rotation operations **R** followed by translations **t**.

$$\mathbf{T}_{rigid}(\bar{r}) = \mathbf{R}\bar{r} + \mathbf{t}$$

$$= \begin{pmatrix} \cos\theta_y\cos\theta_z & \cos\theta_x\sin\theta_z + \sin\theta_x\sin\theta_y\cos\theta_z & \sin\theta_x\sin\theta_z - \cos\theta_x\sin\theta_y\cos\theta_z \\ -\cos\theta_y\sin\theta_z & \cos\theta_x\cos\theta_z - \sin\theta_x\sin\theta_y\sin\theta_z & \sin\theta_x\cos\theta_z + \cos\theta_x\sin\theta_y\sin\theta_z \\ \sin\theta_y & -\sin\theta_x\cos\theta_y & \cos\theta_x\cos\theta_y \end{pmatrix} \begin{pmatrix} x \\ y \\ z \end{pmatrix} + \begin{pmatrix} t_x \\ t_y \\ t_z \end{pmatrix}. \tag{2.17}$$

$$= \begin{pmatrix} \cos\theta_y\cos\theta_z & \cos\theta_x\sin\theta_z + \sin\theta_x\sin\theta_y\cos\theta_z & \sin\theta_x\sin\theta_z - \cos\theta_x\sin\theta_y\cos\theta_z & t_x \\ -\cos\theta_y\sin\theta_z & \cos\theta_x\cos\theta_z - \sin\theta_x\sin\theta_y\sin\theta_z & \sin\theta_x\cos\theta_z + \cos\theta_x\sin\theta_y\sin\theta_z & t_y \\ \sin\theta_y & -\sin\theta_x\cos\theta_y & \cos\theta_x\cos\theta_y & t_z \\ 0 & 0 & 0 & 1 \end{pmatrix} \begin{pmatrix} x \\ y \\ z \\ 1 \end{pmatrix}$$

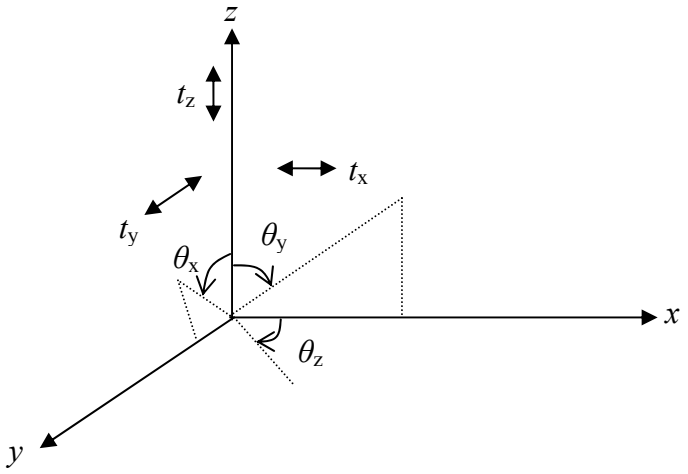

Figure 2.8: Rigid body rotate translate transformation parameters.

For registration algorithms that use voxel intensities directly, the transformation **T** can be found by iteratively optimizing a similarity measure derived from the comparison of the intensities in the overlapping regions of the two images.

2.5.2 Mutual Information

Mutual information (MI) is a concept from information theory that measures the statistical dependence between two random variables. In other words, it measures the information that one random variable contains about the other. In the image registration problem, the random variables are the image intensities A and B of the two images to be registered with marginal probability density functions $p_A(a)$ and $p_B(b)$ and joint probability density function $p_{AB}(a,b)$. A and B are statistically independent if $p_{AB}(a,b) = p_A(a)p_B(b)$. They are maximally dependent if they are related by a one-to-one mapping T: $p_A(a) = p_B(T(a)) = p_{AB}(a,T(a))$. In image registration, MI is maximal when the images are registered. MI measures the statistical dependence between A and B by measuring the Kullback-Leibler distance [23] between the actual joint distribution $p_{AB}(a,b)$ and the joint distribution for which A and B are independent, i.e. $p_A(a)p_B(b)$. MI can be expressed as

$$I(A,B) = \sum_{a,b} p_{AB}(a,b) \log \frac{p_{AB}(a,b)}{p_A(a)p_B(b)} . \tag{2.18}$$

If the intensities of the two datasets to be registered are linearly correlated, similarity measures such as absolute difference, cross-correlation or sum-of-squared differences of intensities within overlapping regions can be used. This is usually true for intra-modality registration or registration between images acquired by the same imaging technique. However, this is generally not true for inter-modality registration. For MI, the nature of the dependence (linear, non-linear) of A and B is not assumed which makes it highly data independent. In fMRI, motion correction is typically performed between T_2^*-weighted EPI slices or between T_2^*-weighted EPI slices and a T_1-weighted 3D anatomical volume. Since T_2^*-weighted and T_1-weighted images are not linearly correlated with each other, MI is a good choice for the motion correction similarity measure.

MI is closely related to the entropies of the random variables A and B. The entropy H(A) and H(B) is known as the amount of uncertainty associated with the respective random variables. H(A,B) is the joint entropy of A and B. H(A|B) be the conditional entropy of A given B or the uncertainty left in A upon knowing B. MI is related to entropy by the following equations

$$I(A,B) = H(A) + H(B) - H(A,B) = H(A) - H(A \mid B) = H(B) - H(B \mid A). \quad (2.19)$$

The Shannon entropy equations of interest are defined as follows.

$$H(A) = -\sum_{a} p_A(a) \log p_A(a). \quad (2.20)$$

$$H(A,B) = -\sum_{a,b} p_{AB}(a,b) \log p_{AB}(a,b). \quad (2.21)$$

$$H(A \mid B) = -\sum_{a,b} p_{AB}(a,b) \log p_{A|B}(a \mid b). \quad (2.22)$$

An optimization method is required to search for the transformation that gives the highest MI value. Unlike quadratic cost functions, the MI metric does not have a tractable analytical form to its gradient with respect to the motion parameters. The MI metric as a function of motion parameters also consists of many local minima, unlike the concave quadratic cost function. Thus common gradient-based optimization techniques like steepest descent or conjugate gradient cannot be used directly. A direct search method known as the Nelder Mead simplex optimization method implemented in the MIAMI Fuse software [24] by the University of Michigan Radiology Department's Digital Image Processing Laboratory is used for this project. The Nelder-Mead simplex algorithm used is robust and computationally simple but may be sub-optimal in that the number of iterations required to reach a solution is not the minimum possible.

2.5.3 Map Slice-to-Volume Motion Correction

Conventionally, in fMRI, motion correction is done by performing rigid body slice-to-slice registration of the EPI slices to a designated 'typical' EPI slice in the time-series. This form of registration ignores out-of-plane motion which is not realistic since the head can move in any of the six degrees of freedom. Volume-to-volume rigid body registration between each time-series volume to a reference or an anatomically accurate 3D volume is also sometimes done for motion correction. This model is inaccurate for multi-slice EPI since it does not account for inter-slice head motion. A more accurate motion correction model allows each slice to have its own six DOF motion parameters. Motion correction is then done by registering each EPI slice to a 3D anatomical volume as shown in Fig. 2.9.

Automated 3D registration of a slice into an anatomical volume is accomplished in [25] by optimizing the mutual information metric calculated from the gray values of the overlapping region of the image pair. For rigid body registration, three control points are placed in the reference anatomical volume as well as the EPI slice in a 3D space. The Nelder-Mead simplex algorithm generates an ordered set of search positions for the control points within a user-

specified radial bound. Each new set of control point positions have a rigid body transformation that will align the reference and homologous control points. The homologous volume is re-mapped using this transformation and the MI metric is computed. The transformation that gives the lowest MI metric in the iterative optimization scheme is the final estimated motion parameters that will bring the homologous and reference data into alignment. Previous results in [25] have shown that the MSV method outperforms the slice-stack method which registers stacks of slices to the anatomical volume. The slice-stack registration method allows out of plane motion but does not model motion in individual slices. Additional results in [26] on simulated EPI data with known ground truths for motion, activation and geometric distortion suggests that MSV-corrected datasets yield better activation detection performance compared to SPM-generated results.

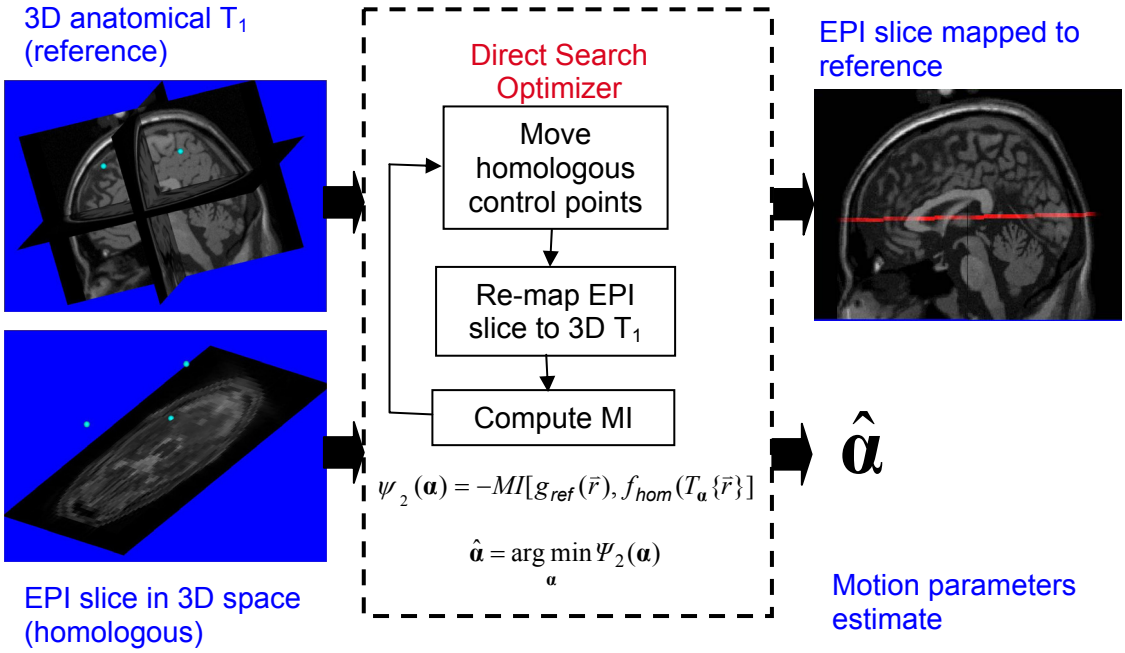

Figure 2.9: Overview of MSV registration scheme.

2.6 Joint Two-Dimensional Motion and Geometric Distortion Problem

Conventionally, motion effects and field-inhomogeneity induced geometric distortion in EPI are corrected separately in fMRI, if at all. Motion-correction is conventionally done by registering time-series volumes/slices to a 'typical' volume/ slice selected from the time-series or to a higher resolution anatomically accurate reference volume. Geometric distortion in EPI is typically corrected with a field map. However, accurate distortion correction requires an accurate field

map. Unfortunately, the two problems are inter-related in that the field map changes as the head moves. Ideally, in order to do accurate geometric distortion correction, multiple field maps should be acquired during the fMRI scan to track the temporal changes in the field-inhomogeneity. However, for a variety of reasons, only one field map is usually acquired prior to, or, after the fMRI experiment. Some of these reasons include the additional effort required to modify pulse sequences for dynamic field map acquisition [9], increased computational complexity [10] and the need to balance the tradeoffs between obtaining acceptable field map spatial resolution and good image time series temporal resolution [9].

CHAPTER 3

Motion-Robust Field-Inhomogeneity Estimation Using Dual-Echo Fast GRE

In this section, a dual-echo fast gradient echo (DEFGRE) pulse sequence using two back-to-back readout gradients, each at a different echo time and of opposing polarity to the other, is investigated for static field map estimation [11]. This pulse sequence can yield field maps with reduced motion-induced errors compared to the conventional static field map acquisition method using two different echo times. This is due to the greatly reduced time elapsed between data acquisition of the two different echoes. However, there is an inherent phase error in the dual-echo method due to the opposite polarity of the two readout pulses. Results from three phantoms and three patients scanned over a period of two years by the same GE Signa 1.5T scanner show that the first order phase error inherent in the dual-echo field map is relatively constant at 0.1 rad/ pixel and hence may be applied to different data acquired over time. The zero order phase error changes with time but can be approximated empirically.

3.1 Introduction

The static magnetic field passing through an object in an MRI scanner is perturbed by disjoint object regions with different magnetic susceptibilities that augment the magnetic field-inhomogeneity caused by imperfections in the gradients and main magnet. Field-inhomogeneity causes image artifacts that increase in severity as the static magnetic field strength, B_0, increases. Such artifacts are especially apparent in high-speed MRI techniques like echo-planar imaging and spiral imaging where geometric distortion and blurring are observed, respectively, because of the

longer readout time. Most correction methods for field-inhomogeneity effects require an accurate estimate of the field map [2,4]. These methods assume that the data from two different echo times acquired for field map estimation are free of acquisition dependant errors, i.e., position changes due to motion.

A static field map can be estimated by taking the phase difference of a pair of gradient-echo images acquired at two different echo times [14-16]. The echo time difference is typically constrained to be small to prevent phase wrapping. With a few exceptions, field maps are generated using two separate image acquisitions with different echo times. However, this method is prone to motion-induced and position dependent errors that degrade the field map. Using two separate RF excitations with different echo times would produce accurate field maps only in the absence of motion, i.e., phantom studies. Ideally, B_0 field maps may be computed from the phase changes between two time points of the same images. In human data sets, a common problem of computing field maps from two different images, acquired at two different echo times, is the change in B_0 during the time delay due to the motion, either bulk head motion or physiological brain motion, which cause the error in field map measurement. Typical acquisition times for 3D SPGR volumes used for the field map computations are approximately three to four minutes. With a normal subject, the mean translation and rotation of the head were observed to be 2.25 mm and 0.71º, respectively, in a three minute scan time [25]. Even if the head is restrained, brain tissue velocity for normal subject could be 0.94±0.26 mm/s due to the physiological motion [27]. The corresponding images from the two separate volumes with typical three minute acquisition time will then be misregistered resulting in the field map estimation error. There is a clear advantage in measuring a field map from the same images acquired at two different echo times, i.e., using a dual-echo sequence.

Partial *k*-space techniques for dynamic field map estimation can greatly reduce motion-induced errors but may suffer from decreased field map resolution [9]. Some EPI-based dynamic field map estimation methods acquire the field maps in distorted space, obviating the need for registration between the field maps and the geometrically distorted EPI images [9,18]. Other field-inhomogeneity correction methods assume that the field map is available in undistorted space [5,7]. In some dynamic field mapping techniques, dual-echo images are acquired by using the same positive polarity in the read out gradient, but that would require pulse sequence modifications, an option that may not be available on all clinical scanners.

This work presents a zero and first order phase shift correction technique used in conjunction with a simple dual-echo fast gradient echo (DEFGRE) pulse sequence employing two back-to-back readout gradients, continuous but of opposite polarity, for static field map

estimation. This work describes a relatively straightforward technique that allows computation of field maps without the need to modify a commonly available sequence in a clinical set up where the sequence modification is not accessible. The pulse sequence, DEFGRE, acquires two echoes efficiently with one RF pulse and the image data can be used to compute field maps without inter-echo motion-induced position errors. It is to be noted that inter-phase encode motion is not addressed with this technique. A caveat in using this sequence is that, due to the asymmetry of the readout gradients, artifactual phase shifts causing phase wraps are evident in the phase difference map. This study focuses on correcting this residual phase error to remove the phase wraps without using elaborate phase unwrapping algorithms [28,29]. We formulate a hypothesis of how the asymmetric readout pulses cause the artifactual phase shift and then model the phase error as an affine term in the readout direction. The unknown affine model parameters are then estimated using motionless phantom data. Results from several sets of phantom and patient data acquired on the same scanner with the same scan parameters over a period of two years suggest that the first order phase correction term does not change for a given scanner over time and hence can be applied to the field map estimation of different data sets. The zero order phase correction term may change with time but can be estimated empirically from the dual-echo data for each new scan.

3. 2 Dual-Echo Fast Gradient Echo Pulse Sequence

In the generally used static field map estimation method, two complex images, $I_{\mathrm{TE1,sep}}$ and $I_{\mathrm{TE2,sep,}}$ are acquired separately at two different echo-times, TE1 and TE2 where TE2>TE1. Assuming all scan parameters, excluding the echo-time, are identical for the two sets of images, $I_{\mathrm{TE2,sep}}$ will approximately be equal to the complex magnetization M_{sep} of $I_{\mathrm{TE1,sep}}$ multiplied by a complex phase term dependent on the field-inhomogeneity. The two sets of images can be written as

$$I_{\mathrm{TE1,sep}}(\boldsymbol{r}) = M_{\mathrm{sep}}(\boldsymbol{r}) + \varepsilon_1(\boldsymbol{r}) \ , \tag{3.1}$$

$$I_{\mathrm{TE2,sep}}(\boldsymbol{r}) = M_{\mathrm{sep}}(\boldsymbol{r}) e^{j(\Delta\omega_{\mathrm{sep}}(\mathbf{r})\Delta\mathrm{TE}_{\mathrm{sep}})} + \varepsilon_2(\boldsymbol{r}) \tag{3.2}$$

where the spatial variable is $\boldsymbol{r} = [x\ y\ z]^T$, the true off-resonance map is denoted by $\Delta\omega_{\mathrm{sep}}$, ΔTE=TE2-TE1, and the images have complex noise denoted by ε_1 and ε_2. The off-resonance map can be estimated as

$$\Delta\hat{\omega}_{\text{sep}}(\boldsymbol{r}) = \frac{\angle\left[I_{\text{TE2,sep}}(\boldsymbol{r}) I^{*}_{\text{TE1,sep}}(\boldsymbol{r})\right]}{\Delta\text{TE}_{\text{sep}}} \approx \Delta\omega_{\text{sep}}(\boldsymbol{r}), \tag{3.3}$$

Where $I^{*}_{\text{TE1,sep}}$ denotes the complex conjugate of $I_{\text{TE1,sep}}$. Fig. 3.1(a) shows an example of an off-resonance map estimated with Eq. (3.3).

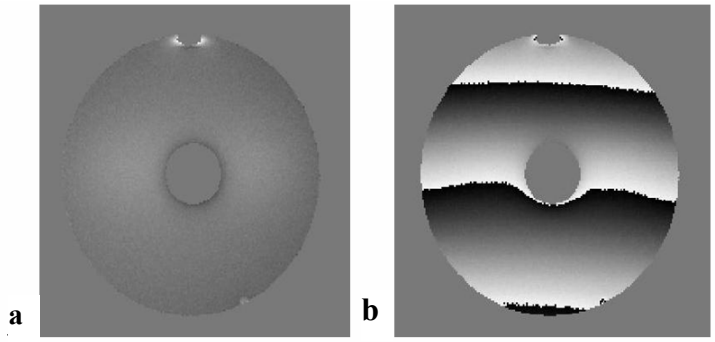

Figure 3.1: Off-resonance maps of phantom estimated by (**a**) standard off-resonance method, (**b**) uncorrected dual-echo method showing linear phase wrapping in readout direction (*x* direction downwards).

In the proposed dual-echo field map method, two complex images $I_{\text{TE1,dual}}$ and $I_{\text{TE2,dual}}$ are acquired with back-to-back readout gradients. There is no delay between the pulses, which have opposite polarity, as shown in Fig. 3.2.

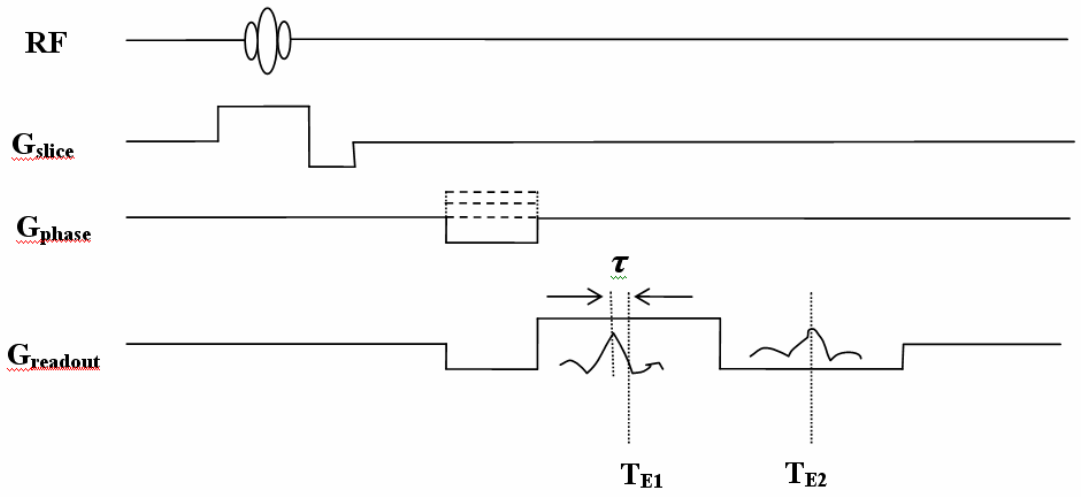

Figure 3.2: Simplified dual-echo pulse sequence with back-to-back $G_{readout}$ pulses with opposite polarity. Readout data from T_{E1} may be off-center relative to data from T_{E2}. The first order phase shift correction term α is proportional to the time delay τ.

Due to imperfect gradient balancing along the readout direction, as in most scanners, the two sampled echoes for each readout line may not be centered relative to each other in the readout direction in *k*-space. Assuming that the gradient imbalance is relatively constant for every scan, we model this non-ideal behavior as a net shift of one of the *k*-space echo data relative to the other in the readout direction as shown in Fig. 3.3. This frequency shift induces a spatially linear, first order phase shift term, $e^{j\alpha x}$, in the readout direction in the image domain. This term would cause massive phase wrapping in the readout direction if the general field map estimation procedure in Eq. (3.3) were applied to the dual-echo data under the unrealistic assumption that the gradient pulses are symmetric.

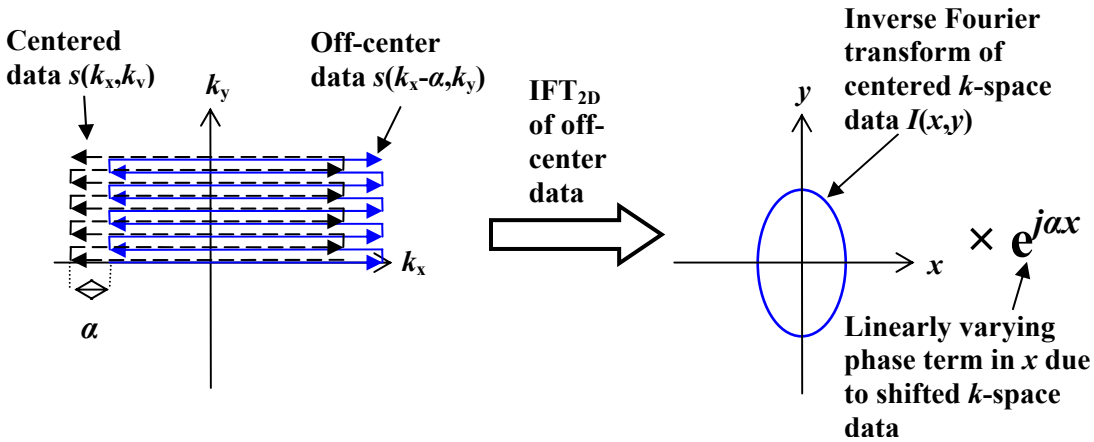

Figure 3.3: Frequency shifted *k*-space data is transformed via inverse Fourier transform to an image with an affine phase error term in the readout direction *x*.

Ignoring T_2 relaxation effects, we model $I_{\mathrm{TE2,dual}}$ as the complex magnetization of $I_{\mathrm{TE1,dual}}$, denoted by M_{dual}, multiplied by several complex terms as follows:

$$I_{\mathrm{TE1,dual}}(\boldsymbol{r}) = M_{\mathrm{dual}}(\boldsymbol{r}) + \varepsilon_3(\boldsymbol{r}) \tag{3.4}$$

$$I_{\mathrm{TE2,dual}}(\boldsymbol{r}) = M_{\mathrm{dual}}(\boldsymbol{r}) e^{j(\Delta\omega_{\mathrm{sep}}(\boldsymbol{r})\Delta\mathrm{TE}_{\mathrm{dual}})} e^{j(\alpha x+\beta)} + \varepsilon_4(\boldsymbol{r}) \tag{3.5}$$

where the field-inhomogeneity induced complex term is denoted by $e^{j(\Delta\omega_{\mathrm{sep}}(\mathbf{r})\Delta\mathrm{TE}_{\mathrm{dual}})}$ and the first order phase shift is modeled by $e^{j\alpha x}$ where x is the readout direction. The complex term $e^{j\beta}$ attempts to model any residual zero order phase shift left over after the first order phase component has been removed. Multiplying Eq. (3.4) by the complex conjugate of Eq. (3.5) and dividing by its magnitude, we obtain

$$\begin{aligned} I_{dual}(\boldsymbol{r}) &= I_{TE\,2,dual}(\boldsymbol{r}) I^{*}_{TE\,1,dual}(\boldsymbol{r}) / \left| I^{*}_{TE\,1,dual}(\boldsymbol{r}) \right| \\ &= \left| M_{dual}(\boldsymbol{r}) \right| e^{j(\Delta\omega_{sep}(\boldsymbol{r})\Delta TE_{dual})} e^{j(\alpha x+\beta)} + \varepsilon_5(\boldsymbol{r}) \end{aligned} \tag{3.6}$$

where the phase of the complex magnetization M_{dual} cancels out. The off-resonance map can be estimated by taking the ratio of the phase of I_{dual} and $\Delta\mathrm{TE}_{\mathrm{dual}}$,

$$\Delta\hat{\omega}_{dual}(\boldsymbol{r}) = \frac{\angle\left[I_{dual}(\boldsymbol{r})\right]}{\Delta TE_{dual}} = \Delta\omega_{sep}(\boldsymbol{r}) + \frac{\alpha x + \beta}{\Delta TE_{dual}} + \eta_1(\boldsymbol{r}) \cdot \tag{3.7}$$

However, for the DEFGRE acquisitions, this estimate of the field map is highly inaccurate unless the massive phase wrapping caused by the first order phase term $e^{j\alpha x}$, as shown in Fig. 3.1(b), is removed.

3. 3 Residual Phase Error Correction

To obtain field maps with DEFGRE, we assume that the affine phase parameters α and β are independent of the object being scanned, in which case they need to be calibrated only once for all the data acquired in the same scanner with a given set of imaging parameters, i.e., imaging sequence and field-of-view. A phantom filled with doped water, which has a well-defined homogeneous region, was scanned for the purpose of computing the calibration term, first, using 2D fast SPGR sequence, twice, at different echo times followed by a dual-echo aquisition using

DEFGRE sequence. The off-resonance map estimates $\Delta\hat{\omega}_{\text{sep}}$ and $\Delta\hat{\omega}_{\text{dual}}$ were then computed using Eqs. (3.3) and (3.7) respectively. Since the spherical phantom is motionless, it is reasonable to consider $\Delta\hat{\omega}_{\text{sep}}$ to be the ground truth of the phantom field map. We estimate the correction parameters α and β by minimizing the following cost function with phantom data:

$$\hat{\alpha},\hat{\beta} = \arg\min_{\alpha,\beta} \sum_{x=0}^{N-1} \left| \angle\left\{ \exp\left[j\frac{\alpha x + \beta - \Delta\hat{\phi}_{\text{dual}}(x,y_0)}{\Delta\text{TE}_{\text{dual}}} \right] \right\} - \angle\left\{ \exp(\, j\Delta\hat{\omega}_{\text{sep}}(x,y_0)) \right\} \right|^2, \qquad (3.8)$$

where y_0 is a column of N pixels for which $|M_{\text{dual}}|$ is significantly large, i.e. $|M_{\text{dual}}|$ exceeds 10% of the maximum image intensity of dual-echo data, $\Delta\hat{\phi}_{\text{dual}}$ is the estimate of the dual-echo phase difference map or $\angle[I_{\text{dual}}]$, $\Delta\text{TE}_{\text{dual}}$ is the time difference between the two echoes in the DEFGRE sequence, y is the phase encoding direction, x is the readout direction and $\Delta\hat{\omega}_{\text{sep}}$ is the estimate of the off-resonance map obtained with Eq. (3.3). The first order phase error α is solely dependent on the gradient imbalance, and should not change considerably with different $\Delta\text{TE}_{\text{dual}}$. The estimation of α will serve to unwrap the linear component of the phase error. Data from a single column y_0 is used in Eq. (3.8) since the first order phase shift is modeled in the readout or x direction. The values of α and β estimated via the Nelder-Mead simplex method are used to correct the dual-echo field map acquired for subsequent studies. All phase correction computational work was performed on an Intel Pentium 4 3.6 GHz CPU using MATLAB (The Mathworks Inc., Natick, MA).

The cost function in Eq. (3.8) is periodic with respect to β and has many local minimum points with respect to α in the vicinity of the global minimum. This may cause the Nelder-Mead algorithm to yield a local minimum point as the optimum solution. An alternative optimization method is to perform a line search with respect to α, and then use the solution of α in a derived maximum likelihood analytical solution for β assuming a white Gaussian observation model. A maximum likelihood estimator can be derived for β while α can be estimated via a line search. Let the observation model be

$$Z = me^{j\theta} + N, \qquad (3.9)$$

where m is an unknown magnitude, θ is the unknown phase of interest and N is complex, zero-mean Gaussian noise with variance σ^2, i.e., $\begin{bmatrix} real(N) \\ imag(N) \end{bmatrix} \sim N\left(\begin{bmatrix} 0 \\ 0 \end{bmatrix}, \begin{bmatrix} \sigma^2 & 0 \\ 0 & \sigma^2 \end{bmatrix}\right) = N(\mu_N, \Sigma_N)$. Thus, the likelihood function can be written as follows:

$$f_Z(z;\theta) = \frac{1}{\sqrt{(2\pi)^n |\Sigma_N|}} e^{-(z-\mu_N)^H \Sigma_N^{-1}(z-\mu_N)/2}, \tag{3.10}$$

where $\mu_N = E[Z]$. Taking the logarithm of Eq. (3.10) and removing the terms that are independent of θ, the log-likelihood can be written as

$$\begin{aligned} &\log f_Z(z;\theta) \\ &\equiv -\frac{1}{2}\left|z - me^{j\theta}\right|^2 \\ &= -\frac{1}{2}\left(z - me^{j\theta}\right)\left(z^* - me^{-j\theta}\right) \\ &\equiv \frac{1}{2} zme^{-j\theta} + \frac{1}{2} z^* me^{j\theta} \\ &= m\mathrm{Re}\left\{z^* me^{j\theta}\right\} \\ &= m|z|\cos(\theta - \angle z) \end{aligned} \tag{3.11}$$

where '≡' denotes equality after removing terms that are independent of θ. For the dual-echo field map estimation problem, let

$$\begin{aligned} z &= I_{\text{dual}}(\boldsymbol{r}) I^*_{\text{sep}}(\boldsymbol{r}) / \left|I_{\text{sep}}(\boldsymbol{r})\right| \\ &= \left|M_{\text{dual}}(\boldsymbol{r})\right| e^{j\left\{\angle I_{\text{dual}}(\boldsymbol{r}) - \Delta\hat{\omega}_{\text{sep}}(\boldsymbol{r})\Delta\text{TE}_{\text{sep}}\right\}} + \varepsilon(\boldsymbol{r}) \end{aligned} \tag{3.12}$$

Since the true magnitude of I_{dual} is approximately equal to the observed noisy magnitude of z, we assume $m \approx |z|$. The magnitude and angle of z can be stated as $|z| \approx \left|M_{\text{dual}}(\boldsymbol{r})\right|$ and $\angle z \approx \angle I_{\text{dual}}(\boldsymbol{r}) - \Delta\hat{\omega}_{\text{sep}}(\boldsymbol{r})\Delta\text{TE}_{\text{sep}}$. In reality, $\left|M_{\text{dual}}(\boldsymbol{r})\right|$ is also unknown and is approximated by $\left|I_{\text{dual}}(\boldsymbol{r})\right|$. By having $\theta = \alpha x + \beta$ where x is the frequency encoded readout direction, Eq. (3.11) can be written as follows:

$$
\begin{aligned}
&\log f_Z(z;\theta) \\
&\propto |z|^2 \cos(\angle z - \theta) \\
&= |M_{\text{dual}}|(x)^2 \cos(\angle I_{\text{dual}}(x) - \Delta\hat{\omega}_{\text{sep}}(x)\Delta\text{TE}_{\text{sep}} - \alpha x - \beta) \\
&= |M_{\text{dual}}(x)|^2 \cos(\varphi(x) - \beta)
\end{aligned} \tag{3.13}
$$

where $\varphi(x) = \angle I_{dual}(x) - \Delta\hat{\omega}_{sep}(x)\Delta TE_{sep} - \alpha x$.

Using the identity $\cos(\varphi(x) - \beta) = \cos\beta\cos\varphi(x) + \sin\beta\sin\varphi(x)$, Eq. (3.13) can be expressed as

$$
\begin{aligned}
&\psi(x,\alpha,\beta) \\
&= \sum_{x=1}^{N} |M_{\text{dual}}(x)|^2 \cos(\varphi(x) - \beta) \\
&= \left[\sum_{x=1}^{N} |M_{\text{dual}}(x)|^2 \cos\varphi(x)\cos(\beta)\right] + \left[\sum_{x=1}^{N} |M_{\text{dual}}(x)|^2 \sin\varphi(x)\sin\beta\right]
\end{aligned} \tag{3.14}
$$

where N is the number of pixels used in a readout line. Assuming α can be found via a line search, the maximum likelihood estimator of β can be obtained by taking the derivative of Eq. (3.14) with respect to β as follows:

$$
\begin{aligned}
&\frac{\partial\psi(x,\beta)}{\partial\beta} \\
&= -\left[\sum_{x=1}^{N} |M_{\text{dual}}(x)|^2 \cos\varphi(x)\sin(\beta)\right] + \left[\sum_{x=1}^{N} |M_{\text{dual}}(x)|^2 \sin\varphi(x)\cos\beta\right] = 0 \\
&\Rightarrow \beta = \arctan\left[\frac{\sum_{x=1}^{N} |M_{\text{dual}}(x)|^2 \sin\varphi(x)}{\sum_{x=1}^{N} |M_{\text{dual}}(x)|^2 \cos\varphi(x)}\right]
\end{aligned} \tag{3.15}
$$

In summary, the ML estimator for β in Eq. (3.15) can be substituted into Eq. (3.13) and a line search performed with respect to α to maximize Eq.(3.13). The resultant solution for α is then substituted into Eq. (3.15) to yield a solution for β.

3. 4 Empirical Approximation of β

Table 3.1 reports that while α remained constant over different scans of phantoms on the same scanner, β varied with different scan sessions. This indicates that α has to be estimated only once for a given scanner. As the goal of this study is to be able to compute a field map from the

DEFGRE data directly without the need to acquire additional data for human studies, an empirical method to estimate β was implemented. As the study progressed, β was determined for a new human subject scan by computing the difference between the mean of two-single-echo SPGR off-resonance values, over several homogeneous regions in several previously scanned images from different human subjects, and the corresponding mean DEFGRE off-resonance value of the new subject after linear phase correction with α. This difference is computed in Hz, and β is then estimated by multiplying the off-resonance difference by $2\pi\Delta TE_{dual}$. The two single-echo SPGR off-resonance values of the homogeneous regions across the scanned subjects used to calculate the mean value show little variation (standard deviation of 2.22 Hz).

Table 3.1: Estimated phase correction parameters for phantom data acquired on same scanner using i) DEFGRE and 2D SPGR data with Eq. (3.8) (first two rows), and ii) DEFGRE data and mean 2D SPGR off-resonance value with empirical method.

	Estimated parameters for phantom data		
	Scan 1 (**susceptibility**)	Scan 2 (4 months later) (**susceptibility**)	Scan 2 (4 months later) (**sphere**)
α (rad/ unit distance)	-0.10	-0.10	-0.10
β (rad) using Eq.(3.8)	2.26	0.27	0.11
β (rad) empirical	2.15	0.31	0.12

3. 5 Phantom and Human Subject Data

Along with the homogeneous sphere phantom (17 cm in diameter) filled with Gadolinium-doped water, an air-water phantom (i.e., susceptibility phantom) representing susceptibility changes in a typical human head was imaged. The susceptibility phantom was constructed with a cylinder (13 cm in diameter and 20 cm in height) filled with doped water and a lateral air-column suspended in the middle, which induces inhomogeneity in the static magnetic field. Each phantom was scanned with two pulse sequence protocols: (i) 2D dual-echo fast gradient echo (with readout gradients in opposite polarities) (TR=200 ms, TE1=2.6 ms, TE2=5.3 ms, ΔTE=2.7 ms, image matrix=256x256x68); (ii) twice with single-echo 2D SPGR (TR=200 ms, image matrix=256x256x68) at TE1=2.7 ms and TE2=4.2 ms, where ΔTE=1.5 ms. The slice locations were kept consistent with the dual-echo data. All the above scans were performed twice on each phantom in an interval of four months on the same 1.5 T GE SIGNA MR scanner (GE Medical Systems, Milwaukee, WI).

In addition, data from three different human subjects were acquired over a period of two years after the first phantom scan. The studies were conducted in accordance with the guidelines

set by the University of Michigan Medical School Internal Review Board. Informed consent was obtained from all three subjects. The data were acquired with two pulse sequence protocols: (i) 2D dual-echo fast gradient echo (TE1=2.7 ms, TE2=5.3 ms, ΔTE=2.6 ms, image matrix=256x256x54); (ii) Two single-echo 3D SPGR (TE1=2.4 ms, TE2=4.2 ms, ΔTE=1.8 ms, image matrix=256x256x128). All phantom and human scans were performed on the same scanner.

The first order phase correction terms are useful if they are constant over time for a given scanner and can be applied to yield corrected field maps from dual-echo acquisitions. For phantom data, the corrected field map can be validated with the truth map, i.e., a field map calculated from two separate single echo acquisitions. The constant first order phase correction terms can then be routinely applied to calculate the initial field map from a dual-echo acquisition for the correction of the B_0 inhomogeneity that induces image distortions in clinical human data. The values from the homogeneous phantom regions were used to compute the first order phase correction terms without the effect of the field-inhomogeneity of the sample.

3. 6 Results

Table 3.1 shows that α was consistently estimated to be -0.10 radians/ pixel for all the phantom data from the same scanner. The value of β estimated with Eq. (3.8) however changes for different scans. A surface plot of the cost function in the range $-1.0 \leq \alpha \leq 1.0$ and $-4.0 \leq \beta \leq 4.0$ was computed to verify that the estimated values correspond to global minimum points. Fig. 3.4 shows the true, dual-echo and corrected dual-echo field map profiles of a single column of the sphere phantom in the readout direction. The first order phase error in Fig. 3.4(b) is corrected as observed in Fig. 3.4(c). The third row of Table 3.1 shows the respective values of β computed using the empirical method. It is noted that they closely approximate the β values computed with Eq. 3.8 shown in the second row of Table 3.1. The values of α and β (non-empirical) in Table 3.1 were then used to correct the respective dual-echo field maps of phantoms in each scan session.

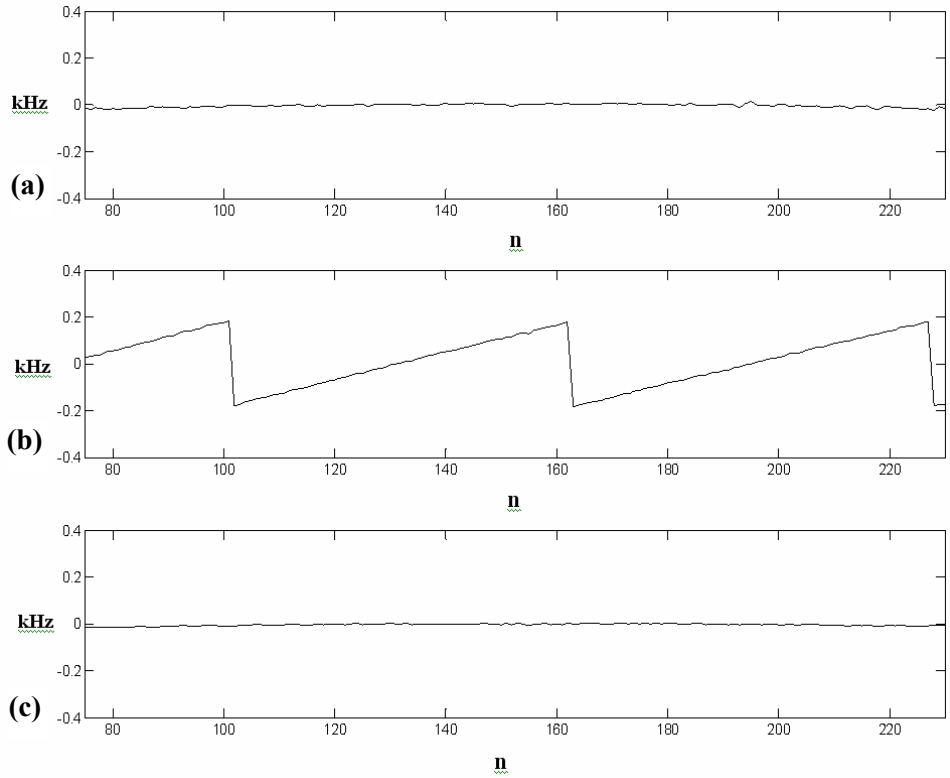

Figure 3.4: A column of the spherical phantom off-resonance map samples in the readout direction for (**a**) standard off-resonance method, (**b**) dual-echo off-resonance method, (**c**) corrected dual-echo off-resonance method.

Figs. 3.5(a-c) show sample slices from the susceptibility phantom from (a) scan time 1 and (b) scan time 2 and (c) sphere phantom from scan time 2. In each sub-figure, the off-resonance maps are shown in rows of sample slices selected from (top) the dual-echo data without correction, (middle) after applying the affine phase correction terms and (bottom) two separate single-echo acquisitions. It is evident that massive phase wrapping in the corrected DEFGRE off-resonance maps in the middle row due to the first order phase shift has been removed.

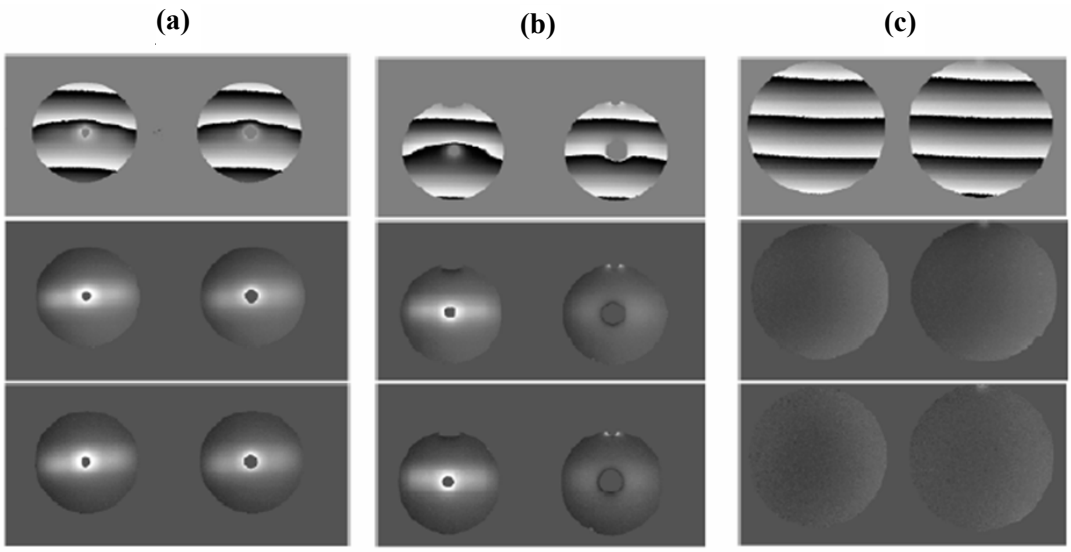

Figure 3.5: Two slices of off-resonance maps in Hz from (top) DEFGRE without correction, (middle) DEFGRE after correction with affine phase term and (bottom) two separate single-echo acquisitions for (**a**) susceptibility phantom in scan 1, (**b**) susceptibility phantom in scan 2 (acquired 4 months after scan 1), (**c**) sphere phantom in scan 2. Quantitative results for entire volumes are shown in Table 3.2.

The root-mean-square error (RMSE) values between the dual-echo and corrected dual-echo field maps, and the ground truth field maps over all 68 slices in each phantom scan are shown in Table 3.2. The relatively low RMSE values (ranging from 0.17 ppm to 0.43 ppm) for the corrected dual-echo off-resonance maps strongly suggest that the affine phase error model is suitable for field map estimation with the dual-echo pulse sequence in Fig. 3.2.

Table 3.2: Off-resonance RMSE values in Hz and ppm (B_0=1.5 T) between each phantom's corrected dual-echo field map (using parameters computed in Table 3.1) and corresponding field maps computed with the standard field map method (using 2D SPGR data). Only pixels with MR image intensity values above 10% of the maximum image intensity of the respective datasets are used in the computation of the RMSE values.

RMSE (Hz, ppm)		
Scan 1 (**susceptibility**)	Scan 2 (4 months later) (**susceptibility**)	Scan 2 (4 months later) (**sphere**)
27.26 Hz, 0.43 ppm	23.43 Hz, 0.37 ppm	11.16 Hz, 0.17 ppm

Results from the three human subject scans confirm that the same value of α obtained in Table 3.1 gives good correction results for the same scanner over a period of two years. Prior to obtaining empirical approximations of β, the mean off-resonance value of homogeneous regions

of three human subject brains over 10 slices each, $f_{sep,mean}$, was computed to be 18.89 Hz. The DEFGRE off-resonance map for each subject was corrected with the first order phase term α, and the mean off-resonance values, $f_{dual,mean,1}$, $f_{dual,mean,2}$ and $f_{dual,mean,3}$, of corresponding homogeneous regions over 10 slices of the resultant data were computed to be 165.54 Hz, -130.30 Hz and 188.84 Hz, respectively. The corresponding value of β (radians) for the i^{th} subject is obtained by $\beta_i=2\pi(f_{sep,mean}- f_{dual,mean,i})\Delta TE_{dual}$, which yield β_1=-2.40 rad, β_2=2.44 rad and β_3=-2.78 rad for the three subjects, respectively. Table 3.3 shows that the RMSE values for the corrected DEFGRE using the empirically determined values of β, compared to the reference 3D SPGR off-resonance maps, are relatively low (ranging from 0.44 ppm to 0.53 ppm), indicating that the corrected off-resonance maps are close to the 3D SPGR off-resonance maps. This RMSE comparison is performed to determine if the empirically computed values of β have corrected most of the zero order phase shift. Only pixels having significant MR signal (i.e., image intensity values above 10% of the maximum image intensity value)) were used in computing the RMSE.

Table 3.3: Off-resonance RMSE values in Hz and ppm (B_0=1.5 T) between each human subject's corrected dual-echo field map (using α=-0.10 with β computed empirically for each scan) and corresponding field maps computed with the standard field map method (using 3D SPGR data). Only pixels with intensity values above 10% of the maximum image intensity of the respective datasets are used in the computation of the RMSE values.

RMSE (Hz, ppm)		
Subject 1	Subject 2	Subject 3
33.88 Hz, 0.53 ppm	27.98 Hz, 0.44 ppm	32.03 Hz, 0.50 ppm

Fig. 3.6 shows DEFGRE off-resonance map slices for three of the subjects before and after the affine phase correction with empirically determined values of β. It is observed that the zero and first order phase errors have been largely removed after the phase correction procedure.

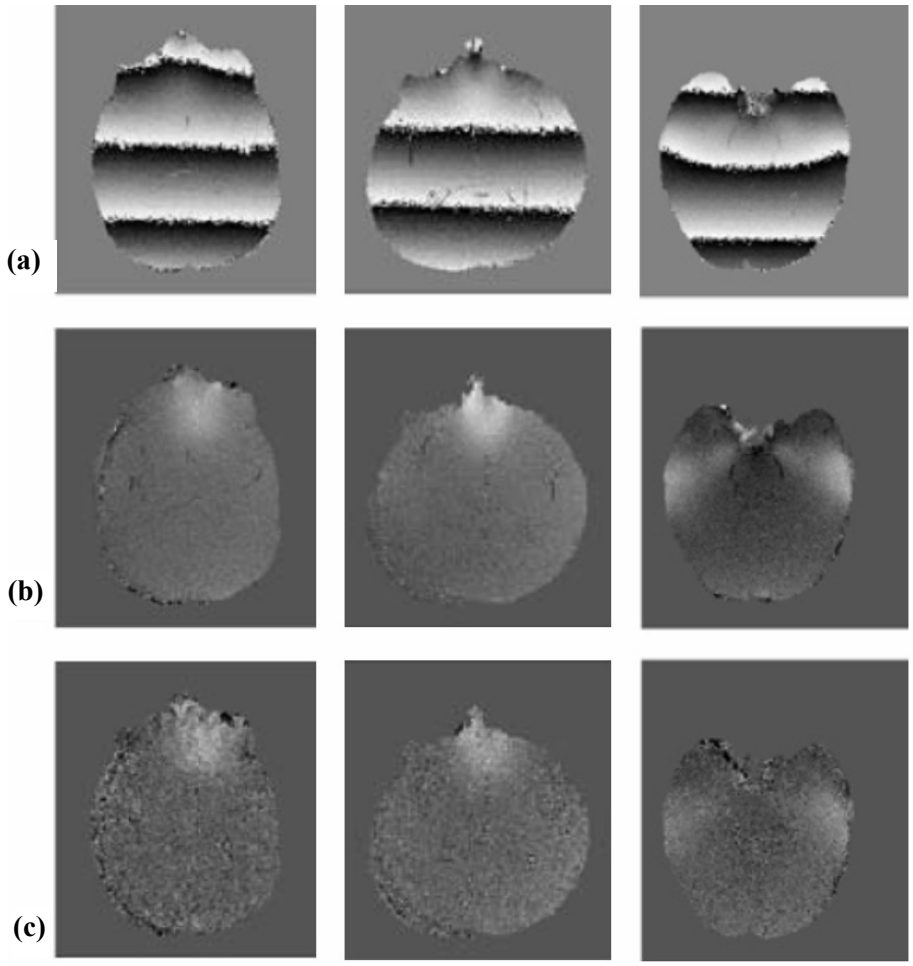

Figure 3.6: Subject 1 (first column), subject 2 (second column) and subject 3 (third column) off-resonance slices from (**a**) uncorrected DEFGRE data (direct application of Eq. (3.7)), (**b**) DEFGRE field map corrected with affine phase term (empirically determined β), (**c**) standard 2 single-echo 3D SPGR data. Note that the linearly varying phase error in (**a**) has been removed in (**b**). Part (**a**) is displayed on a scale from -1500 Hz to 1500 Hz while (**b**) and (**c**) are both displayed on a scale from -100 Hz to 200 Hz.

3. 7 Discussion

The first order phase correction term α was computed with field maps generated from phantom data acquired with a single echo SPGR at two different echo times and a dual-echo sequence, and was used to remove the linearly varying phase error in field maps acquired using the same dual-echo protocol on the same scanner. The correction was tested on multiple sets of human brain data as well as phantom data that exhibit susceptibility artifacts. The results show that α was observed to be constant on the same scanner over a period of two years. The computation process is straightforward and no elaborate phase unwrapping is required to correct for the first order component of the phase error. The estimation of α on each scanner needs to be done only once

and can be used to perform field map estimation with dual-echo data thereafter. In the event that the scanning environment changes, the recalibration can be done by following the simple protocol set up to acquire data with the two single-echo GRE and DEFGRE sequences using a homogeneous spherical phantom.

Although the zero order phase term β varies with different scan sessions, we have proposed an empirical method to approximate it using only DEFGRE data and an average off-resonance value computed from suitable homogeneous regions of objects previously scanned with the two single-echo SPGR protocol on the same scanner. This empirical method yielded corrected DEFGRE off-resonance maps that had relatively low off-resonance RMSE values ($\leq$0.53 ppm for human subjects at B_0=1.5 T). As stated previously, the off-resonance maps computed with the two single-echo acquisitions are prone to motion artifacts since the data are acquired from two separate echoes. Thus, the RMSE values for the human subject data are meant to be approximations of how close the corrected DEFGRE off-resonance maps are to the standard off-resonance maps, but not measures of accuracy in the corrected DEFGRE field maps. This is useful information only because, in the absence of a ground truth field map without motion, it shows that the corrected DEFGRE estimates do not deviate significantly from the standard field map. For the phantom data, the field maps computed using the standard method is a closer approximation to the ground truth field map since the phantoms do not move during the scans. Thus, using the standard field maps as ground truth field maps, the RMSE values of phantom dual-echo data after phase shift correction are better measures of the accuracy of the corrected DEFGRE method.

Other factors like the different field map SNR values obtained with different ΔTE values used in the 3D SPGR and DEFGRE protocols may influence the accuracy of the RMSE values. It is observed that the field maps computed using the two separate single echo acquisition method are noisier than the corrected DEFGRE field maps. This is true for both phantom and human data. For the phantom experiments, the standard deviation values of homogeneous field map regions, which approximate the field map noise levels, were 4.9, 6.0, 6.9 Hz for single echo while the values for the corresponding regions in the respective dual-echo datasets were 3.15, 0.4, 4.3 Hz. Similarly, the human field map measurements were 20.6, 24.2, 19.7 Hz for single echo and 15.6, 12.5, 11.6 Hz for dual-echo experiments. Among other reasons, this phenomenon may be due to $\Delta TE_{dual} > \Delta TE_{sep}$ combined with motion-induced noise. The human subjects' noise standard deviation values are larger than phantom noise standard deviation values which may be attributed to additional noise sources in humans, i.e., motion, body thermal noise, etc. Performing a future field map SNR study of phantom (with and without motion) and human data with $\Delta TE_{dual} = \Delta TE_{sep}$

may aid in quantifying any motion-related SNR gain in using the DEFGRE field map estimation method compared to the standard field map method.

It is ideal to keep the ΔTE values equal in order to be able to compare SNRs in field maps fairly. For field map measurements, ΔTE was kept as close as possible for the standard and dual-echo sequences while avoiding spontaneous changes in other acquisition parameters due the scanner's built-in timing restrictions in choosing values for TE. Our key motive was to use the DEFGRE sequence for field map estimation as it was with the limitations in sequence timing included, and results strongly suggest that the affine phase error model holds over time (two years).

3. 8 Conclusions

The dual-echo bipolar readout gradient technique offers an efficient way of collecting data and computing static field maps with reduced motion-induced errors compared to the widely used, two separate single echo acquisition method. The affine parameters modeling the phase error inherent in the dual-echo bipolar readout gradient technique is estimated with data from a phantom of homogeneous medium where the field-inhomogeneity is mainly system-induced. The estimated phase correction parameters are then applied to DEFGRE data of an air-tissue susceptibility phantom. Results have shown that the first order phase error term stays constant with time as expected with the same scanner using the same DEFGRE protocol parameters, allowing the technique to be used for human subject field map estimation once the first order phase error term has been characterized. The first order term is due to the readout imbalance which is scanner dependent and yields similar *k*-space shifts in each readout line acquired with the dual-echo acquisition. The zeroth order term has off-resonance contributions from other sources such as heating effects of coils depending on the object being scanned. The phase error from the zeroth order term changes with different scan sessions but can be estimated empirically using the previously scanned two-single echo field maps. The proposed method has been tested on three human subjects and the results strongly suggest that the DEFGRE pulse sequence can yield good field map estimates. The relatively low RMSE values (ranging from 0.17 ppm to 0.43 ppm) for the corrected dual-echo off-resonance maps at 1.5 T suggest that the affine phase error model is suitable for field map estimation with the dual-echo pulse sequence. Since the first order correction term depends largely on how the readout gradient switches and not on how strong the B_0 field is, an affine phase error model is expected to hold for images from different field strengths. The value of the linear phase term may be different for different scanners but should be constant for any one scanner. Future work includes an evaluation of the proposed field map

estimation method at 3 T and the investigation of methods to improve the reliability of the zero order phase error estimate.

CHAPTER 4

Concurrent Field Map and Map-Slice-to-Volume (CFMMSV) Motion Correction for EPI

A popular method of estimating field-inhomogeneity involves scanning the sample at two different echo times with a T_2*-weighted pulse sequence (e.g. GRE) and computing the phase difference divided by the echo time difference. This is typically done once in the beginning or the end of an fMRI experiment. This method may be insufficient for two reasons. First, the acquired field map is spatially inaccurate in the presence of motion between the two echoes. Secondly, the acquired static field map does not account for head motion during the acquisition of the fMRI time-series. Dynamic field map estimation methods such as partial *k*-space methods are robust to subject motion but may either reduce the temporal resolution of fMRI images or the spatial resolution of the field maps [9].

The objective of this section is to propose a concurrent motion and field-inhomogeneity correction framework in which the effects of head motion on the field map (and hence geometric distortion) are accounted for. The slice-profile warp is ignored in this section. The concurrent field map and MSV (CFMMSV) correction framework uses iterative reconstruction and MSV registration. The key difference in the following methods within this framework revolves around the dynamic field map update method.

Our previously reported CFMMSV method [13] attempted to estimate dynamic field maps from an initially collected field map using the MSV rigid body motion parameters obtained by registering the EPI time-series to a 3D anatomical dataset. This method does concurrent field-inhomogeneity and slice motion correction using only one field map but is unable handle larger out-of-plane rotations. This is because rigid body transformation of a field map does not accurately describe the true field map changes with out-of-plane motion. Preliminary results on simulated data show that the final reconstructed image quality and estimated motion parameters improve in accuracy compared to a conventional non-concurrent correction scheme.

4.1 Introduction

In functional MRI (fMRI) studies, activation maps are generated after statistical analyses of voxel intensity changes between stimulus and rest images of echo-planar imaging (EPI) time series data. The accuracy of measuring these intensity changes, which are typically in the range of 1% to 4%, is severely degraded in the presence of head motion. To compensate for the voxel shifts with head motion, some studies employ in-plane and volumetric image registration techniques on EPI time series data [30-33]. Besides image alignment errors caused by head motion, single-shot EPI data acquired in a Cartesian *k*-space grid is also sensitive to magnetic susceptibility(χ)-induced geometric distortions, especially for the mid to lower brain regions with air-tissue and bone-tissue interfaces. Subject motion causes image shifts as well as field-map changes which result in time-varying local changes in geometric distortion [34,35]. Consequently, inconsistencies in voxel positions across the time series images result in inaccurate statistical testing of the signal changes in response to the given tasks in activation studies.

In fMRI, geometric distortion correction is typically performed with a static field-map independently of motion correction [4,35], thus ignoring field-map changes caused by head motion. A prospective approach to this problem is to acquire field-maps simultaneously with EPI data during an fMRI experiment to track temporal field-inhomogeneity changes by collecting additional *k*-space data [9,10]. However, acquisition of extra *k*-space data within reasonable time may pose some limitations in field-map resolution since, to reduce scan time, the extra data acquired is typically constrained to a low-pass filtered or truncated version of a full set of EPI image *k*-space data. Also, modifying pulse sequences may not be an available option in many clinical scanners. In addition, some of the algorithms for image reconstruction and post-processing are computationally intensive [10]. A correction strategy [36] based on the work done by Chang and Fitzpatrick [37] is of notable interest since no field-maps are required a priori. Instead, pairs of EPI images are acquired with opposing blipped phase encode (PE) gradient polarity, thus yielding image pairs with identical geometric distortion but in opposite directions along the PE axis. The deformation field between each pair of images, from which the dynamic field-map is computed, is estimated from the images' intensity values. However, to acquire the pairs of EPI images, pulse sequence modification is required, and motion-induced field-map changes may occur between the acquisitions. This may lead to local differences in geometric distortion in each pair of images, especially in regions with susceptibility-induced field-inhomogeneity, which may yield inaccurate field-map estimates. Another retrospective correction method [34] adopts a least squares approach and models the temporal change in B_0 using a Taylor

series expansion with respect to motion parameters. Qualitative results indicate good correlation between estimated and measured parameters. This model was designed for registration and geometric distortion correction of mono-modality EPI time series images with a pre-selected EPI volume as a reference volume. An anatomically correct structural volume was not used for registration.

Previously, in our group, a realistic motion-correction approach by mapping a slice-to-volume (MSV) for multi-slice EPI time series was developed [25]. This technique, which uses negated mutual information as the similarity cost metric, allows individual slices in the time series to be mapped to an anatomically correct reference volume, and has demonstrated a capability to accurately correct image shifts due to 3D rigid head motion. Compared to the widely used volumetric registration of EPI volumes, which assume no inter-slice motion, the MSV approach improved sensitivity and specificity in localizing activated regions [25]. While the rigid-body transformation function may be sufficient for activation localization in the sensorimotor cortex, geometric distortions in EPI slices acquired from the mid to lower brain regions cause difficulty in localizing activations, which makes language studies with fMRI difficult. Consequently, MSV was expanded to include a non-linear warping function for the studies involving activations in mid brain regions [38,39]. This improvement comes with increased computational cost due to the longer optimization process associated with higher degrees of freedom (DOF) in registration.

In this work, we developed a concurrent MSV and field inhomogeneity correction framework for EPI time series images [13]. The concurrent field-map MSV (CFMMSV) method employs iterative field-corrected quadratic penalized least squares (QPLS) image reconstruction [25] followed by a field-map update to enhance the MSV rigid body motion-correction scheme, therefore accounting for field-inhomogeneity changes with inter-slice head motion [5]. The proposed method consists of iterative correction cycles, each with a pair of QPLS image reconstruction and MSV motion correction stages. In each cycle, dynamic field-map slices are re-sampled from a high resolution 3D static field-map that has been spatially transformed by a rigid body transformation function determined by MSV for the respective EPI slices. Since geometric distortion is incrementally corrected in the QPLS stage after each field-map update, a rigid body MSV motion model is expected to be sufficient and computationally less expensive than non-linear MSV registration. Results from two sets of realistically simulated EPI time series with different ground truths for rigid body motion, image intensities and activation regions show that the CFMMSV method improves the accuracy of the estimated motion parameters and reconstructed images when compared to a strategy that performs geometric distortion and motion

correction independently using just a static field-map. Non-parametric random permutation tests were also performed on all datasets at various stages in the CFMMSV correction process to compute activation detection receiver operating characteristic (ROC) curves. The areas under these ROC curves show that the CFMMSV method improves the activation detection accuracy.

4.2 Background

4.2.1 EPI Geometric Distortion

In brain EPI data that is reconstructed without field-inhomogeneity correction, geometric distortion is observed in regions where the local magnetic field is inhomogeneous, especially at the boundaries of tissues with significant magnetic susceptibility differences. Head motion that changes the orientation of the inter-tissue boundary with B_0 (out-of-plane rotations) may induce significant field-inhomogeneity changes in the region around the boundary. Translations and in-plane rotation are less likely to cause such changes in the susceptibility-induced component of the field-map. Such motion mainly induces shifts and in-plane rotation of the entire field-map. In blipped EPI, due to the long readout time, field-inhomogeneity causes pixel shifts mainly in the phase encode direction [2] as shown in Eq. (2.7). These space-variant pixel shifts depend on the EPI slice readout time $T_{readout}$ and the field-inhomogeneity map. The resultant geometric distortion and image intensity errors can adversely affect fMRI activation detection performance.

4.2.2 Iterative Field-Corrected Reconstruction

To perform geometric distortion correction, we use the iterative field-corrected reconstruction method [5] described in Chapter 2. The continuous object f and field-map $\Delta\omega$ are parameterized into a sum of weighted rect functions $\phi(\boldsymbol{r}-\boldsymbol{r}_n)$ where $\boldsymbol{r}$ is the vector of spatial coordinates. Some of the equations from Chapter 2 are reproduced here to specifically denote the correction of EPI time series image slices. Ignoring spin relaxation and assuming uniform receiver coil sensitivity, the parameterized MR signal equation of slice frame l in an EPI time series is

$$\begin{aligned} u^l(t_m) &= s^l(t_m) + \varepsilon^l(t_m) \\ &\approx \Phi(\boldsymbol{k}(t_m)) \sum_{n=0}^{N-1} f_n^l e^{-j\Delta\omega_n^l t_m} e^{-j2\pi(\boldsymbol{k}(t_m)\cdot\boldsymbol{r}_n)}, \qquad l = 0 \ldots L-1 \end{aligned} \tag{4.2}$$

where $s^l(t_m)$ is the baseband MR signal sample at time t_m during readout, $\varepsilon^l(t_m)$ denotes white Gaussian noise [20], $\Phi(\boldsymbol{k}(t_m))$ denotes the Fourier transform of $\phi(\boldsymbol{r})$, N is the number of pixels in a slice, L is the total number of slice frames in the EPI time series and f_n^l and $\Delta\omega_n^l$ are the object

intensity and field-inhomogeneity values, respectively, at $\boldsymbol{r}_n$. The matrix-vector form of Eq. (4.2) can be written as follows:

$$\boldsymbol{u}^l = \boldsymbol{A}^l \boldsymbol{f}^l + \boldsymbol{\varepsilon}^l \tag{4.3}$$

where $\boldsymbol{f}^l = (f_0^l, .., f_{N-1}^l)$ and elements of the $M \times N$ system-object matrix $\boldsymbol{A}^l$ are

$$a_{m,n}^l = \Phi(\boldsymbol{k}(t_m)) e^{-j\Delta\omega_n^l t_m} e^{-j2\pi(\boldsymbol{k}(t_m)\cdot\boldsymbol{r}_n)} \tag{4.4}$$

To estimate the unknown object slice $\boldsymbol{f}^l$ from the observed k-space data, the iterative conjugate gradient algorithm is used to minimize the QPLS cost function

$$\Psi_1(\boldsymbol{f}^l) = \left\|\boldsymbol{u}^l - \boldsymbol{A}^l \boldsymbol{f}^l\right\|^2 + \beta\left\|\boldsymbol{C}\boldsymbol{f}^l\right\|^2 \tag{4.5}$$

where $\boldsymbol{C}$ is a first-order difference matrix, and β is a parameter that controls the tradeoff between obtaining a data-consistent estimate and a smoothed, regularized estimate. The QPLS estimate of $\boldsymbol{f}^l$ is

$$\hat{\boldsymbol{f}}_{QPLS}^l = \arg\min_f \Psi_1(\boldsymbol{f}) = [\boldsymbol{A}^{l*}\boldsymbol{A}^l - \beta\boldsymbol{C}^*\boldsymbol{C}]^{-1}\boldsymbol{A}^{l*}\boldsymbol{u}^l, \tag{4.6}$$

however, we minimize Eq. (4.5) using the conjugate gradient algorithm instead of evaluating Eq. (4.6) directly.

To accurately perform field-corrected reconstruction in the presence of head motion, every slice of observed data $\boldsymbol{u}^l$ should be paired with a dynamic field-map slice $\Delta\omega^l$ that describes the field-inhomogeneity at frame l of the fMRI experiment. Typically, however, only a static field-map $\Delta\omega_{\text{static}}$ is available. This field-map is usually acquired before or after the experiment and does not track field-inhomogeneity changes during the acquisition of the fMRI time series images. Each volume in the EPI time series typically has a lower spatial resolution and larger slice thickness than $\Delta\omega_{\text{static}}$. A simple approach to obtain field-corrected fMRI images is to register each time series volume to the image intensity volume acquired in the same coordinate space as the static field-map volume, and then use re-sampled slices of $\Delta\omega_{\text{static}}$ in place of $\Delta\omega^l$ in

minimizing Eq. (4.5). This correction method ignores inter-slice motion and field-inhomogeneity changes due to head motion and thus yields potentially significant image reconstruction errors.

4.2.3 Map Slice-To-Volume (MSV) Registration in fMRI

The MSV motion correction technique [25] models the 3D motion of multislice EPI data by allowing each slice to have its own six DOF motion. To perform MSV motion correction for fMRI time series images, each reconstructed EPI slice $\boldsymbol{f}^l$ is registered with a 3D reference volume $\boldsymbol{g}_{\text{ref}}$ using the six DOF rigid body transform denoted by T_{α^l}. The vector $\boldsymbol{\alpha}^l$ consists of the six MSV motion parameters t_x, t_y, t_z, θ_x, θ_y, θ_z for slice l. This is performed by minimizing a function $\Psi_2(\boldsymbol{\alpha}^l)$ that measures the dissimilarity between $\boldsymbol{f}^l$ and $\boldsymbol{g}_{\text{ref}}$. In the implementation of MSV, the negated mutual information (MI) is used, which performs well for multi-modality datasets, i.e. T_2^*-weighted EPI slices registered with a T_1-weighted reference volume. The motion parameters $\boldsymbol{\alpha}^l$ are estimated by minimizing the following cost function over $\boldsymbol{\alpha}^l$ using the Nelder-Mead downhill simplex optimization algorithm

$$\Psi_2(\boldsymbol{\alpha}^l) = -\text{MI}(\boldsymbol{g}_{ref}, \boldsymbol{f}^l(T_{\boldsymbol{\alpha}^l}(\boldsymbol{r}))) \tag{4.7}$$

Each set of optimized motion parameters is then used to transform and interpolate (trilinear) its respective slice $\boldsymbol{f}^l$ into a volume with the same spatial coordinates as the reference volume. In the original MSV method, the motion of each slice is computed independent of other slices and allows six DOF between each slice acquisition. For single shot acquisition, intra-slice motion is negligible. Given that head motion is typically correlated in time and that MSV may generate outlier estimates, especially for top slices where the information content is reduced, we apply temporal median filtering on the recovered MSV motion parameters before use. A median filter was chosen because the MSV motion estimates obtained from data with simulated smooth motion were observed to track the ground truth except for intermittent outlier estimates. Fig. 4.1 shows a motion parameter recovered from a 120-volume simulated EPI time series using MSV alone and MSV with a nine point median filter. The ground truth is also plotted. The RMSE values of the raw and median filtered MSV results in Fig. 4.1 are 1.10mm and 0.19mm, respectively.

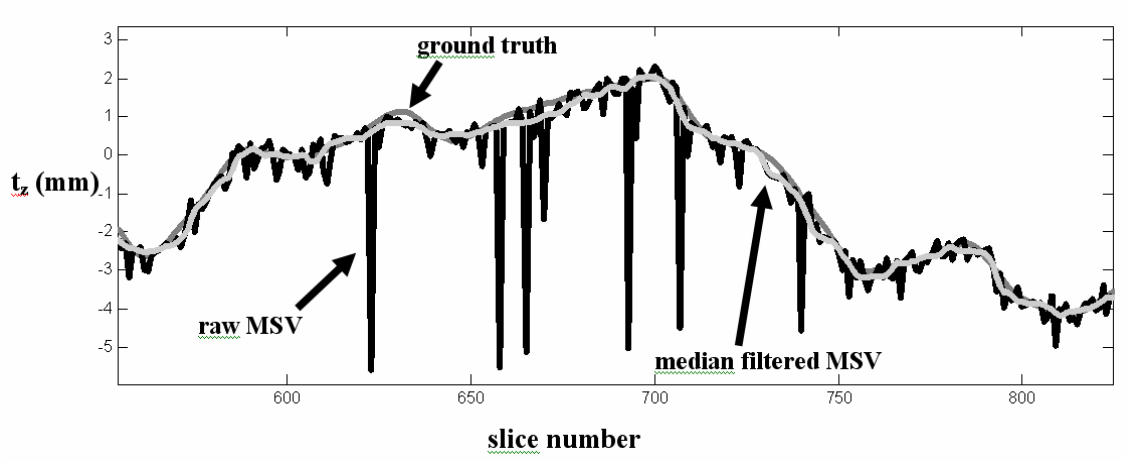

Figure 4.1: Recovered raw MSV motion estimates, median filtered MSV motion estimates and ground truth of a subset of simulated dataset A with applied translation in the *z* direction. The RMSE values of raw MSV and median filtered MSV results are 1.10mm and 0.19mm respectively. The standard deviation values of the estimation error for raw MSV and median filtered MSV are 1.06mm and 0.13mm respectively.

4.3 Concurrent Field-inhomogeneity Correction with MSV

To design a concurrent correction technique that involves Eqs. (4.5) and (4.7) with a rigid body transformation function, the main challenge is the approximation of the dynamic field-map from the initial static field-map. To partially account for field-map changes due to 3D head motion during the fMRI experiment, we propose and evaluate the following "concurrent" correction approach. The concurrent field-map and MSV motion correction framework (CFMMSV) loops through several correction cycles, each of which consists of a field-corrected reconstruction stage followed by MSV registration. The changing field-map is approximated using the recovered MSV motion estimates and the static field-map. As the number of correction cycles increases, the geometric distortion is incrementally corrected in the image reconstruction stage. Thus, a rigid body transformation function in MSV is expected to be sufficient to correct for head motion. This leads to a faster image registration process compared to the use of 3D non-linear warping functions.

Since the true dynamic field-map $\Delta\omega^l$ in Eq. (4.4) is unavailable, the EPI time series image reconstruction in the *initial cycle* ($\kappa = 0$) of the concurrent correction algorithm is performed with the static field-map volume $\Delta\omega_{\text{static}}$. The elements of the system matrix $\boldsymbol{A}^{l,\kappa=0}$ can be written as

$$a_{m,n}^{l,\kappa=0} = \Phi(\boldsymbol{k}(t_m))e^{-j\Delta\omega_{n,static}^{l}t_m}e^{-j2\pi(\boldsymbol{k}(t_m)\cdot\boldsymbol{r}_n)} \tag{4.8}$$

where κ denotes the correction cycle number. The first field-corrected estimate of slice frame l, $\hat{\boldsymbol{f}}^{l,\kappa=0}$, is then obtained by minimizing Eq. (4.5) with $\boldsymbol{A}^{l}= \boldsymbol{A}^{l,\kappa=0}$. The reconstructed slices are then registered via MSV to the reference volume $\boldsymbol{g}_{\text{ref}}$ by minimizing Eq. (4.7). Each set of median filtered motion parameters $\hat{\boldsymbol{\alpha}}_{filt}^{l,\kappa}$, $l = 0,..,L\text{-}1$, is applied to the original static field-map volume and the respective slice within the transformed field-map volume is re-sampled and stacked into a new field-map volume

$$\Delta\hat{\omega}^{l,\kappa+1} = H^{l}\left\{\omega_{static}(T_{\hat{\boldsymbol{\alpha}}^{l,\kappa}}(\boldsymbol{r}))\right\},\ l = 0,..,L\text{-}1, \tag{4.9}$$

where $H^{l}\{U\}$ denotes an operator which re-samples slice l from a volume U. This updated field-map is then used in the next cycle to reconstruct field-corrected images again from the original k-space data.

Since geometric distortion in EPI is predominantly in the PE direction, the recovered MSV motion parameters in the phase encoding direction are *not* used to transform the static field-map in the initial field-map update when $\kappa = 0$. This is because the EPI image shifts in the PE direction may be largely influenced by field-inhomogeneity induced geometric distortion rather than object motion. In addition, the field-map may change significantly with out-of-plane rotations which would render these motion parameters unreliable for the initial field-map update. Thus, for $\kappa = 0$, the motion parameters t_y (translation in PE direction), θ_x and θ_y (out-of-plane rotations) are omitted when applying the transformation $T_{\hat{\boldsymbol{\alpha}}^{l,\kappa=0}}$ to the static field-map. For the following cycles, $\kappa \geq 1$, all six DOF are used when applying $T_{\hat{\boldsymbol{\alpha}}^{l,\kappa}}$ to update the field-map. The original raw data $\boldsymbol{u}$ and static field-map $\Delta\omega_{\text{static}}$ are used in each cycle to approximate the dynamic field-map and field-corrected EPI images to avoid error propagation due to intermediate processing steps as the number of cycles increases. The CFMMSV method is summarized as follows:

Algorithm. *Concurrent QPLS-MSV for EPI Motion and Field-Inhomogeneity Correction*
Initial data: $\Delta\hat{\omega}^{l,\kappa=0}$ *(slice l of static field-map* $\Delta\omega_{\text{static}}$*),* u^{l} *(k-space data), l=0...L-1*
for κ*=0...K (correction cycles)*
Step 1: $\hat{\boldsymbol{f}}^{l,\kappa} = \arg\min_{\boldsymbol{f}}\left\|\boldsymbol{u}^{l} - \boldsymbol{A}(\Delta\hat{\omega}^{l,\kappa})\boldsymbol{f}\right\|^{2} + \beta\left\|\boldsymbol{C}\boldsymbol{f}\right\|^{2}$ *do for l=0...L-1 (**QPLS**)*

Step 2: $\hat{\boldsymbol{\alpha}}^{l,\kappa} = \arg\min_{\boldsymbol{\alpha}} \left\{ -MI(g_{\text{ref}}(\boldsymbol{r}), \hat{f}^{l,\kappa}(T_{\boldsymbol{\alpha}}(\boldsymbol{r})) \right\}$ *do for l=0…L-1* ***(MSV)***

Step 3: Median filter $\hat{\boldsymbol{\alpha}}^{\kappa}$ *to obtain* $\hat{\boldsymbol{\alpha}}^{\kappa}_{\text{filt}}$.

Step 4: $\Delta\hat{\omega}^{l,\kappa+1} = H^{l}\left\{ \Delta\omega_{\text{static}}(T_{\hat{\boldsymbol{\alpha}}^{l,\kappa}_{filt}}(\boldsymbol{r})) \right\}$ *do for l=0…L-1* ***(resample slice l)***

end

4.4 Motion, Functional Activation and Geometric Distortion Simulation in EPI Time Series

To evaluate the effectiveness of the CFMMSV method in recovering accurate motion parameters, forming accurate field-corrected intensity images and detecting functional activation regions, two time series datasets, labeled A and B, were simulated with different applied motion. The ground truths available for head motion, activation regions and non-distorted image intensities allow for a precise evaluation of the correction method. To simulate the datasets, we start with two perfectly registered T_1- and T_2-weighted image datasets (matrix size: 256×256×124, voxel size: 0.8mm×0.8mm×1.5mm) derived from International Consortium of Brain Mapping (ICBM) data. The T_1 volume is used as the anatomical reference for MSV registration and the T_2 volume forms the "baseline" volume from which the time series datasets are simulated. To simulate functional activation, an "activated" T_2 volume was created by increasing the T_2 ICBM dataset intensity by 5% in pre-defined ellipsoidal regions as shown in Figs. 4.8(e) and 4.8(j). Six baseline-activation cycles, each of which was formed by concatenating ten baseline and ten activated T_2 volumes, were assembled to form a 120-volume time series. In addition, a simulated brain static field-map was created by adding three 3D Gaussian blobs located at the inferior frontal and temporal lobes to a 3D third-order polynomial (Fig. 4.2). This field-map was scaled such that the off-resonance values range from -64 Hz to +320 Hz to simulate a maximum field-inhomogeneity of 5 ppm at 1.5 T.

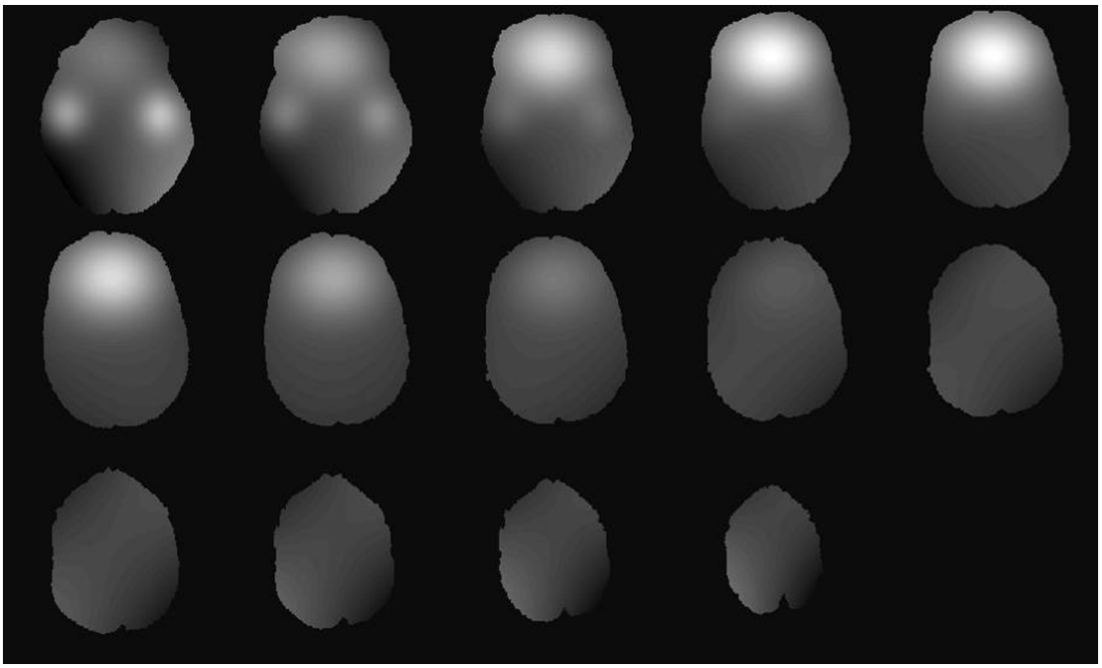

Figure 4.2: Simulated field-map slices from a single volume with significant field-inhomogeneity near frontal lobe and inferior temporal lobe regions. Field-map values range from -64 Hz to +320 Hz to simulate a maximum field-inhomogeneity of 5 ppm at 1.5 T.

Dataset A is a geometrically distorted EPI time series with simulated motion in t_x, t_y, t_z and θ_z (translations and in-plane rotation) while dataset B is a geometrically distorted EPI time series with simulated motion in θ_x, θ_y and θ_z (rotations). To generate dataset A, temporally smooth translational and in-plane rotational motion (t_x, t_y, t_z and θ_z) were applied to both the T_2-weighted baseline-activation time series and simulated field-map volumes. Sequential 5.6 mm thick slices were then re-sampled to form 120-volume intensity and field-map time series datasets (volume matrix size: 128×128×14). Each re-sampled slice has its own set of motion parameters. The applied motion has maximum values of 7.20 mm, 8.00 mm, 3.51 mm and 4.70° for t_x, t_y, t_z and θ_z, respectively. The T_2-weighted volumes obtained are henceforth referred to as the time series image intensity ground truth without geometric distortion. These are used to compute the image normalized root mean square error (NRMSE) values at various correction cycles to measure the accuracy of the field-corrected reconstructed images. The applied motion does not change the orientation of the air-tissue interface with respect to B_0 and thus is unlikely to change the field-map significantly except for the respective translation or in-plane rotation. Thus, forward distorting the T_2 volume with the rotated-translated field-map is reasonable as long as out-of-plane rotations θ_x and θ_y are not applied. However, to test the effectiveness of the CFMMSV framework in the presence of out-of-plane motion while assuming the field-map moves with a

rigid body transformation function together with the head, a second pair of 120-volume time series intensity and field-map datasets (dataset B) were simulated with temporally smooth motion in three rotation parameters θ_x, θ_y and θ_z. This assumption, while simplistic in the presence of large out-of-plane motion, provides a way to generate an otherwise realistic time series dataset with out-of-plane motion and subsequent field-inhomogeneity induced geometric distortion. The simulated rotational motion has maximum values of 5.0°, 8.6° and 8.1° for θ_x, θ_y and θ_z respectively. Slice acquisition interleaving was incorporated when generating both time series datasets.

To forward distort the T_2 time series images from both datasets, simulated blipped EPI Cartesian *k*-space data of the distorted images were generated in conjunction with the respective field-map time series with motion using Eq. (4.2). The distorted images (Fig. 4.3(b)) were then reconstructed from this *k*-space data using a system-object matrix with a field-map set to zero [13]. The simulated readout time was 43.8 ms and the pixel bandwidth in the PE direction was 22.8 Hz. In subsequent sections, datasets A and B will refer to the final geometrically distorted time series with the respective applied motion.

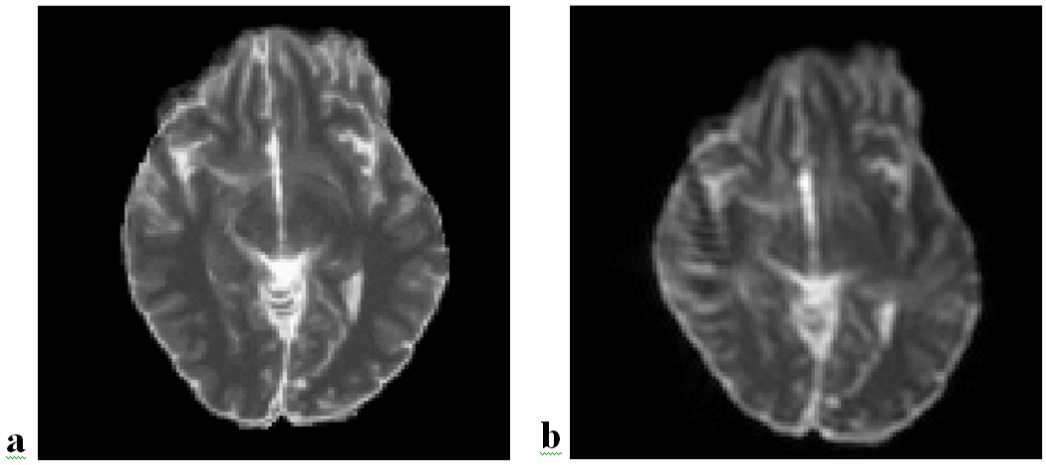

Figure 4.3: (**a**) T_2 ICBM slice before simulated geometric distortion. (**b**) T_2 ICBM slice after simulated geometric distortion with a peak field-inhomogeneity of 5 ppm at 1.5 T.

4.5 Activation Detection with Random Permutation Test

After re-positioning all the EPI time series slices into volumes, MSV yields time series volumes that may have empty voxels. This results in variable sample sizes for different voxels for statistical analysis. The non-parametric statistical method of voxel-wise random permutation, using the averaged difference between activation and rest images as the test statistic, was used for

significance testing of differences in voxel intensities in the simulated datasets [25,40]. This statistical technique is simple, robust and independent of sample size variability [41]. Random draws of 2000 permutations of activated and rest periods were used to form a permutation distribution for each voxel from which activated regions are identified by testing the null hypothesis of no activation at a fixed threshold of $\alpha = 0.001$. To obtain ROC curves, we vary the threshold P values from 10^{-4} to 1.0 to obtain a set of activation maps and, together with the ground truth activation map, compute the true positive and false alarm rates. The area under each ROC curve (AUC) is used to measure how accurately the activation regions have been detected.

4.6 Results

In our experiments, the concurrent correction scheme was evaluated on simulated EPI time series datasets A (with simulated motion in t_x, t_y, t_z and θ_z) and B (with simulated motion in θ_x, θ_y and θ_z). Both datasets have known ground truths for the applied slice-wise motion parameters which allow for precise evaluation of MSV registration performance. In addition, the non-distorted time series intensity images with applied motion is available to serve as image intensity ground truths to evaluate the performance of the field-corrected image reconstruction process. Tables 4.1 and 4.2 list the RMSE and MSV error standard deviation values of the estimated MSV motion parameters. With median filtering of the estimated MSV parameters, the errors decrease as κ increases and empirically converge to relatively small values. This implies that registration accuracy has improved with the concurrent correction method compared to a single-cycle correction method where a static field-map is used for geometric distortion correction prior to MSV (cycle 0). The observed empirical convergence strongly suggests that the algorithm is relatively stable as κ increases.

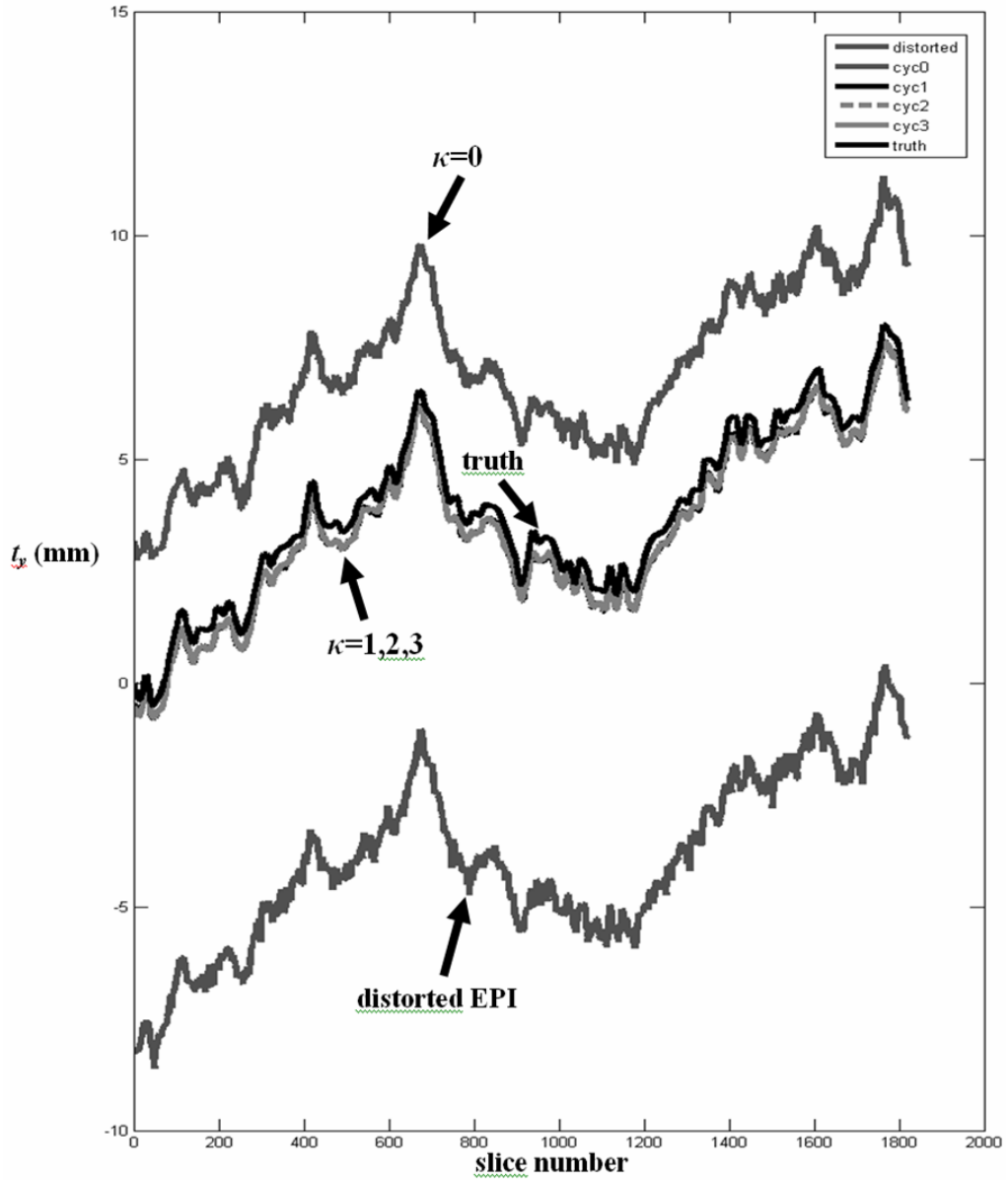

Figure 4.4: Median filtered MSV motion parameter t_y recovered at various correction cycles for dataset A. Field-inhomogeneity induced geometric distortion in the PE direction y cause significant MSV errors for the distorted EPI data as well as the corrected data in cycle 0 (κ=0). Correction cycles 1 to 3 yield estimates of t_y that are close to the ground truth as shown in Tables 4.1 and 4.2.

In fMRI, the accuracy of the reconstructed images' intensity values is of key importance since brain activation maps are computed from the change in image intensity values in the time-series. To measure image quality, the normalized root mean square error (NRMSE) values between corrected EPI slices and their corresponding T_2-weighted ground truth images are computed and averaged over the 120 volumes. Fig. 4.5 shows that the average NRMSE of each

slice in the 14-slice T_2-weighted volume decreases as κ increases. Empirical truth images were computed by correcting the simulated EPI time series images with the exact same dynamic field-map that was used to distort them. The empirical truth images contain errors inherent to the image reconstruction and MSV processes and represent the best images that can be obtained using these correction methods if the simulated dynamic field-map were known exactly. It is observed that when $\kappa \geq 2$, the corresponding NRMSE values converge to the NRMSE values of the empirical truth images which implies that the CFMMSV method yielded updated field-maps that are very close to the ground truth dynamic field-maps. Fig. 4.6 shows reconstructed EPI slices from the same position in the head and their corresponding absolute error images when compared to corresponding T_2-weighted ground truth images as κ increases. It is observed that the field-corrected image errors are greatly reduced when $\kappa \geq 3$.

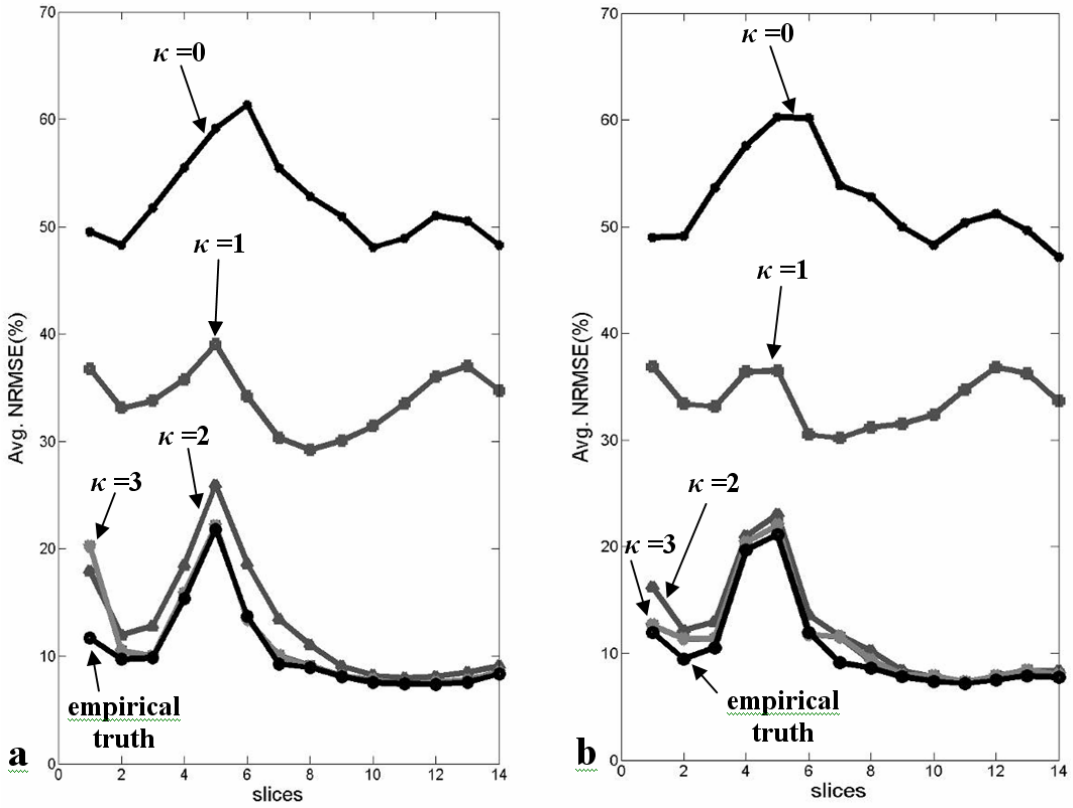

Figure 4.5: Normalized RMSE (NRMSE) values for each EPI slice in the same position in the head averaged over 120 volumes for various correction cycles for (**a**) dataset A with applied t_x, t_y, t_z and θ_z motion, and (**b**) dataset B with applied θ_x, θ_y, θ_z motion.

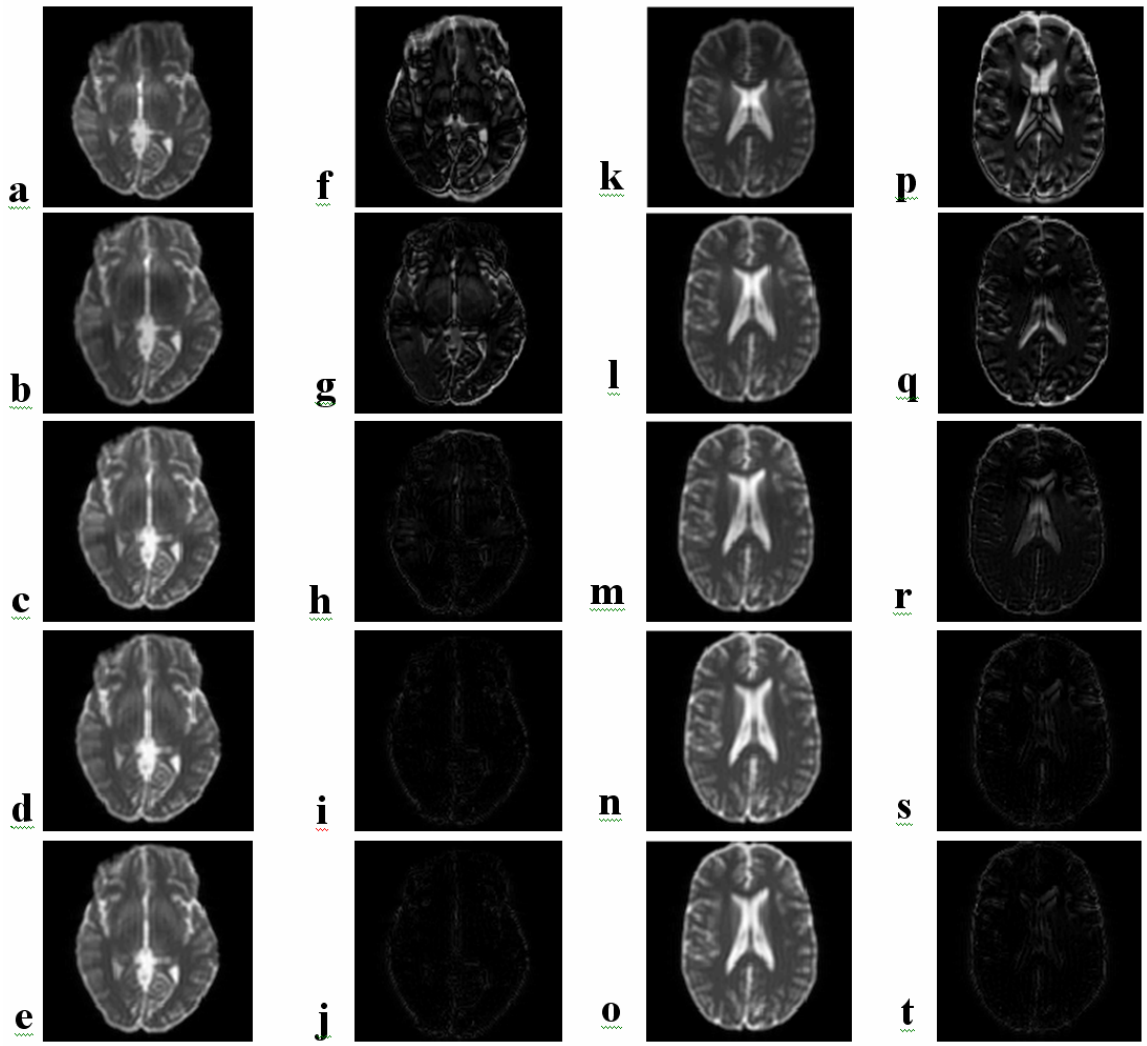

Figure 4.6: (**a-e, k-o**) Intensity and (**f-j, p-t**) absolute difference images with respect to ground truth images for two sample slices from dataset A at various stages in the CFMMSV correction process. (Top row) Geometrically distorted dataset, (second row) cycle 0, (third row) cycle 1, (fourth row) cycle 2, (fifth row) cycle 3. All images are displayed on the same normalized intensity scale ranging from 0 to 1.

As κ increases from zero, the field-corrected EPI images become more similar to the ground truth T_2 images. It is possible to obtain improved image NRMSE values without a corresponding improvement in activation detection performance since the simulated intensity increase is only 5% and applied to a relatively small subset of activated voxels. Thus, we applied the statistical random permutation test on datasets A and B at all stages of the CFMMSV correction process and computed ROC curves and respective AUC values to verify that activation detection performance improves as κ increases. Figs. 4.7(a-b) show the ROC curves for both datasets at several stages of the CFMMSV correction process and Table 4.3 shows the

corresponding AUC values. It is observed for both datasets that the AUC values increase significantly between cycle 0, which are the results one would obtain if the same static field-map was used to correct all the time series data, and cycle 3, which are the final results after applying the CFMMSV method. The improvement in activation detection is even more significant upon considering that fMRI studies are often performed directly on EPI datasets without any form of geometric distortion correction i.e. compare the AUC values between the distorted dataset and cycle 3. Fig. 4.8 shows the activation maps obtained ($\alpha = 0.001$) for two slices from datasets A and B at several stages in the CFMMSV correction process. Comparing the activation maps for cycle 0 (second row) and cycle 3 datasets (third row), it is readily observed that the latter has more true positives and fewer false positives. The ground truth activation regions for the two slices are shown in Figs. 4.8(e) and 4.8(j). Activation maps obtained by applying the random permutation test on the ground truth time series images for both datasets are also shown (fourth row) to illustrate the best performance obtainable with the statistical analysis method used.

All experiments were performed on Intel Pentium 4 Xeon 3.0GHz CPUs using MATLAB (The Mathworks Inc., Natick, MA, USA) and Advanced Visual Systems (Advanced Visual Systems Inc., Waltham, MA, USA).

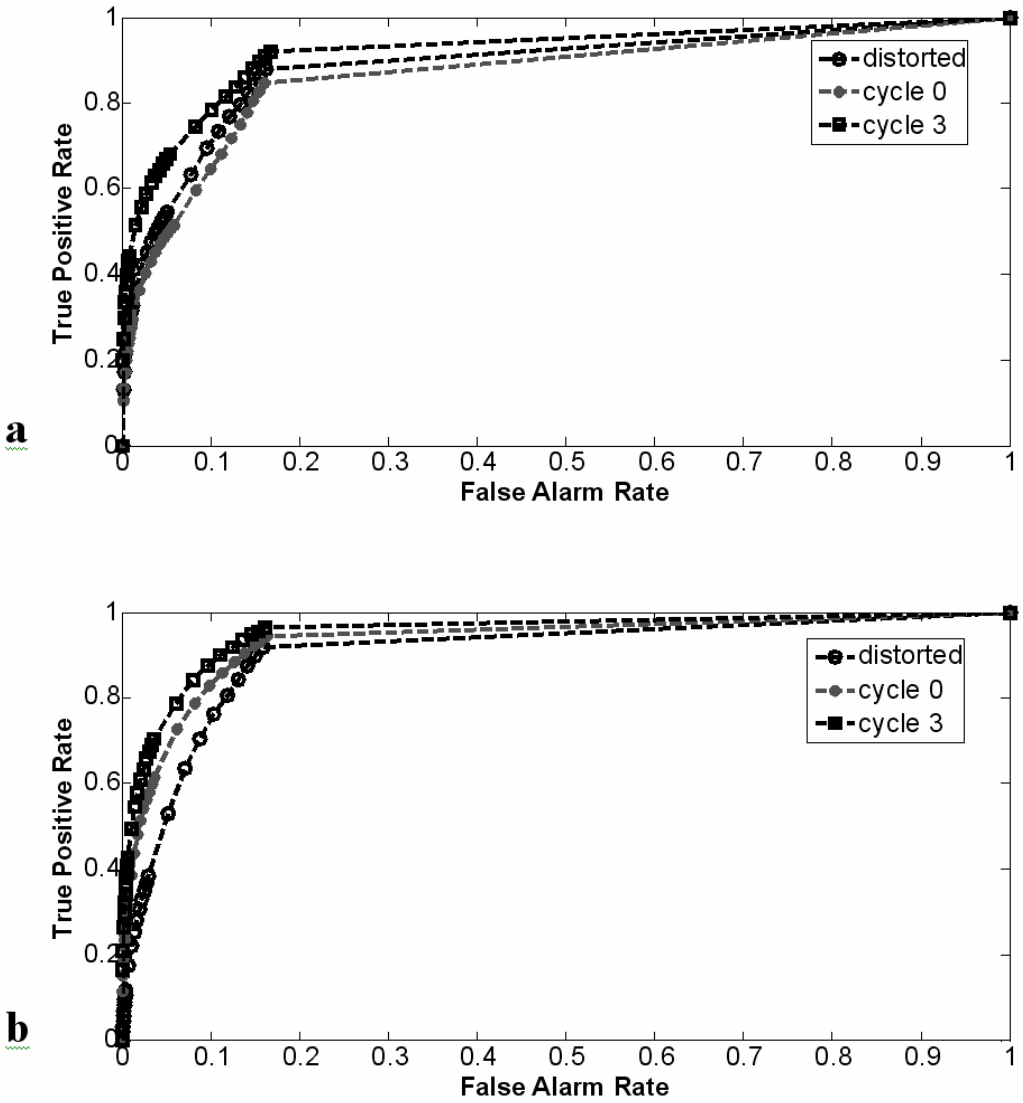

Figure 4.7: ROC curves showing activation detection performance for (**a**) dataset A and (**b**) dataset B at several stages in the CFMMSV correction process.

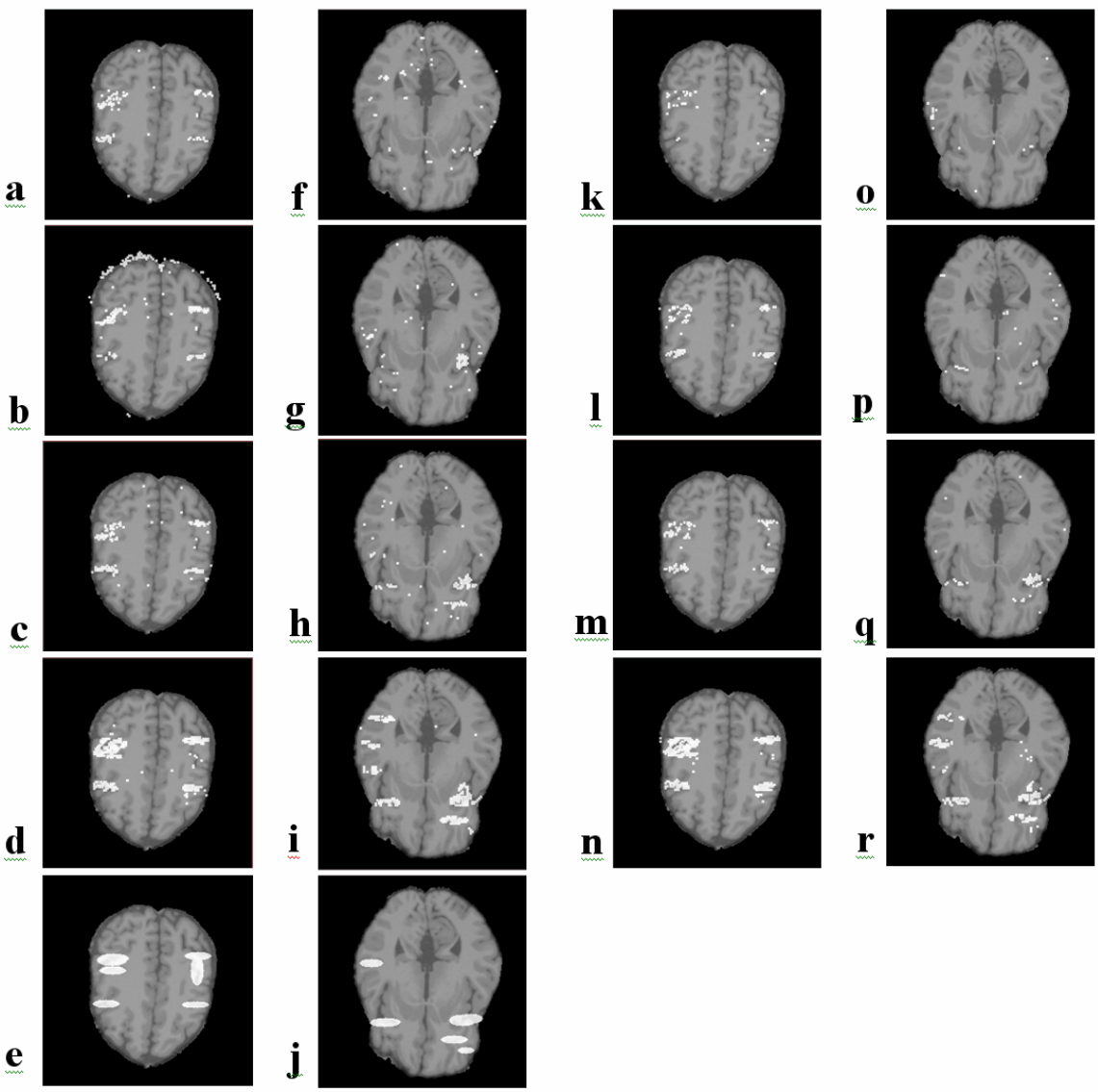

Figure 4.8: Activation detection maps (P=0.001) overlaid on anatomical data of two sample slices from (**a-d,f-i**) dataset A and (**k-r**) dataset B at several stages in the CFMMSV correction process. Each row of activation maps corresponds to a specific correction stage consisting of (top row) geometrically distorted, (second row) cycle 0, (third row) cycle 3 and (fourth row) ground truth time series images. The simulated activation maps applied to the two slices are shown in (**e**) and (**j**).

4.7 Discussion

The proposed CMFMSV framework is a retrospective correction framework that incorporates slice-to-volume registration, field-map updating and geometric distortion correction for the purpose of improving activation detection performance in fMRI. In this work, we have chosen to perform iterative field-corrected reconstruction to correct the geometric distortion and employ a

field-map updating scheme that applies rigid body MSV motion parameters to a high resolution static field-map of the object. Our results on two simulated EPI time series datasets show that as the number of correction cycles increases, the field-corrected image quality and the accuracy of recovered MSV motion parameters improve and empirically converge to the ground truths. This is evident in the decreasing MSV RMSE, MSV error standard deviation and image NRMSE values as κ increases (Tables 4.1 and 4.2 and Fig. 4.2). Improved activation detection performance, as inferred from the increasing AUC values in Table 4.3, is also observed as κ increases.

Table 4.1: RMS error of median filtered MSV estimates for simulated EPI datasets A and B.

Correction cycle	RMSE (mm and °)											
	Dataset A (motion applied t_x, t_y, t_z and θ_z)						**Dataset B** (motion applied θ_x, θ_y, θ_z)					
	t_x	t_y	t_z	θ_x	θ_y	θ_z	t_x	t_y	t_z	θ_x	θ_y	θ_z
Distorted	1.07	7.81	0.17	0.31	0.31	0.35	1.37	7.79	1.01	0.97	0.51	0.35
Cycle 0 (κ=0)	0.62	3.11	0.19	0.13	0.12	0.26	1.12	3.24	0.53	0.19	0.22	0.21
Cycle 1 (κ=1)	0.76	0.38	0.22	0.03	0.04	0.13	1.20	1.05	0.66	0.18	0.18	0.14
Cycle 2 (κ=2)	0.76	0.36	0.19	0.03	0.04	0.11	1.22	1.06	0.70	0.17	0.17	0.12
Cycle 3 (κ=3)	0.77	0.37	0.20	0.03	0.04	0.11	1.22	1.06	0.70	0.18	0.18	0.13

Table 4.2: Standard deviation of the error of median filtered MSV estimates for simulated EPI datasets A and B.

Correction cycle	Standard deviation of error of median filtered MSV (mm and °)											
	Dataset A (motion applied t_x, t_y, t_z and θ_z)						**Dataset B** (motion applied θ_x, θ_y, θ_z)					
	t_x	t_y	t_z	θ_x	θ_y	θ_z	t_x	t_y	t_z	θ_x	θ_y	θ_z
Distorted	0.95	0.16	0.16	0.30	0.18	0.35	1.34	0.98	0.98	0.89	0.37	0.35
Cycle 0 (κ=0)	0.50	0.15	0.14	0.10	0.10	0.21	1.10	0.92	0.48	0.19	0.21	0.14
Cycle 1 (κ=1)	0.62	0.07	0.15	0.03	0.04	0.11	1.16	0.96	0.63	0.18	0.18	0.14
Cycle 2 (κ=2)	0.62	0.07	0.14	0.03	0.04	0.10	1.18	0.98	0.66	0.17	0.17	0.12
Cycle 3 (κ=3)	0.62	0.06	0.14	0.03	0.04	0.10	1.18	0.98	0.66	0.18	0.18	0.12

Table 4.3: Area under ROC curve (AUC) values for activation detection of datasets A and B at various stages in CFMMSV correction.

Correction cycle	Area under ROC Curve (AUC)	
	Dataset A	**Dataset B**
Distorted	0.8880	0.9043
Cycle 0 (κ=0)	0.8664	0.9295
Cycle 1 (κ=1)	0.8990	0.9382
Cycle 2 (κ=2)	0.9053	0.9519
Cycle 3 (κ=3)	0.9208	0.9521
Ground truth T_2	0.9209	0.9659

These results demonstrate that, under the simulated conditions, the CFMMSV method can provide effective correction of motion artifacts that are complicated by the field effects induced by rigid head motion. It is interesting to note that for dataset A, the AUC value for cycle 0 actually decreased when compared to the AUC value for the distorted dataset. The AUC values increased subsequently in cycles 1 through 3. This illustrates that in the presence of significant motion, using a static field-map to correct an entire time series can lead to degraded activation detection performance, even after applying motion correction to the time series data. This is because the field-map changes due to motion were not accounted for.

Dataset A was simulated with relatively realistic assumptions of how the susceptibility-induced field-map changes with translations and in-plane rotation. Thus, the results obtained from that dataset are a reasonable indication of the performance of the concurrent correction method on well-shimmed real MR data with such motion. For real MR data, the field-map may include other contributions like post-shim system-induced field-inhomogeneity that remain stationary with respect to the head. Since the focus of the simulation study is on susceptibility-induced artifacts, we have assumed that these additional field-map contributions are less dominant and can be characterized separately, if necessary. This is a reasonable assumption for data collected from a well-shimmed magnet. Dataset B was simulated with similar assumptions as dataset A except that *local* field-map changes that may arise due to out-of-plane rotations are not modeled exactly. Thus, the results from dataset B are less indicative of the CFMMSV method's performance on real MR data in the presence of larger out-of-plane rotation. However, for small out-of-plane motion, the local field-map changes may be small enough [35] to justify the assumption that the dynamic field-map can be approximated with a rigid-body transformation of the static field-map.

For time series datasets that do not have ground truths, an appropriate stopping criterion is necessary to terminate the CFMMSV correction process automatically. In Table 4.1 and Fig.

4.2, respectively, the MSV RMSE and image NRMSE values remain relatively constant for $\kappa \geq 2$ for both datasets A and B which suggests that the procedure could be terminated earlier, thus reducing computation time. However, the increasing AUC values in Table 4.3 indicate that activation detection performance continues to improve for $\kappa \geq 2$. Thus, there is a computation time versus activation detection performance tradeoff that may influence the choice for the stopping criterion. To obtain minimal computation time at the expense of activation detection performance, the CFMMSV process can be tasked to automatically terminate when the time series' average NRMSE difference for the previous two cycles are below a threshold value. For maximal activation detection performance, the number of non-overlapping activated voxels for the previous two cycles can be used as a dissimilarity measure to automatically stop the CFMMSV process.

The CFMMSV framework was formulated to jointly correct for motion and geometric distortions arising from susceptibility-induced field-inhomogeneity without the explicit acquisition of dynamic field-maps. The framework can be further improved by using field-map update techniques that account for susceptibility-induced field-map changes with out-of-plane rotation. For example, a conceivable modification would be to apply MSV motion parameters to a high resolution 3D volume of a brain that has been pre-segmented into air, bone and soft tissue regions. The susceptibility-induced component of the dynamic field-map can then be re-estimated from the transformed 3D structural volume using numerical techniques to approximate solutions to the magnetostatic scalar potential based on Maxwell's equations [42,43]. This will increase the computational cost but may yield improved performance.

4.8 Conclusions

A proposed technique to perform concurrent susceptibility-induced geometric distortion correction with slice-to-volume motion correction for EPI fMRI data has been evaluated on two 120-volume simulated time series with different applied motion. Under the simulated conditions, the CFMMSV method improved the accuracy in recovering both the MSV motion parameters and the field-corrected reconstructed images compared to the simpler method of performing motion and geometric distortion correction independently. Activation detection performance, quantified using the AUC values at various stages in the CFMMSV correction process, also improved with the CFMMSV method. Although the CFMMSV method may currently be limited to small out-of-plane rotations, it presents a correction framework that addresses geometric distortion and slice-wise head motion as a joint problem and has the potential to perform better than methods that do not account for the relationship between these two problems.

CHAPTER 5

Motion-Induced Magnetic Susceptibility and Field Inhomogeneity Estimation using Regularized Image Restoration Techniques for fMRI

5.1 Introduction

In functional MRI (fMRI), times series images are acquired with high speed pulse sequences that are typically adversely affected by magnetic field-inhomogeneities. As a result, these images may be geometrically distorted or blurred depending on the pulse sequence used. A static field-inhomogeneity map may be measured before or after a fMRI session to correct for such distortions [4,35], but it does not account for magnetic field changes due to head motion *during* the times series acquisition. To address this, several prospective dynamic field mapping techniques have been proposed [9,10]. However, they require pulse sequence modifications or high computational cost. This work focuses on regularized image restoration methods to approximate dynamic field maps retrospectively without pulse sequence modifications.

In Chapter 4, the concurrent field map and MSV (CFMMSV) correction method [13] applies rigid body transformations directly to a static field map, which may be inaccurate in the presence of significant out-of-plane rotations. In the presence of such rotations, that method may not be suitable since field-inhomogeneities may change nonlinearly [43]. Our approach is to retrospectively estimate the object's magnetic susceptibility (χ) map from an observed susceptibility induced static field map using regularized image restoration principles. To compute the dynamic field maps, we apply rigid body motion to the χ-map estimate, and apply 3D susceptibility voxel convolution (SVC) [44] to the resultant spatially translated/ rotated χ-map. SVC is a deterministic, physics-based discrete convolution model for computing susceptibility induced field-inhomogeneity given a 3D χ-map. A simpler way to approximate the object's χ-map would be to segment a T1-weighted anatomical reference volume into air, bone and soft tissue, and apply literature susceptibility values to different voxels. However, this may introduce

segmentation errors and the use of incorrect susceptibility values, which may lead to inaccurate field map estimates. Our approach obviates the burden of ensuring good accuracy in both the segmentation process, and the susceptibility values used. We estimate the χ-map from a measured high resolution 3D static field map using 3D regularized image restoration techniques, i.e., solving the inverse problem of the noisy forward SVC model. The approach is demonstrated with realistically simulated noisy 3D field maps of a spherical air compartment in water.

5.2 Theory

5.2.1 Susceptibility Voxel Convolution for Field Map Computation

Previous work [42] has shown that given an object with K independent closed compartments of constant χ values, a Lorentz-corrected boundary element approach to computing the z-component of the χ-induced magnetic field map, $\mathbf{B}_p(\mathbf{r})$, yields

$$\mathbf{B}_p(\mathbf{r}) \approx \frac{\chi(\mathbf{r})}{3}\mathbf{B}_0 + \frac{\hat{\mathbf{z}}}{4\pi}\sum_{k=1}^{K}(\chi_k^+ - \chi_k^-)\oint_{S_k}\frac{z-z'}{|\mathbf{r}-\mathbf{r}'|^3}\mathbf{B}_0\cdot d\mathbf{S}' \text{ (Tesla)}, \tag{5.1}$$

where $\hat{\mathbf{z}}$ is a unit vector parallel to the scanner's main magnetic field $\mathbf{B}_0$, χ_k^+ and χ_k^- denote the susceptibilities outside and inside the k^{th} compartment, respectively, S_k is the k^{th} surface, $\mathbf{r}'$ is a surface point, $d\mathbf{S}'$ is perpendicular to the surface at $\mathbf{r}'$. In the presence of out-of-plane rotations, the orientation of the surfaces with $\mathbf{B}_0$, i.e., $\mathbf{B}_0\cdot d\mathbf{S}'$, changes, thus resulting in nonlinear field map changes.

Susceptibility voxel convolution (SVC) [44] applies Eq. (5.1) directly to voxels of an object. Each voxel is defined as a closed six-sided compartment of uniform susceptibility. The dot product, $\mathbf{B}_0\cdot d\mathbf{S}'$, is non-zero only for the top and bottom surfaces of a voxel. Only the upper surface is used since the superposition principle allows each surface to be used only once in computing $\mathbf{B}_p(\boldsymbol{x})$. The values of χ_k^- and χ_k^+ are obtained from the k^{th} voxel, and the voxel above it in the z direction, respectively. The χ-induced field equation now becomes

$$\mathbf{B}_p(\mathbf{r}) \approx \mathbf{B}_0\left[\frac{\chi(\mathbf{r})}{3} + \frac{1}{4\pi}\sum_{k=1}^{K}(\chi_k^+ - \chi_k^-)\int_{y_k-l_y/2}^{y_k+l_y/2}\int_{x_k-l_x/2}^{x_k+l_x/2}\frac{(z_k+l_z/2-z)}{|\mathbf{r}-\mathbf{r}'|^3}dx'dy'\right], \tag{5.2}$$

where (x_k, y_k, z_k) is the center of voxel k, and l_x, l_y, l_z are the x, y, and z lengths of a voxel. After discretisation in $\mathbf{r}$, Eq. (5.2) becomes a 3D discrete convolution in space domain. The convolution kernel can be written as

$$K(x-x_k, y-y_k, z-z_k) =$$
$$(z_k + l_z/2 - z) \int_{y_k - l_y/2}^{y_k + l_y/2} \int_{x_k - l_x/2}^{x_k + l_x/2} \left[(x'-x)^2 + (y'-y)^2 + (z_k + l_z/2 - z)^2 \right]^{-3/2} dx'dy', \tag{5.3}$$

and the SVC impulse response is

$$d(h,i,j) = \frac{\delta(l-l')\delta(m-m')\delta(n-n')}{3} + \frac{\left[K(h,i,j-1) - K(h,i,j)\right]}{4\pi}, \tag{5.4}$$

where (l,m,n) denotes the voxel where $\mathbf{B}_p$ is to be calculated, and (l',m',n') denotes voxels in the field of view. The discrete convolution of Eq. (5.2) becomes

$$\mathbf{B}_p(l,m,n) = \mathbf{B}_0 \sum_{l',m',n' \in \mathrm{FOV}} \chi(l',m',n') d(l-l', m-m', n-n'), \tag{5.5}$$

which can be computed with

$$\mathbf{B}_p = \mathbf{B}_0 \chi *** d = \mathbf{B}_0 \Im_{3D}^{-1}\left(\Im_{3D}(\chi)\Im_{3D}(d)\right), \tag{5.6}$$

where *** denotes 3D convolution and $\Im_{3D}$ denotes 3D Fourier transform. The discrete convolution can also be written in matrix-vector notation as

$$\mathbf{B}_p = \mathbf{D}\boldsymbol{\chi}, \tag{5.7}$$

where $\mathbf{D}$ denotes the SVC "system" matrix and $\boldsymbol{\chi}$ is the column-stacked χ-map vector. The χ-induced field map in Hz is $\Delta\omega_p = \gamma \mathbf{B}_p$, where γ is the gyromagnetic ratio of hydrogen.

The SVC impulse response is linear shift invariant and depends only on the voxel size and orientation with respect to $\mathbf{B}_0$. The impulse response remains unchanged when a 3D susceptibility map undergoes rigid body transformation.

5.2.2 Dynamic Field Map Estimation with Penalized Weighted Least Squares Estimation of Magnetic Susceptibility Map – A 3D Image Restoration Approach

A static field map, $\Delta\boldsymbol{\omega}_{\mathrm{static},}$ is typically approximated by taking the phase difference of a pair of gradient-echo images acquired at two different echo times [14], and may be composed of susceptibility and non-susceptibility induced field inhomogeneity sources. The two complex-valued images may be denoted by

$$I_j^{\mathrm{TE1}} = f_j + \varepsilon_j^{\mathrm{TE1}}, \tag{5.8}$$

$$I_j^{\mathrm{TE2}} = f_j e^{-i\Delta\omega_{\mathrm{static},j}\Delta TE} + \varepsilon_j^{\mathrm{TE2}}, \tag{5.9}$$

where f is the complex transverse magnetization of the object, j is the voxel number, ΔTE is the echo time difference, and ε is independent identically distributed MR Gaussian noise. The echo

time difference is typically small to prevent phase wrapping. In previous work [17], the maximum likelihood estimator for $\Delta\boldsymbol{\omega}_{\text{static}}$ was shown to be

$$\Delta\hat{\boldsymbol{\omega}}_{\text{static}} = \arg\min_{\Delta\boldsymbol{\omega}_{\text{static}}} \sum_j \left| I_j^{\text{TE2}} I_j^{\text{TE1}} \right| \left[1 - \cos(\angle I_j^{\text{TE2}} - \angle I_j^{\text{TE1}} - \Delta\omega_{\text{static},j}\Delta\text{TE}) \right]. \tag{5.10}$$

Ignoring phase wrapping, and decomposing $\Delta\omega_{\text{static},j}$ into susceptibility and system induced parts, i.e., $\Delta\omega_{\text{static},j} = \gamma[\mathbf{D}\boldsymbol{\chi}]_j + \Delta\omega_{\text{sys},j}$, and since a minimum exists when the cosine term equals one, the maximum likelihood estimator for $\boldsymbol{\chi}$ is

$$\hat{\chi}_j = \frac{1}{\gamma}\left[\mathbf{D}^{-1}\left[\frac{\angle\mathbf{I}^{\text{TE2}} - \angle\mathbf{I}^{\text{TE1}}}{\Delta\text{T}E} - \Delta\boldsymbol{\omega}_{\text{sys}} \right] \right]_j . \tag{5.11}$$

For simplicity, we assume that $\Delta\boldsymbol{\omega}_{\text{sys}}$ is negligible, or can be measured empirically. Since the SVC frequency response has very small values at some frequencies, the inverse SVC problem is ill-posed, and thus 3D smoothness regularization is desirable when solving for $\boldsymbol{\chi}$. We propose to use a quadratic penalized weighted least squares (QPWLS) image restoration approach to estimate $\boldsymbol{\chi}$ by minimizing the cost function

$$\Psi(\boldsymbol{\chi}) = \frac{1}{2}\left\| \mathbf{g} - \gamma\mathbf{D}\boldsymbol{\chi} \right\|_{\mathbf{W}}^2 + \beta\left\| \mathbf{C}\boldsymbol{\chi} \right\|^2, \tag{5.12}$$

where $\mathbf{g}$ is the observed static field map ($\angle\mathbf{I}^{\text{TE2}}$- $\angle\mathbf{I}^{\text{TE1}}$)/ΔTE, $\mathbf{W}$ is a weighting matrix that assigns higher weights to voxels where MR image intensity, i.e., $|I_j^{\text{TE2}} I_j^{\text{TE1}}|$, is higher, β is a regularization parameter that determines the amount of smoothing, and $\mathbf{C}$ is a first order finite-differencing matrix. We minimize the cost function using the conjugate gradient algorithm. Any available motion estimates for each slice/ volume in the fMRI time series can then be used to rotate/ translate the χ-map estimate. Since the SVC impulse response is linear shift invariant and depends only on the voxel size and orientation with respect to $\mathbf{B}_0$, it remains unchanged when a χ-map undergoes rigid body transformation. Thus, the same SVC matrix used in estimating the χ-map can be used to compute the dynamic field map after the desired motion has been applied.

The proposed QPWLS method was compared to three other methods of approximating the dynamic field map from an observed field map: thresholded inverse filtering, Wiener filtering [45], and direct rotation of the observed field map to the tilted positions [13]. The thresholded inverse filter ignores noise statistics and amplifies noise in frequency bands where the SVC frequency response has small values. To mitigate the latter, while preserving as much spatial information as possible, the threshold parameter needs to be chosen carefully, usually in an empirical manner. The Wiener filter assumes that χ and the additive field map noise are stationary

processes, and assumes that their power spectra may be estimated accurately, which is often not true in the χ estimation problem.

5.3 Methods

5.3.1 Data Simulation

To measure the algorithms' performances, we generated 91 pairs of ground truth χ-maps of a simulated, off-centered spherical air (χ_{air}=0.04 ppm [44]) pocket in water (χ_{water}=-9.05 ppm [44]) that was rotated counterclockwise about the *x*-axis by angles from 0° to 180° in increments of 2°. The dataset with 0° rotation was defined to be in the *non-tilted* position. In addition, an observed field map in the 0° position was generated. Each 256×256×256 dataset had a voxel size of 1mm×1mm×1mm.

A SVC impulse response was formed (Eq. (5.4)) and applied to all the ground truth χ-maps (Eq. (5.6)) with B_0=1.5 T. The resultant ground truth field maps were then cropped to 128×128×128 voxel volumes. To form the weighting matrix **W** in Eq. (5.12), we simulated an image intensity map, **f**, with zeros in the air pocket region (no MR signal), and 100 in the water region. Using the *non-tilted* ground truth field map ($\Delta\boldsymbol{\omega}_{static}$), an arbitrary value for ΔTE, and **f**, Eqs. (5.8) and (5.9) were used to generate two independent, complex Gaussian distributed images, each with an SNR of 100.0. An observed non-tilted field map, **g**, shown in Fig. 5.2(a), was then computed as described in the Theory section.

5.3.2 Experiments

The main goal of this work was to accurately estimate rotated χ-maps and field maps given an originally observed non-tilted susceptibility induced field map and the respective rotation angles about the *x*-axis. We compared the field map estimation accuracy of our proposed method with those of thresholded inverse filtering, Wiener filtering [45] and direct rotation of the original observed field map to tilted positions. A constant object power spectrum and the true power spectrum were used in the Wiener filter method to obtain two sets of Wiener filter results. Figs. 5.1 to 5.3 show results when a constant object power spectra was used, while Figs. 5.4 to 5.6 show results when the true object power spectra was used for the Wiener filter. The Wiener filter is the optimal stationary linear filter, in the MSE sense, for images degraded by additive noise and blurring. To use the Wiener filter in practice, we assumed an additive phase noise model, and chose a white Gaussian noise spectrum with a constant value that is identical to the variance of

the simulated noise. In reality, noise in a complex MRI image is additive Gaussian while phase noise is not.

The first part of the experiment involved the estimation of the original, *non-tilted* χ-map using the various methods. All estimates of χ were shown in Figs. 5.1 and 5.4. We applied the SVC matrix to these χ-map estimates to compute field map estimates from which a slice is shown in the top rows of Figs. 5.2 and 5.5. Root mean-square-error (RMSE) values were then computed with reference to the 3D ground truth non-tilted field map, $\Delta\boldsymbol{\omega}_{\text{static}}$. In the second part of the experiment, the χ-map estimates from the first part were all rotated about the x-axis by the same range of values used to create the 91 pairs of ground truth maps, i.e., 0° to 180° in increments of 2°. The SVC matrix was again applied to these rotated χ-map estimates to compute the dynamic field map estimates. Root mean-square-error (RMSE) values were then computed with reference to the 3D ground truth tilted field maps. The second rows in Figs. 5.2 and 5.5 show a field map slice of the object rotated by 45° about the x axis. The field map RMSE values for all positions and methods were plotted in Figs. 5.3 and 5.6.

The QPWLS implementation was built upon previous work [46], and 50 iterations of the algorithm were performed for each dataset with β=0.7. The initial guess for the conjugate gradient algorithm was a volume filled with zeros. For the thresholded inverse filter, a threshold value of 10 (0.2 % of the maximum absolute value of the inverse of the SVC frequency response) was used. All algorithms in this work were implemented in MATLAB (The Mathworks Inc., Natick, MA, USA) and C++, and were executed on Intel Pentium 4 Xeon 3.0GHz CPUs.

5.4 Results

The RMSE values over entire 3D field map estimates for all rotated positions using the various field map estimation methods are shown in Figs. 5.2 and 5.5. In Fig. 5.2, when the object power spectra for the Wiener filter was constant, it was observed that the QPWLS method had the lowest (best performing) RMSE values, and RMSE variability, across all rotated positions. In Fig. 5.5, when the true object power spectra was used for the Wiener filter, the RMSE values for the QPWLS method were comparable to the Wiener filter method. Compared to the QPWLS method, the Wiener filter's dependence on prior knowledge of the object's power spectra is a key disadvantage.

Fig. 5.1 shows slices in the y-z plane at the same spatial location of χ-map estimates of the object in the 45° rotated position, i.e., slices from a snapshot of Fig. 5.3. The x-axis points into the plane of the page. It was observed that the associated field map estimates in the spherical air region were invariably noisy for the inverse filter and Wiener filter (using a constant object power

spectra) in Figs. 5.2(b), 5.2(f), and Figs. 5.2(c), 5.2(g), respectively. The noise in this region was greatly reduced in the QPWLS estimates in Figs. 5.2(d) and 5.2(h) because the weighting matrix suppressed the data fidelity requirement in the air region, which allows for smoother χ-map estimates in this region. Since there were less abrupt susceptibility changes in the regularized χ-map estimates, the resultant field inhomogeneity estimate in the air region was small and smooth. For an EPI pulse sequence with a typical phase encode pixel bandwidth of about 20 Hz, the QPWLS RMSE values (<20 Hz) in Fig. 5.3 represent errors of less than one pixel shift. In contrast, the RMSE values for the other methods (>20 Hz) translate to errors of more than one pixel shift, which may reduce the accuracy of geometric distortion algorithms that depend on field maps. The SVC field map computation time was 1.5 secs for a 128×128×128 voxel χ-map. The computation times for χ-map estimation using the thresholded inverse filter, Wiener filter and QPWLS method were 4.1 secs, 5.8 secs, and 5.6 secs (per iteration), respectively.

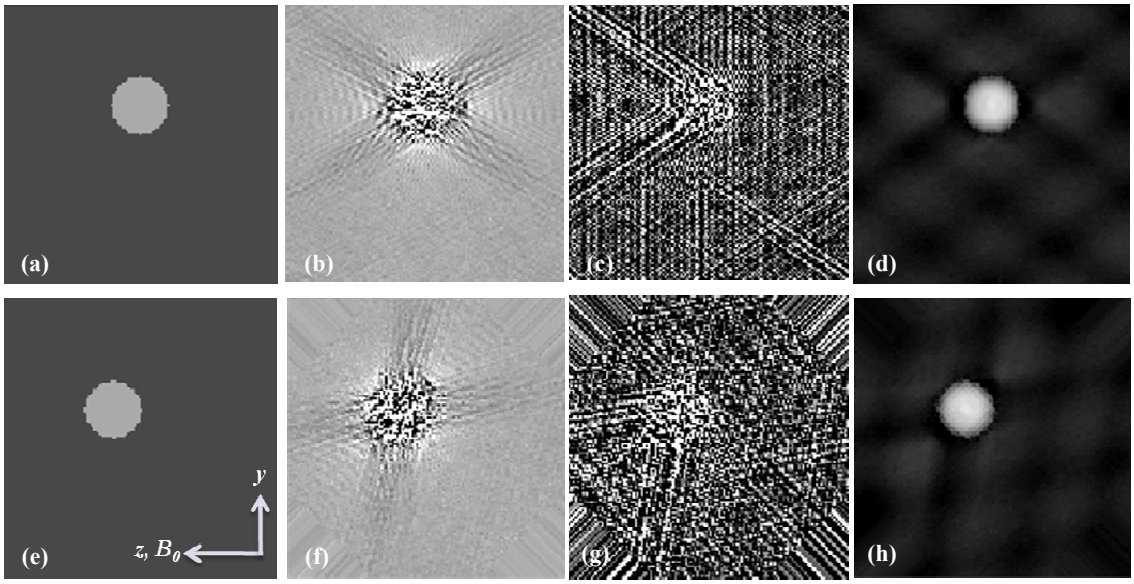

Figure 5.1: (Top row) Non-tilted χ map slice (y-z plane) from (**a**) true χ map, (**b**) thresholded inverse filter estimate, (**c**) Wiener filter estimate (using constant object power spectrum), (**d**) QPWLS estimate with β=0.7. (Second row) χ map slice rotated 45° using non-tilted (**e**) true χ map, (**f**) thresholded inverse filter estimate, (**g**) Wiener filter estimate (using constant object power spectrum), (**h**) QPWLS estimate with β=0.7. All images are displayed on the same intensity scale.

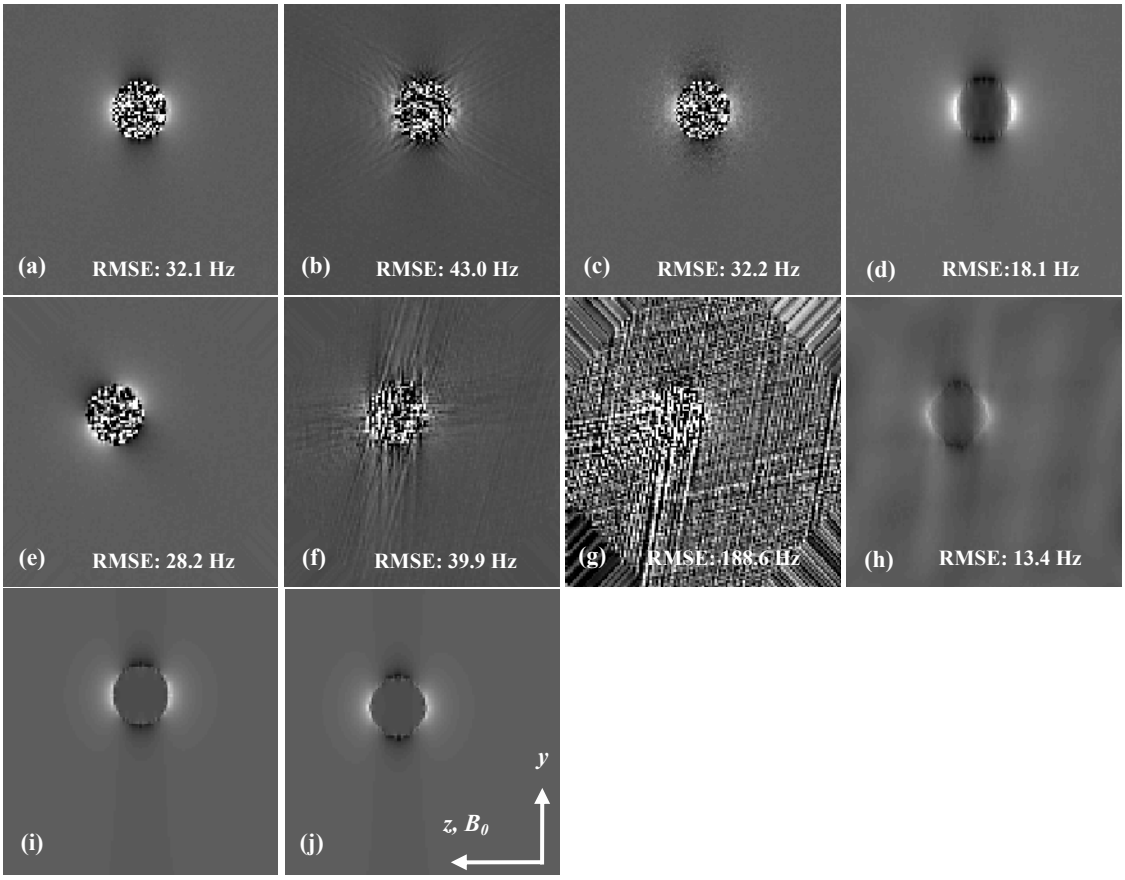

Figure 5.2: (Top row) Non-tilted field map slice (*y*-*z* plane) from (**a**) originally observed field map, (**b**) thresholded inverse filter estimate, (**c**) Wiener filter estimate (using constant object power spectrum), (**d**) QPWLS estimate with β=0.7. (Second row) 45° rotated field map slice from (**e**) rotation of original observed field map, (**f**) application of SVC on rotated estimate of χ from thresholded inverse filter, (**g**) application of SVC on rotated estimate of χ from Wiener filter (using constant object power spectrum), (**h**) application of SVC on rotated estimate of χ from QPWLS. (Bottom row) Ground truth field maps for (**i**) non-tilted, and (**j**) 45° tilted positions. All images are displayed on the same intensity scale.

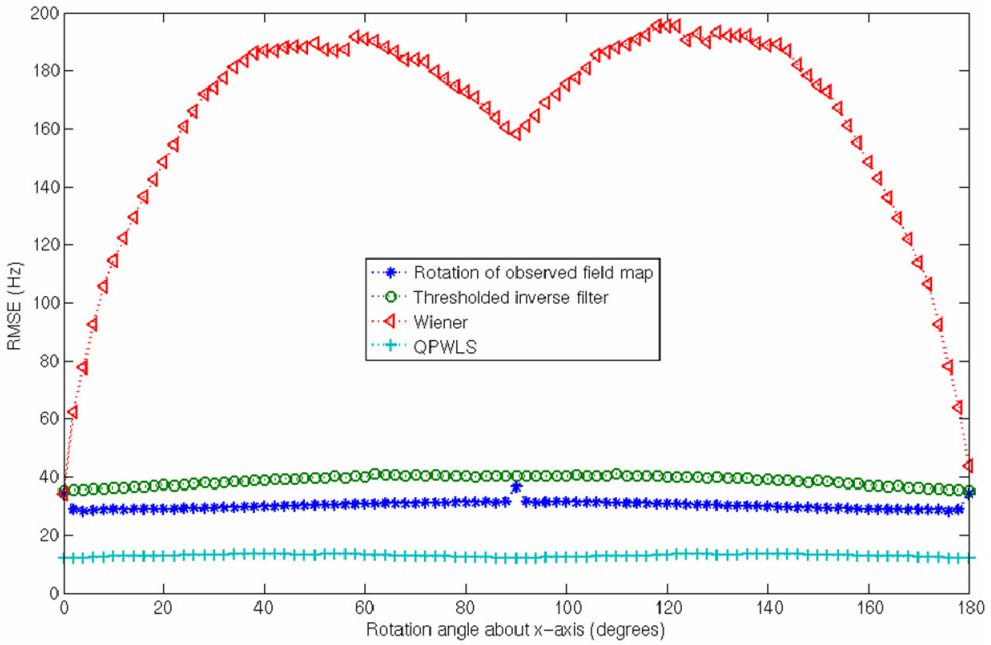

Figure 5.3: Dynamic field map RMSE values versus rotation angles for different estimation methods when object was rotated about the *x*-axis from 0° to 180°. An arbitrary constant object power spectrum was used in the Wiener filter.

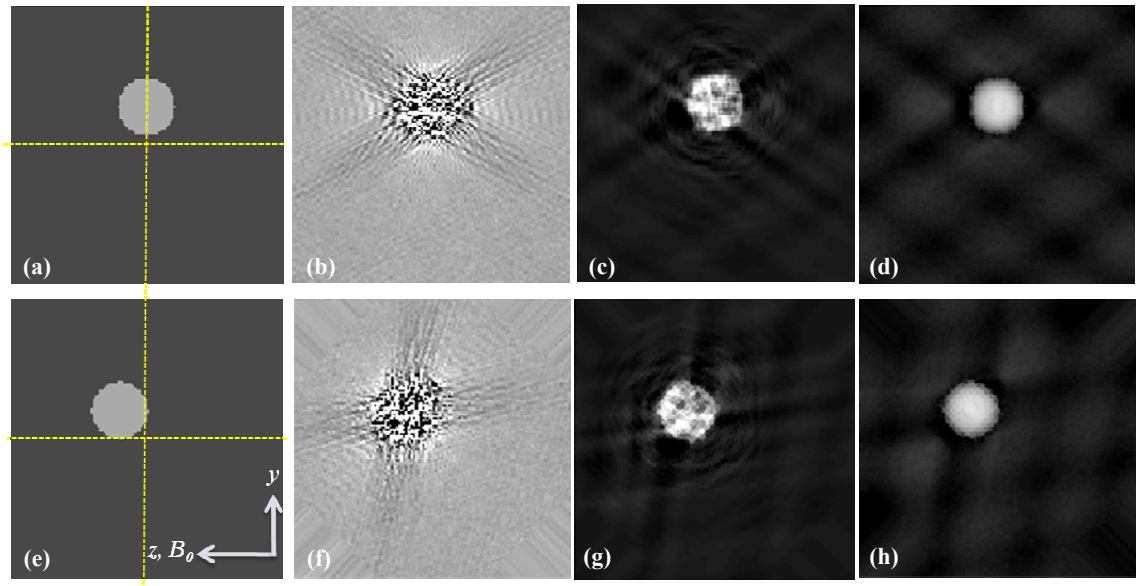

Figure 5.4: (Top row) Non-tilted χ map slice (y-z plane) from (**a**) true χ map, (**b**) thresholded inverse filter estimate, (**c**) Wiener filter estimate (using true object power spectrum), (**d**) QPWLS estimate with β=0.7. (Second row) χ map slice rotated 45° using non-tilted (**e**) true χ map, (**f**) thresholded inverse filter estimate, (**g**) Wiener filter estimate (using true object power spectrum), (**h**) QPWLS estimate with β=0.7. All images are displayed on the same intensity scale.

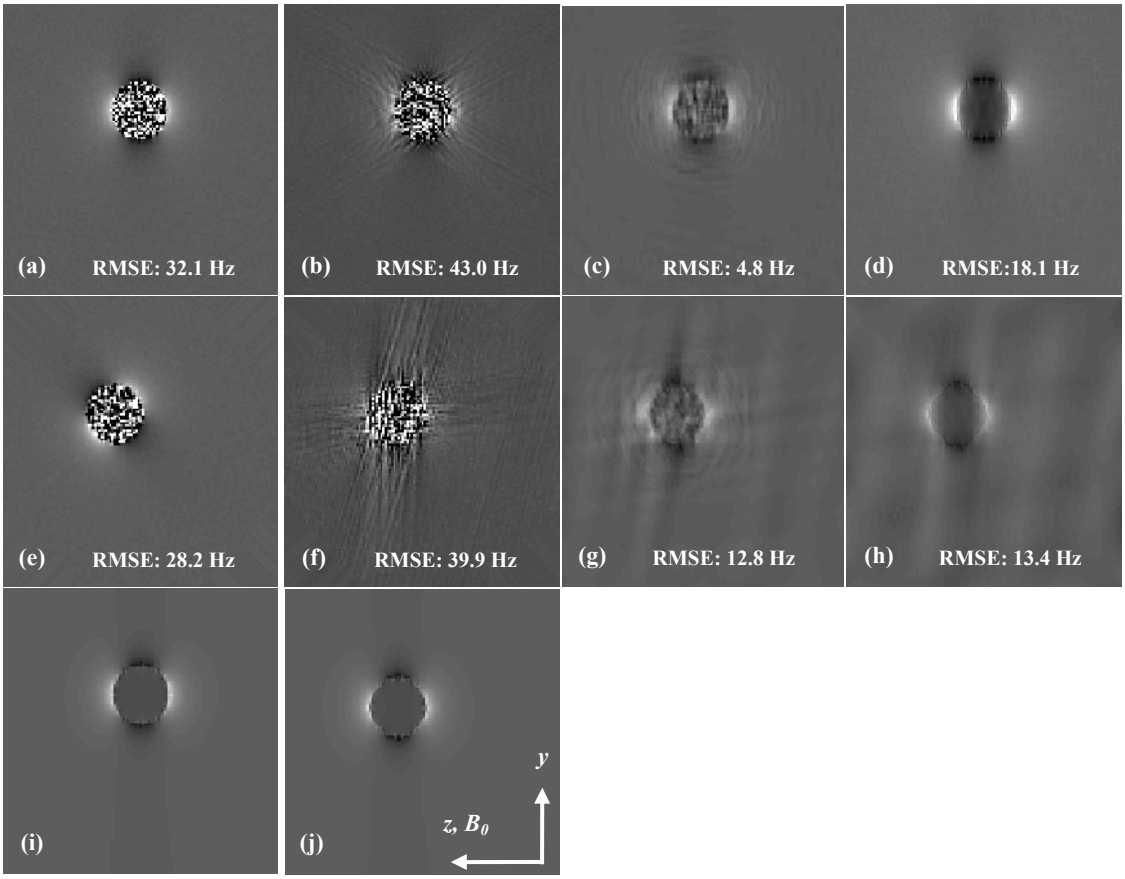

Figure 5.5: (Top row) Non-tilted field map slice (*y*-*z* plane) from (**a**) originally observed field map, (**b**) thresholded inverse filter estimate, (**c**) Wiener filter estimate (using true object power spectrum), (**d**) QPWLS estimate with β=0.7. (Second row) 45° rotated field map slice from (**e**) rotation of original observed field map, (**f**) application of SVC on rotated estimate of χ from thresholded inverse filter, (**g**) application of SVC on rotated estimate of χ from Wiener filter (using true object power spectrum), (**h**) application of SVC on rotated estimate of χ from QPWLS. (Bottom row) Ground truth field maps for (**i**) non-tilted, and (**j**) 45° tilted positions. All images are displayed on the same intensity scale.

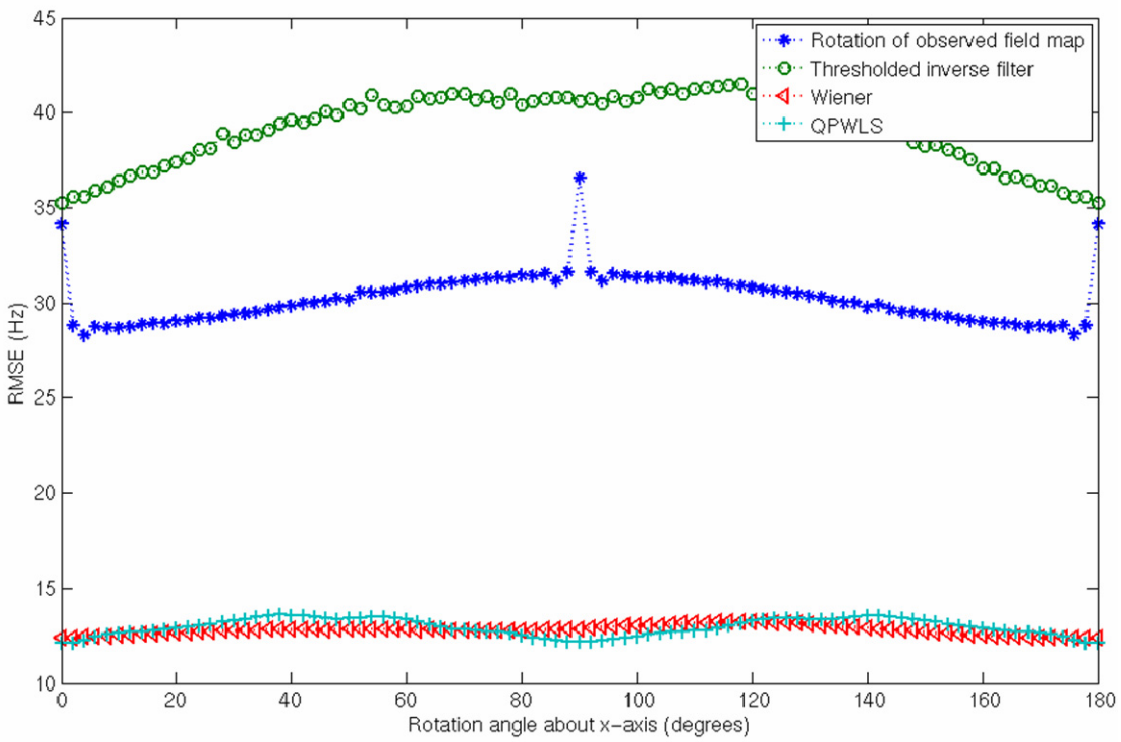

Figure 5.6: Dynamic field map RMSE values versus rotation angles for different estimation methods when object was rotated about the x-axis from 0° to 180°. The true object power spectrum was used in the Wiener filter.

5.5 Discussion and Conclusions

The proposed method estimates dynamic susceptibility induced field maps from an observed static susceptibility induced field map, while accounting for the proper MR noise model. It does not require segmentation or pulse sequence modifications, and may yield higher resolution dynamic field maps that address nonlinear changes due to out-of-plane rotations. Fig. 5.3 shows quantitatively that the QPWLS RMSE values were the lowest (best performing) among all the other methods. Figs. 5.2(d) and 5.2(h) show qualitatively that the field map estimates were close to the ground truths. For our spherical air pocket in water, nonlinear field map changes would typically be worst at the 90° position, hence a peak is observed at that position in Fig. 5.3 for the method that simply rotates the observed field map. In contrast, the low QPWLS RMSE variability across rotation angles in Fig. 5.3 suggests that the method performs reasonably well regardless of rotation angles. Further improvements in the proposed method may be possible upon optimizing the choice for the regularization parameter, coupled with the implementation of regularization functions that utilizes prior spatial information that is specific to a brain's χ-map. Since the χ-map of the brain is smooth, with the exception of air-tissue, bone-air and bone-tissue interfaces, an

edge preserving regularization function, e.g., Huber function, may be used instead. Coarse segmentation of a T1 weighted map of the brain into air, tissue and bone regions may still be helpful to identify voxels around susceptibility interfaces where edge preserving regularization can be selectively applied, while quadratic regularization is used for non-interface regions where the susceptibility map is expected to be smooth. This regularization scheme favors smoothly varying susceptibility map estimates within soft tissue, air and bone regions while allowing for abrupt susceptibility changes at the susceptibility interfaces. It is noted that segmentation is used here as an aid to choose the type of regularization for different brain regions and not for direct computation of the field map. A wrongly chosen regularization function will only lead to more, or less, blurring of the susceptibility map but should not change the locations of the susceptibility interfaces significantly.

The initial guess for the conjugate gradient algorithm was a volume filled with zeros. The use of the static field map as an initial guess for the algorithm may improve the rate of convergence since the static field map resembles the true field map more than a zero volume.

A potential limitation of the proposed method may arise because $\Delta\boldsymbol{\omega}_{sys}$ was ignored in Eq. (5.11) for simplicity. In our future work, we will investigate methods to reliably measure non-χ induced field inhomogeneities, and characterize their effects on the various approaches in this work.

A novel regularized image restoration approach to estimate field maps of a moving object was proposed and shown, with simulated data, to be more effective than non-regularized methods or simple transformations of an observed field map. In fMRI, this may potentially improve dynamic field map estimates and hence, geometric distortion correction accuracy.

CHAPTER 6

Formulation of Current Density Weighted Indices for Correspondence between fMRI and Electrocortical Stimulation Maps

6.1 Introduction

Epilepsy surgery to remove identifiable epileptogenic regions of the brain is often achieved in conjunction with an electrocortical stimulation (ECS) [47] map obtained either before or during the resection surgery. The goal of this mapping is to identify brain regions that are essential for language and sensorimotor functions prior to frontal or temporal lobe resection. Defining hemispheric language and sensorimotor localization in patients with intractable epilepsy is important for avoiding complications of epilepsy surgery involving eloquent cortex. Currently, intraoperative or extraoperative electrocortical stimulation mapping of sensory, motor, and language are used to define the safe limits of resection. The intraoperative ECS procedure performed during an awake craniotomy, followed by resection, subjects the patient to additional strain during surgery. In extraoperative ECS, the placement of subdural electrode arrays for functional mapping places the patient at risk for complications.

Functional magnetic resonance imaging (fMRI) techniques show strong potential for presurgical evaluation of patients with brain tumors or epileptic lesions and may provide a non-invasive alternative to the ECS method to define eloquent cortex at risk during epilepsy surgery. In constant current bipolar ECS, each pair of adjacent electrodes on an electrode grid is stimulated with alternating polarity square wave current pulses. The stimulus current intensity is increased gradually until either the patient's response changes, or an afterdischarge, is observed. In fMRI, an increase in cerebral blood flow induced by local neuronal activity modulates the proportion of oxyhemoglobin to deoxyhemoglobin in nearby vasculature. This results in a magnetic susceptibility difference between the blood vessel and surrounding tissue which can be imaged with a T_2^*-weighted MRI protocol. Because fMRI's stimulation mechanism differs from ECS as the standard technique for presurgical functional mapping, the accuracy of fMRI

functional mapping must be validated for spatial consistency with ECS maps. In this work, stimulated electrode pairs are classified into two categories: ON pairs yielded response changes while OFF pairs did not.

For ECS-fMRI validation, a correspondence index that incorporates contextual information provided by a given set of ON/ OFF stimulated electrode pairs would be useful when comparing mapping data. A reliable performance index would be statistical in nature and yet based on a phenomenon that is physically related to the likely regions of neuronal stimulation around the electrodes. To date, it is not known exactly how different neural tissues respond to ECS and at what current threshold levels functional deficits may occur. However, it is known that for electrical stimulation of nerve fibers, an increase in the injected current intensity level increases the number of axons that are depolarized [48]. Also, the effectiveness of stimulating a nerve fiber decreases with increasing distance from the stimulating electrode [48]. An increase in injected current intensity increases both the electric field magnitude and current density distributions in the tissue for any given anatomical geometry and electrode impedance. These electrostatic quantities decrease in magnitude with increasing distance from the stimulating electrodes and can be numerically approximated by modeling the brain as a chargeless volume conductor and solving the Laplace equation with appropriate Dirichlet and Neumann boundary conditions [49]. As such, we propose incorporating information from the current density map in the brain during electrical stimulation to define ECS-fMRI correspondence indices.

Previous studies in clinical ECS-fMRI correspondence have utilized 3D Euclidean distance based measures [50-53] and statistical indices [54] to quantify how close the fMRI activation maps were to ECS functional maps. For the former, the minimum, maximum and mean Euclidean distances from ON/ OFF electrodes to the local maxima and edge of the nearest fMRI cluster [50,53] have been used. The distance from the tested electrodes to the centroid of the nearest fMRI cluster has also been used as a performance index [52]. These measures are easy to evaluate and provide an intuitive feel of how close the tested electrodes are to surrounding fMRI activation clusters. However, these measures do not utilize much of the clusters' spatial information, i.e., shape, spread, number of voxels etc. This may yield overly optimistic correspondence values for an activation cluster that may be small and artifactual in nature, but is close to a tested electrode. The reliability of these Euclidean distance measures may also be dependent on the accuracy of the clustering algorithms used, either in the process of, or after fMRI statistical analysis.

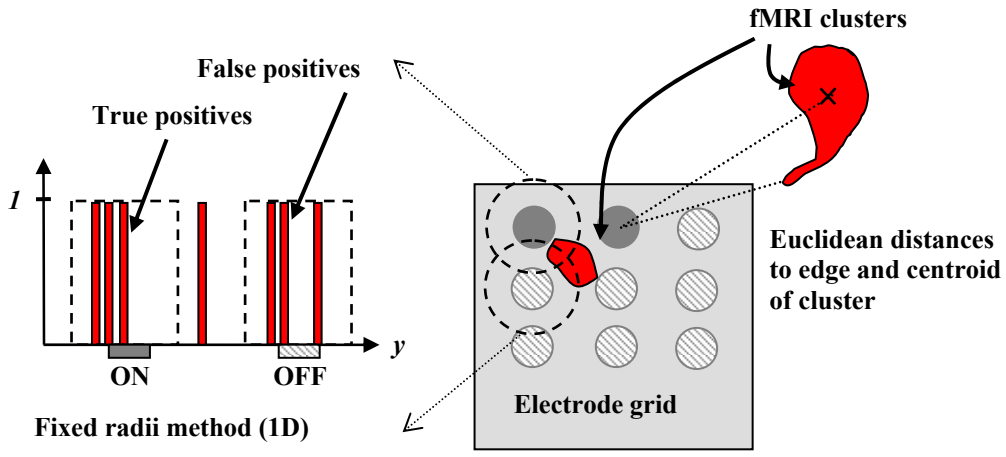

Figure 6.1: In the voxel-based fixed radii method (left), fMRI activation voxels (represented by vertical bars with values of 1) within a user-specified radius around ON (solid shaded discs/ circles) and OFF (diagonal shaded discs/ circles) electrodes are true positives and false positives respectively. In the Euclidean distance method (right), the mean Euclidean distances from ON electrodes to the edges and centroids of all fMRI activation clusters are computed.

Statistical indices like sensitivity, specificity, positive predictive value (*PPV*), negative predictive value (*NPV*) and geometric mean (*gmean*) are widely used classification performance indices. Unlike Euclidean based measures, these indices have a fixed range from 0 to 1.0. To compute these indices for an fMRI activation map, the number of fMRI voxels that are true positives (*TP*), false positives (*FP*), true negatives (*TN*) and false negatives (*FN*) must first be calculated. To do that, some assumptions regarding the voxel-wise locations and "likelihood" of ground truth functional activation given an ECS functional map are required. The ground truth activation voxels can be contained within a user-defined radius around each ON task tag [54] such that any fMRI activated voxels found within the radius causes the tag to be counted as a true positive tag. The sensitivity was defined as the percentage of language tags that exhibited ECS-fMRI matches and the specificity as the percentage of non-language tags that did not exhibit ECS-fMRI matches. Non-language tags were defined as stimulation sites which yielded non-language related responses. No clustering of fMRI activation data is required or assumed. It is, however, not clear how large the radii around the tags should be under different stimulation current levels. Also, a lone fMRI activated voxel found within the specified radius of a language tag would yield the same ECS- fMRI match as a large and dense activation cluster within the same radius. Since there are typically only small numbers of task and non-task tags, the tag-wise sensitivity and specificity values can be significantly altered by stimulus-correlated motion or

noise-induced fMRI activation voxels that happen to fall within the specified radii of the task or non-task tags. Thus, it may be more desirable to consider the actual number of voxels that fall within the radii of the tags as well.

In the above fixed radii method, all activated voxels within the radii are given the same level of influence in determining the indices, irrespective of their relative distances from the electrodes. Activated voxels located outside these radii are not counted. These fixed windows of ground truth voxels make it difficult to measure incremental improvements in ECS-fMRI correspondence when fMRI activated voxels consistently fall outside the windows but are nevertheless inching towards the ON electrodes, e.g., as a result of improved data processing techniques. The true positive count will still be zero. A Euclidean distance measure would be useful in these cases but the previously mentioned limitations would then arise.

There are indications that the level of elicited neuronal activation is influenced by applied stimulus levels [48]. Since a higher stimulus current intensity would likely exceed a wider range of neuronal activation threshold levels, an ECS-fMRI correspondence index may be physically more meaningful and reliable if information from the electric field or current density map was incorporated into its definition. We propose a current density weighted method that combines the advantages of distance-based measures with voxel-wise statistical indices to quantify ECS-fMRI correspondence. We do not calculate Euclidean distances between reference points explicitly and do not assume that the fMRI maps consist of clusters. Information of the Euclidean distance between each activated voxel with respect to ON or OFF electrodes is embedded in numerically computed current density maps by solving the Laplace equation for a quasistatic volume conductor using the finite difference method. Each current density map is unique to each patient-task combination and depends solely on the ECS functional map and current or voltage stimulation parameters.

The goals of this study are to (i) examine and evaluate the ECS-fMRI correspondence indices in various simulated test cases, and, (ii) to demonstrate the use of these indices in human data. We formulate a current density weighted scheme to assess the relative numbers of fMRI true positives, true negatives, false positives and false negatives [58], i.e., populate a contingency table or confusion matrix. These values are then used to compute five existing statistical measures for classification performance, i.e., sensitivity, specificity, positive predictive value (*PPV*), negative predictive value (*NPV*) and geometric mean (*gmean*) [55]. A 3D volume with a simulated electrode grid and simulated fMRI activation maps are used to investigate and compare the behaviors of the proposed current density weighted measures and modified versions of two previously reported correspondence indices [50,54]. The current density weighted indices are also

computed for three different patients who participated in fMRI studies for verbalized language tasks followed by language mapping with extraoperative ECS procedures prior to surgical treatment. The patient studies demonstrate the feasibility of current density weighted statistical measures for evaluating fMRI activation localization with extraoperative ECS mapping.

6.2 Methods

All computational work was performed on Intel Pentium 4 Xeon 3.0 GHz CPUs using MATLAB (The Mathworks Inc., Natick, MA, USA) and Advanced Visual Systems (Advanced Visual Systems Inc., Waltham, MA, USA). The patient studies were conducted in accordance with the guidelines set by the University of Michigan Medical School Institutional Review Board. Informed consent was obtained from all three subjects.

The post-grid CT datasets were acquired on GE MDCT LightSpeed machines, LS16, LS16pro, LSultra(8) and LS4slice scanners. The acquisition protocol was axial slices through electrodes, posterior fossa through vertex and slice thickness of 1.25 mm in a tilted mode so as not to include the lenses with a field of view of 23 cm. All MRI data were acquired on a 1.5 T GE SIGNA MR scanner (GE Medical Systems, Milwaukee, WI). All anatomical MR datasets were acquired with a 3D Spoiled GRASS (SPGR) protocol with the following parameters: TR=10 ms, TE=3.7 ms, flip angle=8 degrees, FOV=25 cm, voxel size=1.0 mm×1.0 mm×1.5 mm, image matrix = 256×256×120. Functional MRI datasets were acquired prior to the grid electrode implant. An echo-planar imaging (EPI) sequence with slice interleaving was used with the following parameters: TR=3000 ms, TE=30 ms, flip angle=90 degrees, FOV=24 cm, voxel size=1.95 mm×1.95 mm×6.0 mm, image matrix = 128×128×16.

6.2.1 Activation Localization in fMRI

Each set of fMRI time series for a test paradigm consists of six cycles of 30 s of stimuli presentation followed by 30 s of rest. Language paradigms in fMRI sessions were designed to follow the equivalent tests in ECS language mapping, which include confrontation naming, responsive naming, and tongue rapid alternating lateral movement (tongue RAMs). For the visual confrontation naming (picture naming of line drawings of objects) task during fMRI, each patient was instructed to name aloud the objects projected on a screen. For responsive naming, the patient would respond verbally to a series of questions asked through intercom during the activation periods. The tongue RAMs task was a self-paced tongue movement from one corner of the lips to the other for 30 s followed by 30 s rest for six cycles.

6.2.2 Euclidean Distance and Voxel-Based Fixed Radii ECS-fMRI Correspondence Indices

To facilitate a fairer comparison of the afore-mentioned tag-wise fixed radii method with our voxel-based current density weighted correspondence indices, and to improve the former's robustness to errors in the presence of lone fMRI activated voxels, we reconfigured the tag-wise fixed radii method by defining voxels within the radii of ON electrodes (task tags) as ground truth positives and OFF electrodes (non-task tags) as ground truth negatives. The values of *TP* and *FP* are computed by counting the total number of fMRI activation voxels within the fixed radii around the ON electrodes and OFF electrodes, respectively. The values of *FN* and *TN* are the total number of fMRI non-activation voxels within the fixed radii around the ON electrodes and OFF electrodes, respectively. The sensitivity, specificity, *PPV*, *NPV* and *gmean* indices are then computed using the voxel-based quantities *TP*, *FP*, *FN* and *TN*. The sensitivity is now the percentage of voxels (of all voxels within the radii of task tags) that have corresponding fMRI activation, i.e., true positive accuracy. The specificity is now the percentage of voxels (of all voxels within the radii of non-task tags) that do not have corresponding fMRI activation, i.e., true negative accuracy. The choice of the radius around the tags is still arbitrary. This voxel-based method of computing statistical performance indices will be referred to as the "voxel-based fixed radii" method (Fig. 6.1).

6.2.3 Current Density Weighted ECS-fMRI Correspondence Indices

For a current density weighted method for computing the ECS-fMRI correspondence indices, let an fMRI activation map, which is a 3D binary map of activated ('1') and non-activated ('0') voxels, be denoted by $m(\boldsymbol{r})$ where $\boldsymbol{r}$ is the vector of 3D spatial variables (x, y, z). It is assumed that $m(\boldsymbol{r})$ is spatially registered to a 3D T1-weighted anatomical reference volume $g_{ref}(\boldsymbol{r})$. Let $J_{\mathrm{ON},k}(\boldsymbol{r})$ denote the *magnitude* of the 3D current density vector field when the k^{th} pair (out of K pairs) of ON electrodes is stimulated. To obtain good ECS-fMRI correspondence, it is expected that fMRI activation would occur near ON electrode pairs and not in the proximity of OFF electrode pairs. The weighted number of true positives is computed by multiplying each fMRI activated voxel, which has a value of 1, with the current density magnitude at that voxel for each ON electrode pair, and then summing all these weighted voxels as follows:

$$TP = \sum_{k=1}^{K} \sum_{\boldsymbol{r}_i \in FOV} m(\boldsymbol{r}_i) J_{ON,k}(\boldsymbol{r}_i) , \tag{6.1}$$

where $\boldsymbol{r}_i$ is the spatial vector variable (x_i, y_i, z_i) for the i^{th} voxel and FOV denotes the imaging field of view. In other words, *TP* is the sum of all fMRI activated voxels weighted by corresponding current density map voxels for all ON electrode pairs. An activated voxel that is far away from any ON electrode pair is effectively ignored since the corresponding current density value will be negligible. In a similar manner, *FP* is computed by using $J_{\mathrm{OFF},l}(\boldsymbol{r})$, the current density map when the l^{th} pair (out of *L* pairs) of OFF electrodes was stimulated

$$FP = \sum_{l=1}^{L} \sum_{\boldsymbol{r}_i \in FOV} m(\boldsymbol{r}_i) J_{OFF,l}(\boldsymbol{r}_i) . \tag{6.2}$$

The number of true negative and false negatives are computed as

$$TN = \sum_{l=1}^{L} \sum_{\boldsymbol{r}_i \in FOV} (1 - m(\boldsymbol{r}_i)) J_{OFF,l}(\boldsymbol{r}_i) \text{ and} \tag{6.3}$$

$$FN = \sum_{k=1}^{K} \sum_{\boldsymbol{r}_i \in FOV} (1 - m(\boldsymbol{r}_i)) J_{ON,k}(\boldsymbol{r}_i) \tag{6.4}$$

where $1\text{-}m(\boldsymbol{r}_i)$ is equal to 1 for non-activated voxels and 0 for activated voxels. Fig. 6.2 illustrates the above equations in one dimension.

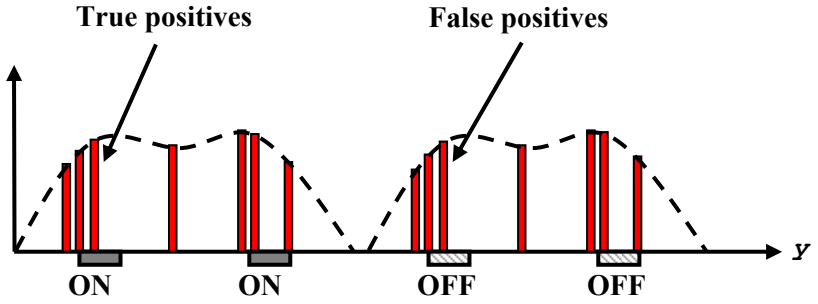

Figure 6.2: In the current density weighted method, fMRI activation voxels (vertical bars) weighted by the ON (solid shaded discs) and OFF electrodes' (diagonally shaded discs) current density values (dotted line) at the voxels' locations contribute to the true positive (*TP*) and false positive (*FP*) quantities respectively. The fMRI non-activated voxels weighted by the ON and OFF current density values contribute to the false negative (*FN*) and true negative (*TN*) quantities respectively.

With the above quantities, the following ECS-fMRI correspondence indices, all of which are in the range of 0 to 1.0, can be evaluated:

$$accuracy = \frac{TP + TN}{TP + TN + FP + FN}, \tag{6.5}$$

$$sensitivity = \frac{TP}{TP + FN} , \tag{6.6}$$

$$specificity = \frac{TN}{TN + FP}, \tag{6.7}$$

$$positive\ predictive\ value\ (PPV) = \frac{TP}{TP + FP}, \tag{6.8}$$

$$negative\ predictive\ value\ (NPV) = \frac{TN}{TN + FN}, \tag{6.9}$$

$$geometric\ mean\ (gmean) = \sqrt{sensitivity \cdot specificity}\ . \tag{6.10}$$

The sensitivity and specificity indices can be used to measure the accuracies of detecting true positives and true negatives, respectively, for a given classification test, i.e., a given fMRI map. However, it is also desirable to have a single index to represent both types of accuracies. The accuracy and geometric mean (*gmean*) indices are possible candidates for such an index. It has been reported [55] that the accuracy index, which measures the proportion of voxels in the brain that were classified correctly (positives and negatives), can be misleading when there is a class imbalance situation, e.g., when the total number of possible negative cases (*TN*+*FP*) is much larger than the total possible positive cases (*TP*+*FN*). In ECS, this scenario may arise when there are many more OFF electrode pairs than ON electrode pairs, or when OFF electrodes are stimulated at much higher current levels than ON electrodes. A significant increase in true positives may yield a negligible increase in accuracy if the number of true negatives is large enough to dominate the ratio in Eqn. 5, making it difficult to compare relative fMRI activation detection performance for the same subject. Also, even when no fMRI activation is detected (*TP*=0), the accuracy can still be very high if *TN* is almost as large as the denominator (*TN*+*FP*+*FN*), i.e., more true negatives than false positives near OFF electrodes and false negatives near ON electrodes. Thus, the accuracy index is not used to quantify ECS-fMRI correspondence in subsequent sections. The *gmean* index was proposed [55] as an alternative single-valued index that quantifies true positive and true negative accuracies simultaneously without incurring the class imbalance problem.

The sensitivity, specificity and *gmean* are the main indices of interest while the positive predictive and negative predictive values are computed for completeness and may serve as useful reference for future work.

6.2.4 Dynamic Ranges of Current Density Weighted Correspondence Indices

A physical interpretation of the upper and lower limits of the current density weighted sensitivity, specificity and *gmean* indices is useful to understand the scenarios that yield the worst and best case values. Assuming there is at least one pair of ON and one pair of OFF electrodes, the sensitivity will be 1.0 if every fMRI voxel in the field-of-view is activated (hence, specificity will be 0), and 0 if no fMRI activation is observed (hence, specificity will be 1.0). These extreme cases are easily detected. For practical fMRI maps with at least some fMRI activation voxels near the electrodes, a sensitivity value close to 1.0 indicates that fMRI activation occurred in regions where the combined current density distribution function of ON electrodes has the most energy (close to ON electrodes). A sensitivity value close to 0 indicates that either only a few fMRI activation voxels are present, or that fMRI activation occurred predominantly in low energy regions of the ON electrodes' current density function (far from ON electrodes). Likewise, a specificity value close to 1.0 indicates that fMRI non-activation voxels occurred in regions where the combined current density distribution function of OFF electrodes has the most energy (close to OFF electrodes) while a specificity value close to 0 indicates either the presence of only a few fMRI non-activation voxels, or that fMRI non-activation voxels occurred predominantly in low energy regions (far away from OFF electrodes) of the OFF electrodes' current density function. Since *gmean* depends on the product of sensitivity and specificity, a *gmean* value close to 1.0 indicates that the sensitivity and specificity values are *both* close to 1.0. A *gmean* value close to 0 indicates that either the sensitivity or specificity, or both indices, are close to zero.

Due to the possible overlapping of ON and OFF electrode current density distributions, the sensitivity and specificity values, and hence the associated *gmean* value, rarely attain their maximum values of 1.0 simultaneously. The maximum possible *gmean* depends on the how much the ON and OFF electrode current density distributions overlap and may vary from patient to patient. As such, it may be useful to approximate the maximum possible *gmean* value for each patient before computing the empirical *gmean* values. ECS-fMRI correspondence can then be evaluated using

$$gmean\,(\%) = 100 * (gmean / max\_gmean)\,. \tag{6.11}$$

Eq. (6.11) is especially relevant for clinical data because it provides a reference point to evaluate computed *gmean* values with respect to the best "score" that can be achieved for a specific ECS map. This may also be helpful for inter-patient comparisons. In our work, values of *gmean(%)* were computed only for clinical cases.

To approximate *max_gmean*, one would need to find an artificial fMRI map that yields the best *gmean* score. A simple strategy to find such an activation map is to create a series of

artificial fMRI maps that yield decreasing sensitivity values from a maximum of 1.0 (with associated increasing specificity values from a minimum of 0). Fig. 6.3 shows an example of finding *max_gmean* for a simulated test case with two ON electrode pairs and 28 OFF electrode pairs. To create each artificial fMRI map, each voxel location is designated as activated if the combined ON electrodes current density distribution at that location exceeds a threshold (Fig. 6.3(b)). Each artificial fMRI map has a different threshold value, which starts from 0 where *all* voxels are designated as activated voxels (Fig. 6.3(c) – map 1), i.e., sensitivity of 1.0, specificity and *gmean* values of 0. As the threshold increases, the sensitivity decreases from 1.0 while the specificity, and hence *gmean*, increases from 0 as shown in Fig. 6.3(d). The increasing *gmean* will reach a maximum value and then start to decrease as the sensitivity tends to 0. The ordinate value in Fig. 6.3(d) at which the sensitivity, specificity and *gmean* plots intersect is the maximum *gmean* value.

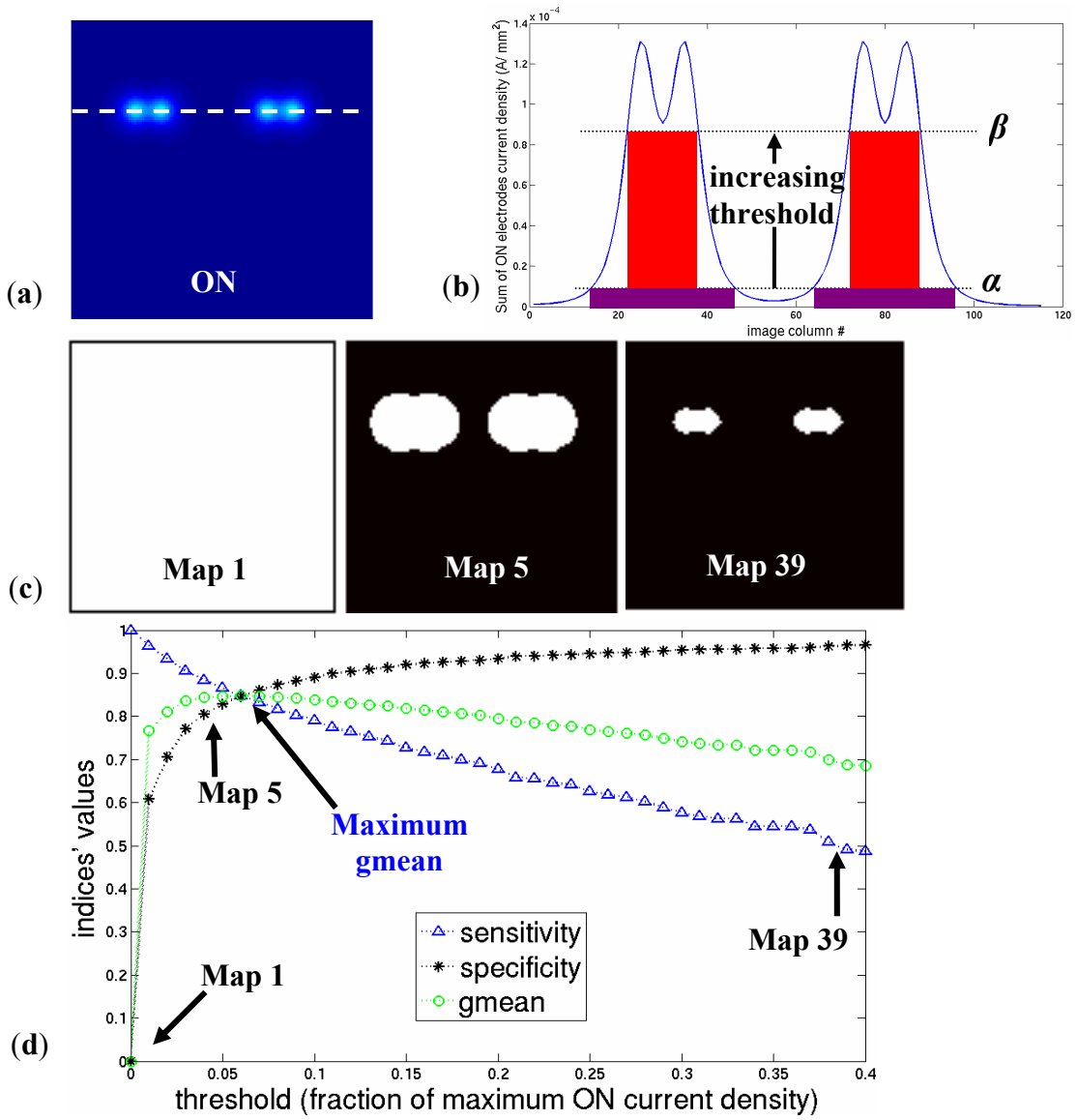

Figure 6.3: (**a**) Sum of two ON electrode pairs' current density maps (stimulated at 0.6 V) on a simulated 5-by-7 electrode grid. OFF electrode pairs' current density maps are not shown. (**b**) 1D profile plot of dashed line in (**a**) showing artificially activated voxels (solid shaded blocks) obtained by thresholding profile plot at two different threshold levels (α and β). Image columns spanned by red (taller block) and purple regions are designated as activated voxels for threshold levels β and α, respectively. (**c**) Samples from series of images showing artificially activated voxels which yield decreasing current density weighted sensitivity values (white denotes activated locations). Each map is generated by designating voxels in (**a**) that are above a threshold as activated. (**d**) Plot of proposed current density weighted sensitivity, specificity and gmean values for series of artificial fMRI maps generated with increasing threshold values. The sensitivity decreases from 1.0 while specificity increases from 0. The maximum possible gmean value, denoted by max_gmean, serves as a reference "best score" value for computed gmean values.

6.2.5 Numerical Approximation of Current Density

In ECS, the brain can be modeled as a volume conductor with no electrical charges within the conductor. A quasistatic condition is assumed where the temporal variations in the electrostatic quantities are ignored, i.e., only the steady-state scalar potential is of interest [49]. This condition corresponds to a snapshot in time when the maximum voltage magnitude is applied across the electrode pair and the electrostatic quantities are allowed to settle to an equilibrium state. For each stimulated electrode pair, the scalar potential field, $\Phi(\boldsymbol{r})$, is computed by solving the Laplace equation,

$$\sigma\nabla^2\Phi = \sigma\cdot\left(\frac{\partial^2\Phi}{\partial x^2}+\frac{\partial^2\Phi}{\partial y^2}+\frac{\partial^2\Phi}{\partial z^2}\right)=0\,, \tag{6.12}$$

where σ is the electrical conductivity. For simplicity, we assume that the volume conductor has isotropic conductivity, i.e., equal conductivity in all directions and σ is a scalar. The boundary conditions required for a unique solution include the applied voltage levels at the electrode-brain interface (Dirichlet boundary condition) and knowledge that the first derivative of the scalar potential perpendicular to the brain surface is zero (Neumann boundary condition)

$$-\sigma\nabla\Phi\cdot\boldsymbol{n}=0\,, \tag{6.13}$$

where $\boldsymbol{n}$ is a vector normal to the brain surface. The scalar potential maps are numerically computed using the finite difference method with 3D 7-element centered approximation. The Gauss Seidel algorithm was used to solve the resultant finite difference equations. The current density maps are then evaluated from the scalar potential field with Ohm's law

$$\boldsymbol{J}=-\sigma\nabla\Phi\ . \tag{6.14}$$

Fig. 6.4 shows top (a slice that is 6 mm below electrodes) and cross-sectional views of current density magnitude contour plots computed for a simulated 3D volume with two pairs of simulated electrodes stimulated at two different stimulus levels. The leftmost electrode pair has an input voltage magnitude of 0.6 V while the rightmost pair has an input voltage magnitude of 2.0 V. Assuming the electrode impedance is 60 Ω and ignoring all other impedances, this would be equivalent to injected current intensities of 10 mA and 33 mA, respectively. Fig. 6.4 illustrates that a higher electrical stimulus level induces a wider current density distribution spread.

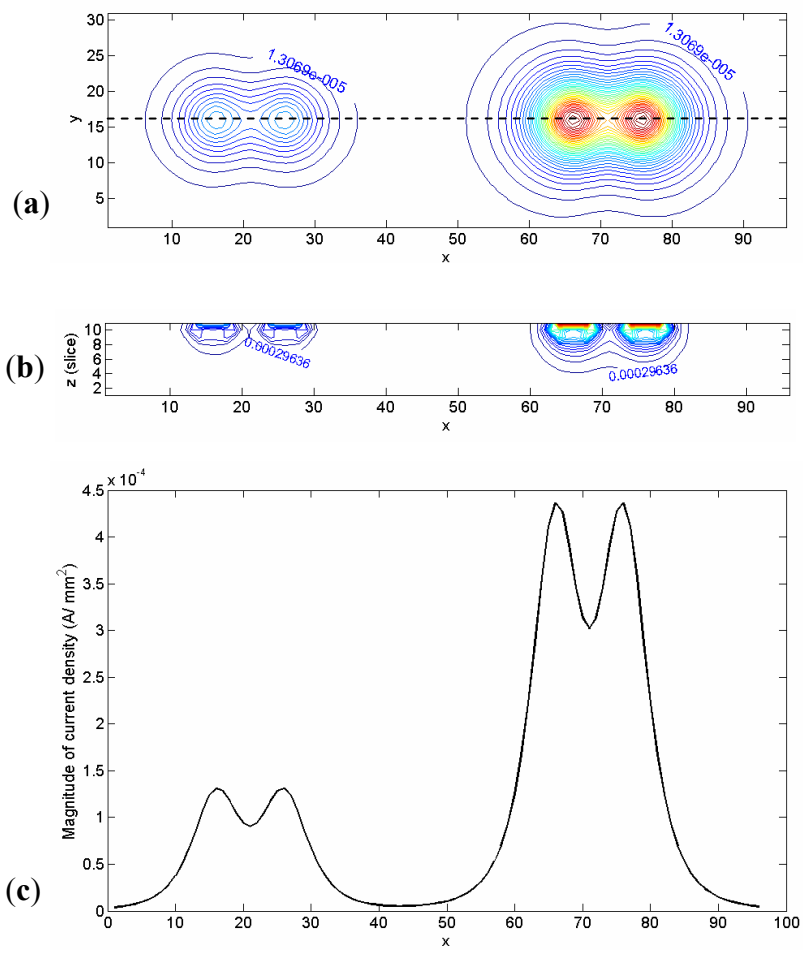

Figure 6.4: Current density magnitude for different simulated electrical stimulus levels (leftmost pair: 0.6 V, rightmost pair: 2 V). (**a**) Top view contour plot (6 mm below simulated electrodes positions), and (**b**) cross-sectional view contour plot (sliced along dashed line in (**a**)), and (**c**) 1D profile plot of (**a**) along dashed line in (**a**). The display range for both electrode pairs in each contour plot is the same to facilitate the comparison of current density distribution spreads at different electrical stimulus levels.

6.2.6 Data Simulation

In this section, simulated datasets are used to compare the current density weighted statistical indices to the voxel-based fixed radii method indices and the Euclidean distances from ON electrodes to nearest fMRI clusters' edges and centroids. A 115×115×100 voxel (115mm×115mm×100mm) 3D rectangular volume (MRI) with an overlaid electrode grid (CT) with known stimulation voltages was simulated. For simplicity, each voxel is assigned the electrical conductivity value of brain grey matter (0.004 Ω^{-1} cm^{-1}). Each circular electrode has a radius of 2 mm and adjacent electrodes are spaced 10 mm in both vertical and horizontal directions. Each voxel is 1 mm×1 mm×1 mm in size. It is assumed that all simulated fMRI

activation maps are in the same coordinate space as, i.e., spatially aligned to, the simulated 3D rectangular MRI volume. Simulated datasets are useful in this phase of the study because the locations of activated voxels, shapes of activation clusters, ON and OFF electrode pair combinations as well as different current stimuli levels can be specified and thus allow precise characterization of the performance indices under different conditions. It also allows the evaluation of these indices against qualitative knowledge of what constitutes good ECS-fMRI correspondence in different cases.

The simulated test cases are *labeled* as combinations of three sub-categories of test cases: ECS, fMRI and electrical stimulation level test cases (Fig. 6.5). Each ECS test case has a specific ON and OFF electrode pair combination that is analogous to a specific patient-task ECS map. Each ECS test case, denoted by E1 to E6, can be combined with fMRI activation test cases F1 to F2 and stimulation level test cases S1 to S2 to simulate different ECS-fMRI map combinations. The activation clusters in fMRI test cases F1 to F2 are not static, i.e., the clusters are moved together across the whole image to simulate different fMRI activation maps for which correspondence indices are computed. The positions of each cluster relative to other clusters do not change but some clusters near the edge of the image may be shifted outside the field of view, i.e., outside the visible part of the image. A 2D map is thus obtained for each correspondence index for each test case from which 1D profile plots are extracted and shown in Figs. 6.7 to 6.15. These 1D plots serve to illustrate specific advantages of using the current density weighted correspondence indices and their behavior under different conditions. A specific ECS-fMRI-stimulation level combination is denoted by the concatenation of their labels shown in Fig. 6.5, e.g., E1-F1-S1 denotes ECS test case E1 with fMRI test case F1 and electrical stimulation level test case S1.

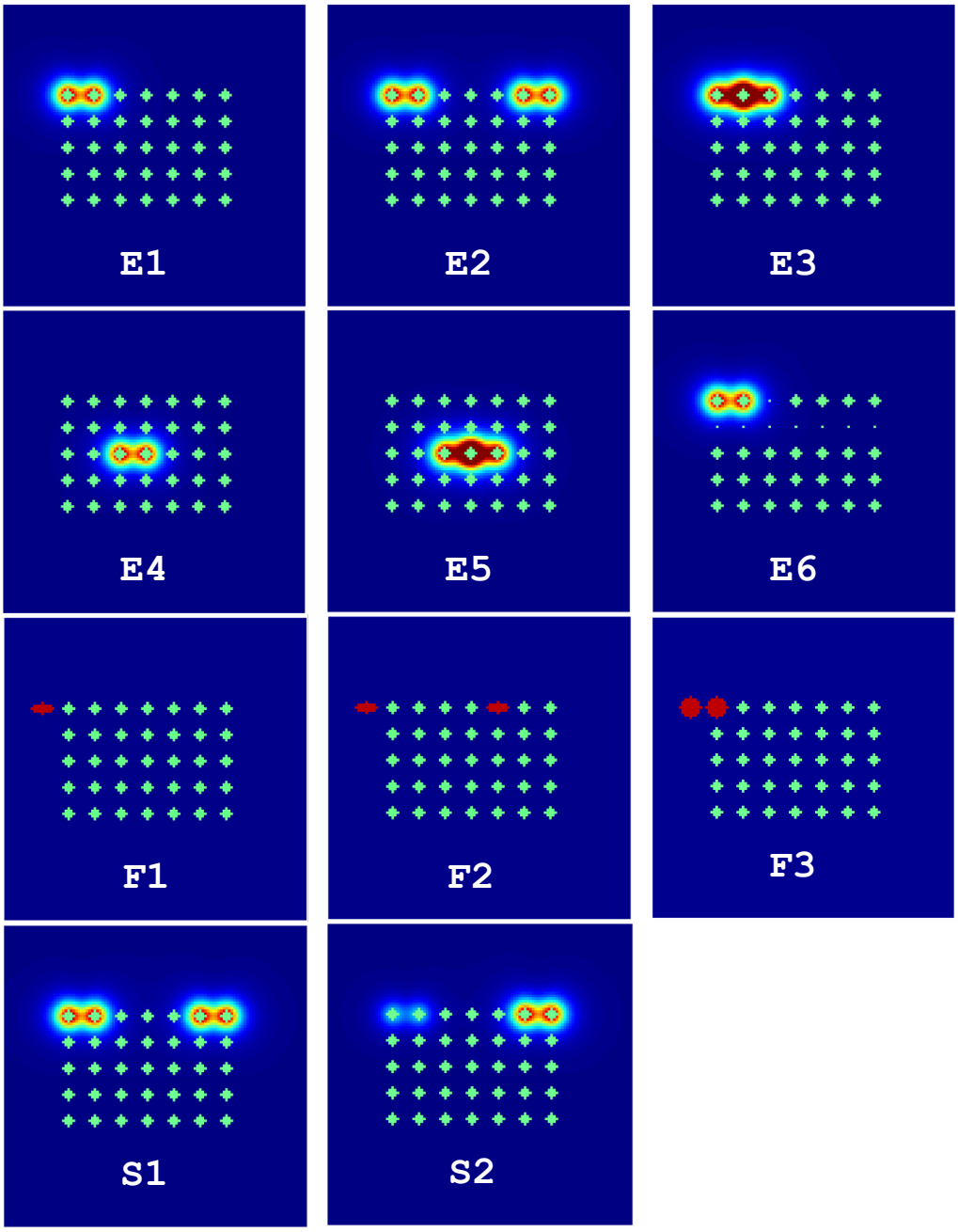

Figure 6.5: Electrode grid overlaid on current density maps (6 mm below electrodes) for simulated ECS maps labeled E1 to E6. In E1 to E6, high current density regions (orange-red regions) indicate locations of ON electrode pairs. All other horizontally adjacent electrode pairs are either OFF electrode pairs (diamonds) or untested (dots on grid), e.g., ECS map E6. F1 to F3 denote simulated fMRI activation test cases where activated voxels are grouped into solid red ellipses (F1, F2) or circles (F3). S1 uses an input peak voltage of 0.6 V for *all* ON and OFF electrodes. Test case S2 uses an input peak voltage of 0.2 V for the leftmost and 0.6 V for the rightmost ON electrode pairs. All OFF electrodes for all test cases have stimulus voltages of 0.6 V.

6.2.7 Clinical Data

6.2.7.1 MR Imaging and Extraoperative ECS Functional Mapping Overview

Fig. 6.6 shows an overview of the fMRI and ECS mapping procedure prior to surgery for lesion resection. An MRI T1-weighted pre-grid anatomical reference volume was acquired in the same scan session as T_2^*-weighted fMRI time series images corresponding to various specified test paradigms. A fully automated 3D nonlinear registration process using our Mutual Information Automated Multimodality Image Fusion (MIAMI Fuse) software [24] was then used to register the T_2^*-weighted fMRI time series to the T1-weighted anatomical reference volume. In addition, 2D to 3D rigid body mapping of slice-to-volume (MSV) was performed to improve motion correction accuracy [25]. Statistical analysis was then performed on the resultant motion corrected datasets to compute fMRI activation maps that indicate the regions of the brain that have increased Blood Oxygenation Level Dependent (BOLD) response to the specified stimuli. With the MSV motion correction technique, slices are repositioned to account for inter-slice motion. In most data sets, out-of-slice motions are detected and unequal number of temporal samples per voxel may be observed. A robust approach in statistical testing using random permutation was chosen to compute the fMRI activation maps [40]. This statistical technique is simple, non-parametric and independent of sample size variability [41].

Following the pre-grid MR scans, the patient undergoes the first craniotomy to implant a subdural electrode grid. Post-grid computed tomography (CT) and MRI scans are subsequently performed. The CT volume is then registered to the post-grid MR volume using the MIAMI Fuse software. To bring the post-grid registered CT volume in alignment with the pre-grid MR anatomical volume, the post-grid MR volume is non-linearly registered to the pre-grid MR volume and the resultant deformation field is applied to the pre-grid CT volume as shown in Fig. 6.6. Consequently, both the fMRI activation and CT datasets are non-linearly registered to the pre-grid MR reference volume. The electrode positions are extracted semi-automatically via *k*-means clustering [56] of the intensity-thresholded CT volume.

Just before the second craniotomy, three sets of information are available for each patient: a T1 pre-grid anatomical reference volume, several sets of fMRI activation maps for different paradigms (e.g., responsive naming and picture naming), and a post-grid CT volume which shows ON and OFF electrode pair locations along with maximum stimulation current levels applied. These datasets are all registered to the T1 pre-grid anatomical reference. The primary interest in our work is to quantify the "closeness" of the fMRI activation maps to their corresponding ECS functional maps.

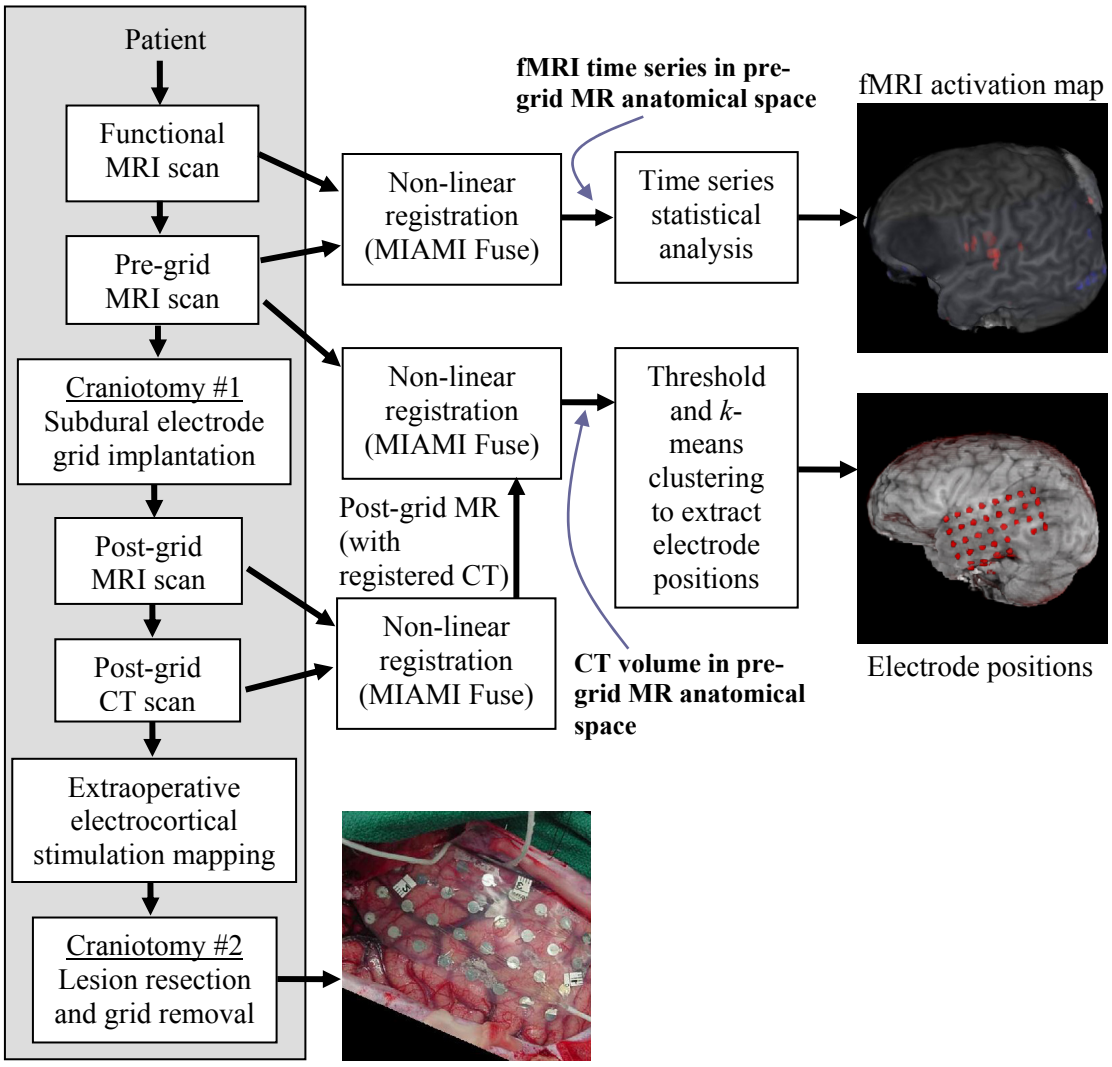

Figure 6.6: Overview of fMRI and ECS mapping procedure for patients undergoing surgery for lesion removal.

6.2.7.2 Electrocortical Stimulation Mapping

Bipolar constant current electrocortical stimulation (ECS) is performed extraoperatively with the injection of constant current pulses across adjacent electrode pairs. For each electrode pair, the patient was asked to perform a task while the current intensity was gradually increased. If a stimulated region is essential to the task, an adequate stimulation current intensity may alter function [57] and inhibits performance of the task. Stimulated electrode pairs that yield a response (ON electrodes) during a specified task (activation or inhibition) are labeled with the injected current levels when the response is observed. The precise locations of the inhibited

neurons under the ON electrodes are not available from the ECS procedure. However, the location of each electrode and a map of ON and OFF electrode pairs are available.

During ECS mapping with the implanted subdural grid electrodes (Ad-Tech Medical Instrument Corp., Racine, WI, USA), stimulus biphasic current with a pulse duration of 300 μs and a pulse interval of 20 ms (frequency of 50 Hz) was applied across horizontally adjacent electrode pairs using a Grass Model S12 isolated biphasic stimulator (Astro-Med Inc., West Warwick, RI, USA). The pulse train duration used was 2 s. Each electrode has an exposed diameter of 2.3 mm and an approximate electrical resistance of 50 to 60 Ω. The spacing between the centers of adjacent electrodes is 10 mm. During ECS mapping, the current intensity is gradually increased from 1 mA for motor and sensory mapping, and 3mA for language mapping until either a response is detected or significant afterdischarges are observed. Responses are confirmed by observing consistent effects with repeated stimulation. The injected current intensity increases in steps of 1 mA for motor/ sensory and 3 mA for language mapping. The final applied voltages for each stimulated electrode pairs are approximated by multiplying the peak injected current intensity by the electrode impedance (Ohms's law). The Grass S12 stimulator allows the peak voltages to be read during stimulation, which may yield more accurate approximations of the actual applied voltage levels for future patient studies.

6.3 Results

6.3.1 Simulation Data Results

Figs. 6.7 to 6.15 show plots of correspondence indices for various combinations of ECS map, fMRI map and stimulus level test cases described in Fig. 6.5. In this section, the characteristics of the current density weighted indices are reported for each test case combination, and then compared to the voxel-based fixed radii and Euclidean distance methods where appropriate. The test cases presented are inter-related to each other in that subsequent test cases are often more complicated variations of previous test cases. Figs. 6.7 to 6.15 each consists of five parts. Part A shows the current density maps with overlaying electrode grids and fMRI cluster(s) moving from the left to right sides of the images. Part B shows the current density weighted counts of *TP*, *FP* and *FN* as the centroids of the *leftmost* fMRI cluster (if there are more than one cluster, i.e., F2 and F3) move along the dashed line displayed in part A. Part C shows the current density weighted ECS-fMRI correspondence indices while parts D and E show the voxel-based fixed radii method and Euclidean distance method correspondence indices, respectively.

The simplest test case, labeled E1-F1-S1 (Fig. 6.7(a)), has an elliptical fMRI activation cluster of radii 2 mm and 4 mm along the minor and major axes of the ellipse respectively. As the fMRI cluster moves across the dashed line in Fig. 6.7(a), the current density weighted true positives (*TP*) plot (Fig. 6.7(b)) peaks when the cluster is directly under each of the two ON electrodes. This leads to corresponding valleys in the *FN* plot since (*TP*+*FN*) is a constant for any ECS map, i.e., sum of Eqns. 1 and 4 is a constant. The resultant sensitivity plot (Fig. 6.7(c)) is bimodal or double-peak, which indicates higher ECS-fMRI correspondence for fMRI activated voxels ($m(\boldsymbol{r})=1$) that are nearer any ON electrode. Since there are 29 pairs of OFF electrodes in Fig. 6.7(a), the number of true negatives (*TN*) is much larger than *FP*, thus yielding a specificity plot (Fig. 6.7(c)) with all values close to 1.0. The *gmean* plot has a similar shape as the sensitivity plot (Fig. 6.7(c)) and summarizes classification accuracies for both true positives and true negatives. Local minima in the sensitivity and *gmean* plots, which become more pronounced as the inter-electrode spacing increases, are also observed in between the two ON electrodes. The sensitivity and *gmean* plots computed using the voxel-based fixed radii method (Fig. 6.7(d)) are zero outside the fixed windows and rises/ falls abruptly at the edges of the windows. Plateaus are also observed in the fixed radii sensitivity and *gmean* plots when the fMRI cluster is located within the fixed windows of the ON electrodes. As long as the fMRI cluster is completely within the fixed windows, the voxel-based fixed radii method reports constant sensitivity and *gmean* values, making it difficult to assess incremental improvements/ deterioration in fMRI performance. For example, an fMRI cluster located within the radii and moving closer to an ON electrode will still yield similar indices' values. This limitation is exacerbated by the lack of a principled method to decide how large the stimulation radius should be, e.g., a larger radius will yield wider plateaus in the sensitivity and *gmean* plots making it even less effective in tracking incremental improvements in fMRI maps. The mean of the minimum electrode-edge and electrode-centroid Euclidean distances have global minima, indicating best ECS-fMRI correspondence, in between the ON electrodes (Fig. 6.7(e)). This implication that an fMRI cluster located in between ON electrodes would yield the best correspondence is not based on any electrostatic or physiological evidence, especially in light of computed current density maps that show maximum electrical stimulus levels directly under ON electrodes, rather than in–between them.

Test case combination E1-F3-S1 (Fig. 6.8(a)) illustrates the improvement in ECS-fMRI correspondence when two larger fMRI activation clusters, each of radius 4 mm and spaced 10 mm apart, are found in high energy regions of the ON electrode pair's current density map. As the number of fMRI activated voxels around ON electrodes increases at locations where current

density magnitude values are highest, the current density weighted sensitivity values will increase and tend to a maximum value of 1.0. The maximum current density weighted sensitivity value in Fig. 6.8(c) is much higher (0.69) than that of Fig. 6.7(c) (0.45) due to the larger number of true positives (*TP*) in the former. The maximum sensitivity and *gmean* values occur when the two fMRI clusters are simultaneously located under the two ON electrodes.

In test case E1-F2-S1 (Fig. 6.9(a)), a second elliptical fMRI activation cluster, spaced five electrodes away from the leftmost cluster in Fig. 6.7, was added. The number of true positives (Fig. 6.9(b)), due largely to the leftmost cluster, is approximately the same as test case E1-F1-S1 in Fig. 6.7(b) but the number of false positives has increased because of the rightmost cluster. As such, the current density weighted sensitivity values in Fig. 6.9(c) does not change appreciably while a slight decrease in specificity values is observed. The decrease in specificity is not large because there are many OFF electrodes, i.e., *TN* is large.

Test case E2-F1-S1 (Fig. 6.10(a)) uses the same elliptical fMRI activation cluster as in Fig. 6.7(a) but with two ON electrode pairs. The current density weighted sensitivity and *gmean* plots (Fig. 6.10(c)) have similar shapes to those in Fig. 6.7(c) (test case E1-F1-S1). The maximum sensitivity and *gmean* values in Fig. 6.10(c), however, are smaller (0.10, 0.31 respectively) because for every location that the fMRI cluster visits, *FN* has increased due to the presence of the additional ON electrode pair. This is desirable since the indices report poorer correspondence when there is an additional ON electrode pair, without any fMRI activation under it. This is unlike the current density weighted *PPV* which has same maximum values in both Figs. 6.7(c) and 6.10(c), which is an undesirable feature. The means of the Euclidean distances in Fig. 6.10(e) have minima in-between the two pairs of ON electrodes. This indicates that an fMRI cluster found directly under an ON electrode can have worst or equal ECS-fMRI correspondence than an identical cluster that is equidistant from all ON electrodes, but yet is not near any ON electrode. This assignment of highest ECS-fMRI correspondence to potentially improbable occurrences of stimulation-induced neuronal activation runs contrary to evidence that bipolar ECS stimulation is localized around ON electrode pairs [49].

Test case E2-F1-S2 (Fig. 6.11(a)) is identical to Fig. 6.10(a) except that the leftmost ON electrode pair is stimulated at 0.2 V instead of 0.6 V as used in the rightmost ON electrode pair. The local maxima of the current density weighted sensitivity and *gmean* plots are higher under the leftmost ON electrode pair (0.05, 0.22 respectively) than the rightmost ON electrode pair (0.15, 0.38). This may be desirable because higher electrical stimulus levels increases both the magnitude and spread of the current density distribution (Fig. 6.4), thus increasing the spatial extent of the stimulated region, as well as the range of neuronal stimulation thresholds that the

stimuli may overcome. The voxel-based fixed radii method does not incorporate information on stimulus levels as illustrated in the plateaus of similar maximum values under both pairs of ON electrodes in the sensitivity and *gmean* plots of Fig. 6.11(d).

In test case E3-F1-S1 (Fig. 6.12(a)), two overlapping pairs of horizontally adjacent electrodes are stimulated. The second ON electrode, where the summed current density map values are highest, is more likely to be near task-related neuronal regions than neighboring ON electrodes since it was stimulated twice and both its horizontally adjacent neighbors are also ON electrodes. Indeed, maximum current density weighted sensitivity and *gmean* values are observed when the fMRI cluster is located directly under the second ON electrode. The fixed radii sensitivity and *gmean* plots (Fig. 6.12(d)) have plateaus across the three ON electrodes and is not able to extract such contextual information.

Test cases E4-F1-S1 (Fig. 6.13(a)) and E5-F1-S1 (Fig. 6.14(a)) are similar to Figs. 6.7(a) and 6.12(a), respectively, except that the ON electrode pairs in the former are now surrounded by OFF electrodes. There are no noticeable changes in the shape or maxima values (sensitivity: 0.19, specificity: 1.00, *gmean*: 0.44) in the current density weighted sensitivity, specificity and *gmean* plots. This implies that the presence or absence of OFF electrodes around ON electrodes does not significantly affect the ECS-fMRI correspondence when an fMRI cluster is found under an ON electrode. This is desirable if OFF electrodes are defined as stimulated electrodes that did not yield a task-related inhibitory response. In this case, it cannot be conclusively stated that regions under these electrodes do not have task-essential neuronal tissue, even though the likelihood of that should be higher compared to an untested electrode pair. It might be that the electrical stimulus level was just not high enough. Thus, it would be premature to penalize ECS-fMRI correspondence values when an fMRI cluster is located near ON electrodes surrounded by OFF electrodes.

Test case E6-F1-S1 (Fig. 6.15(a)) is identical to E1-F1-S1 (Fig. 6.7(a)) except that several electrodes surrounding the ON electrode pair are not tested (neither ON nor OFF). The current density weighted sensitivity, specificity and *gmean* plots are similar in both Figs. 6.15(a) and 6.7(a) with similar maximum values as Figs. 6.13(c) and 6.14(c). This illustrates an example of how neighboring OFF and untested electrodes are similar in their effect on current density weighted indices.

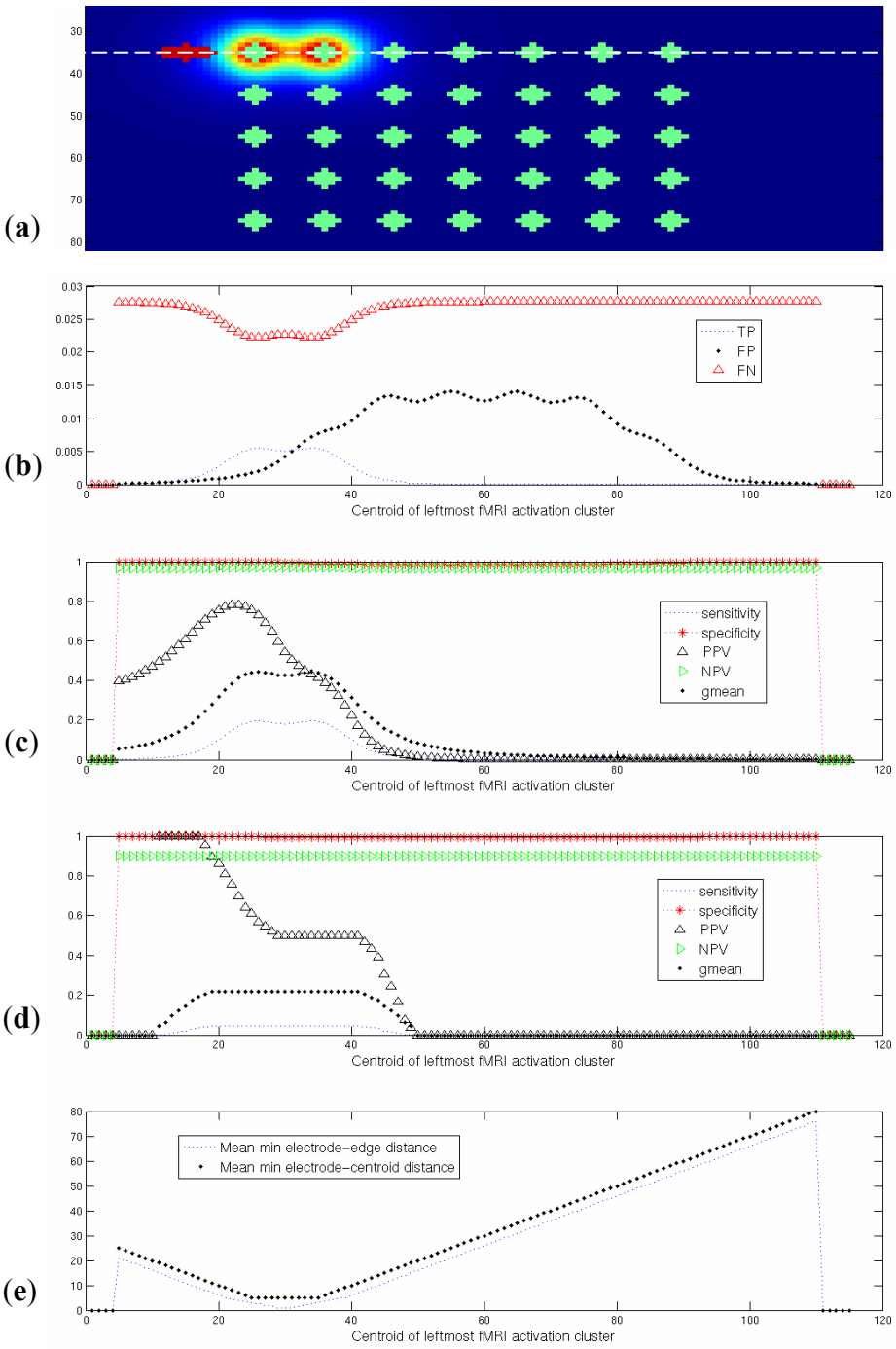

Figure 6.7: Simulated dataset E1-F1-S1. (**a**) Current density map overlaying electrode grid with an fMRI cluster moving from left to right side of image. (**b**) Current density weighted *TP*, *FP* and *FN* as centroid of left fMRI cluster moves along dashed line in (**a**). (**c**) Current density weighted ECS-fMRI correspondence indices. (**d**) Fixed radii method correspondence indices. (**e**) Euclidean distance method.

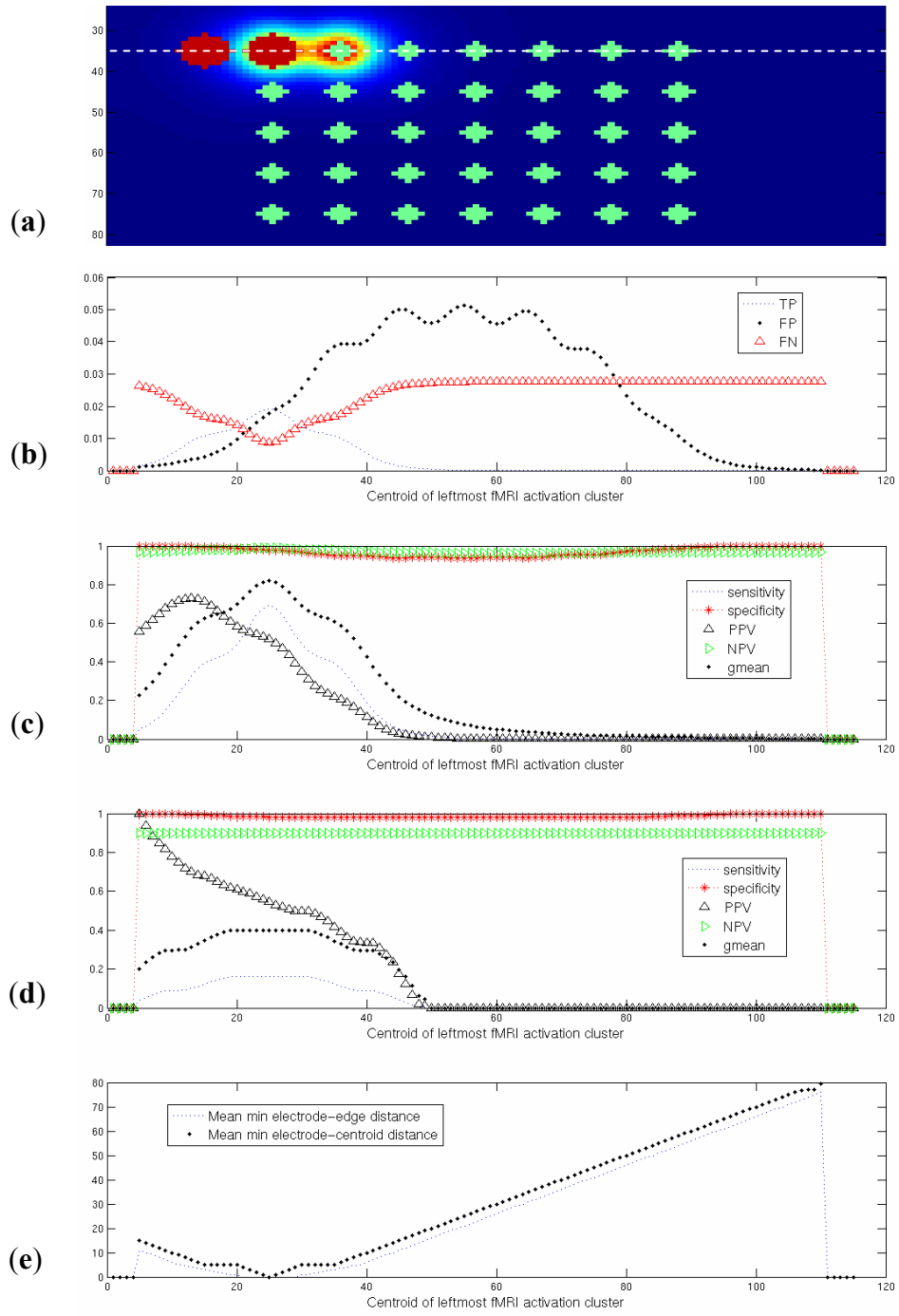

Figure 6.8: Simulated dataset E1-F3-S1. This test case has larger fMRI clusters compared to Fig. 6.7 and illustrates that higher peak values of sensitivity and *gmean* are obtained (compared to Fig. 6.7) when more fMRI voxels occur in regions with high current density energy levels, i.e., near ON electrodes. Parts (**a**) to (**e**) denote images and plots as described in Fig. 6.7.

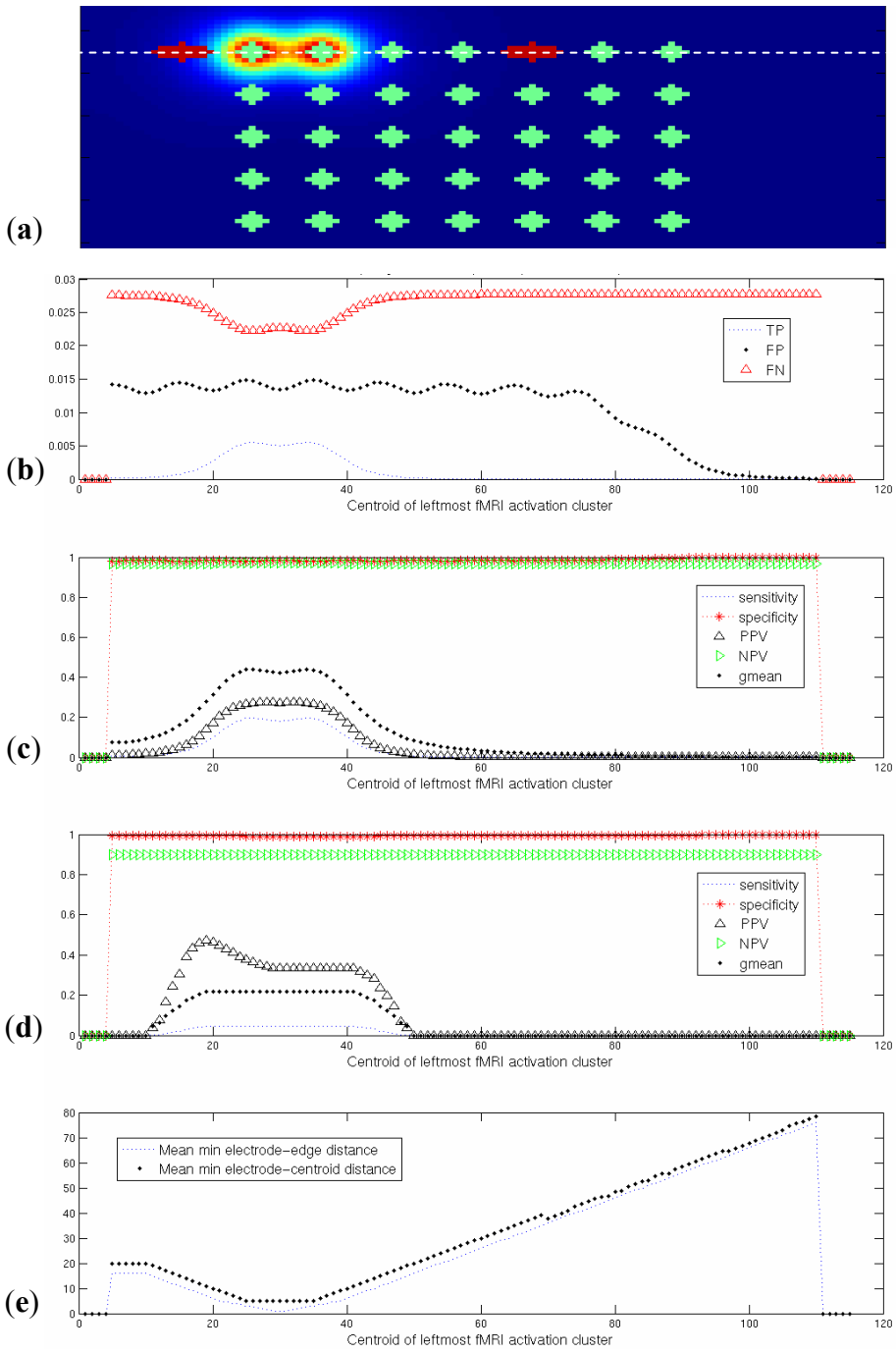

Figure 6.9: Simulated dataset E1-F2-S1. In this test case, a second (rightmost) fMRI cluster, i.e., additional false positives, was added to the cluster (leftmost) in Fig. 6.7. Parts (**a**) to (**e**) denote images and plots as described in Fig. 6.7.

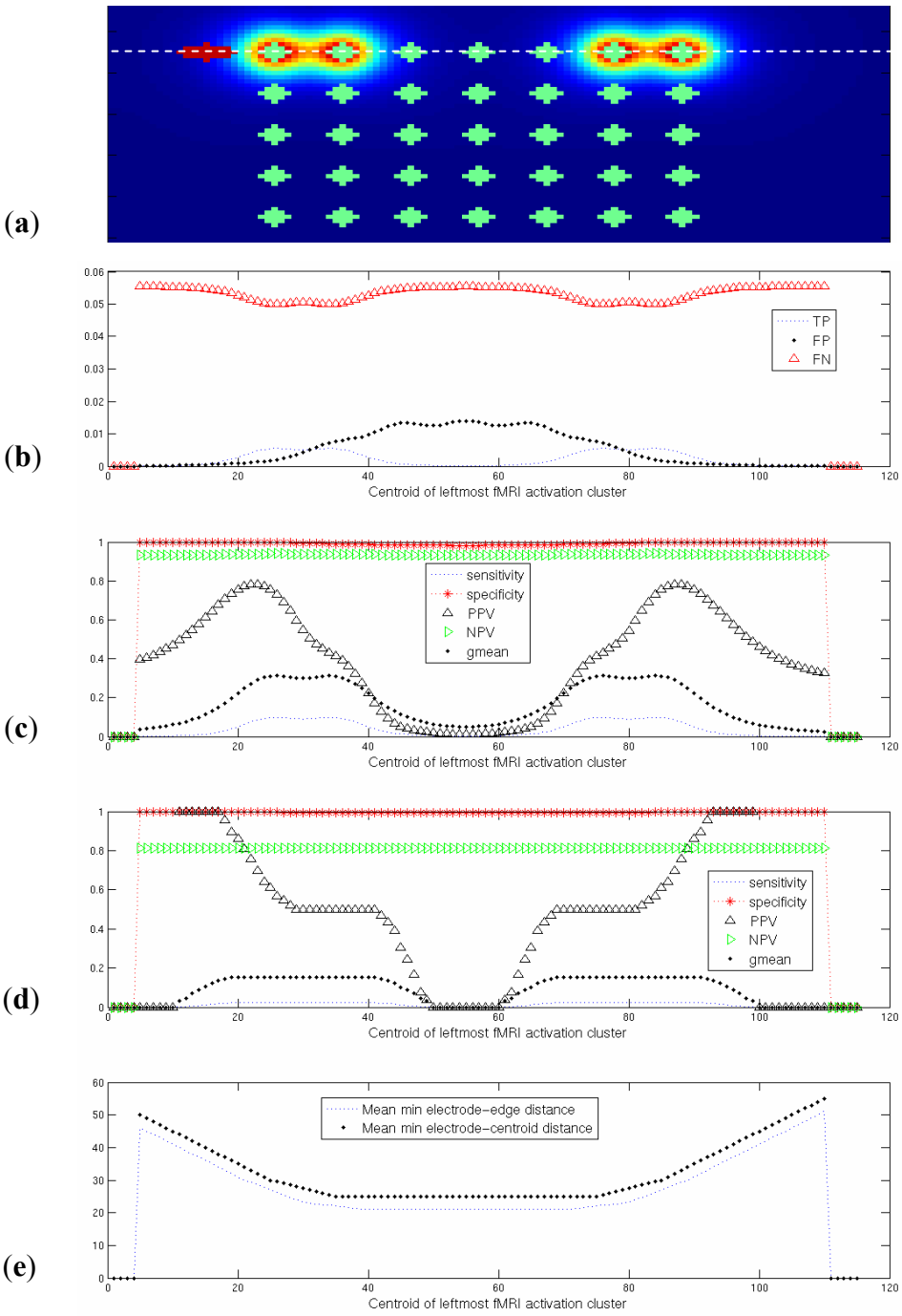

Figure 6.10: Simulated dataset E2-F1-S1. This test case is similar to Fig. 6.7 except for an additional ON electrode pair (rightmost). It illustrates the effects of additional false negative voxels and highlights a limitation of Euclidean distance-based indices. Parts (**a**) to (**e**) denote images and plots as described in Fig. 6.7.

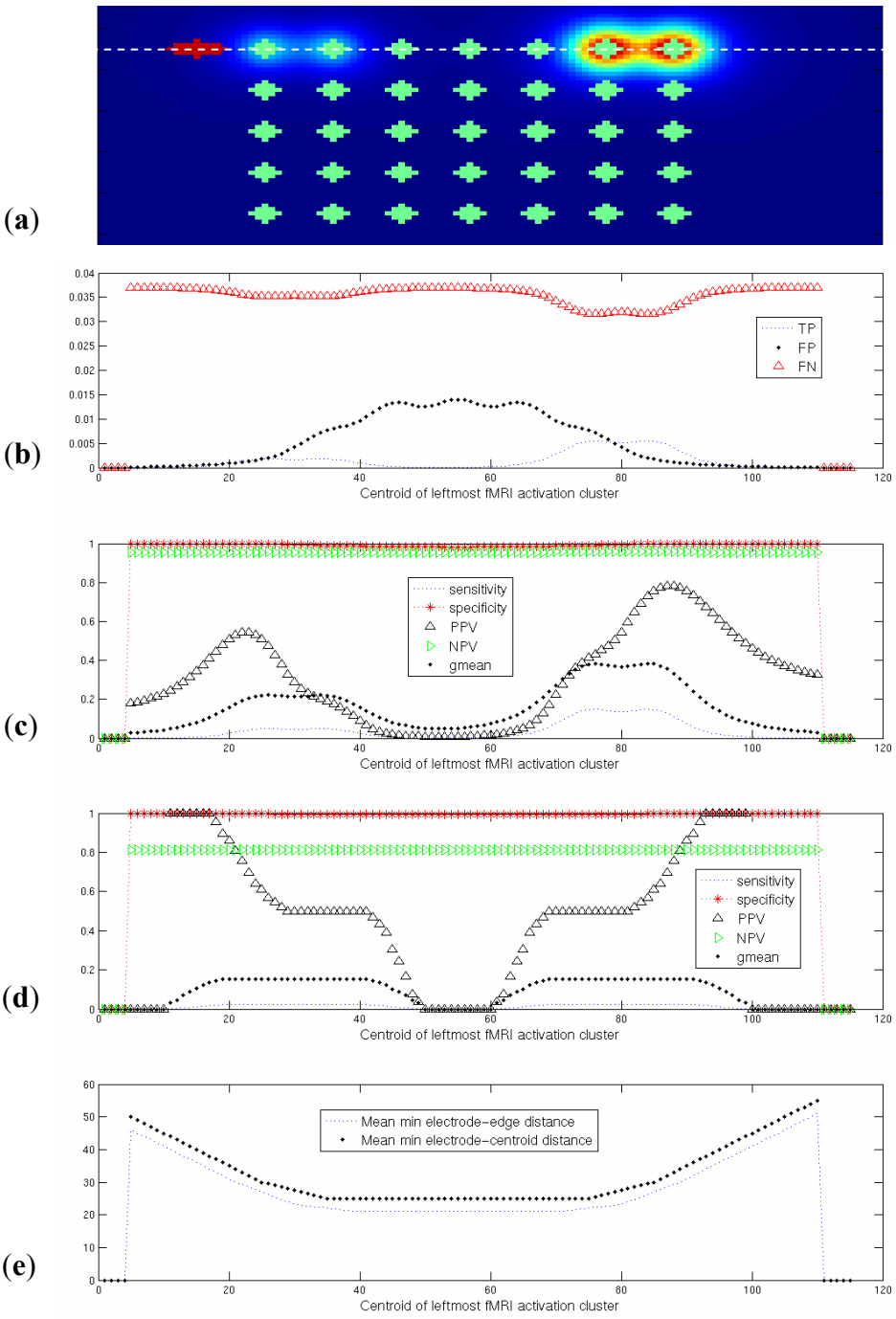

Figure 6.11: Simulated dataset E2-F1-S2. This test case is similar to Fig. 6.10 except that the leftmost ON electrode pair was stimulated at 0.2 V while the rightmost ON pair was stimulated at 0.6 V. In Fig. 6.10, both ON electrode pairs were stimulated at 0.6 V. Parts (**a**) to (**e**) denote images and plots as described in Fig. 6.7.

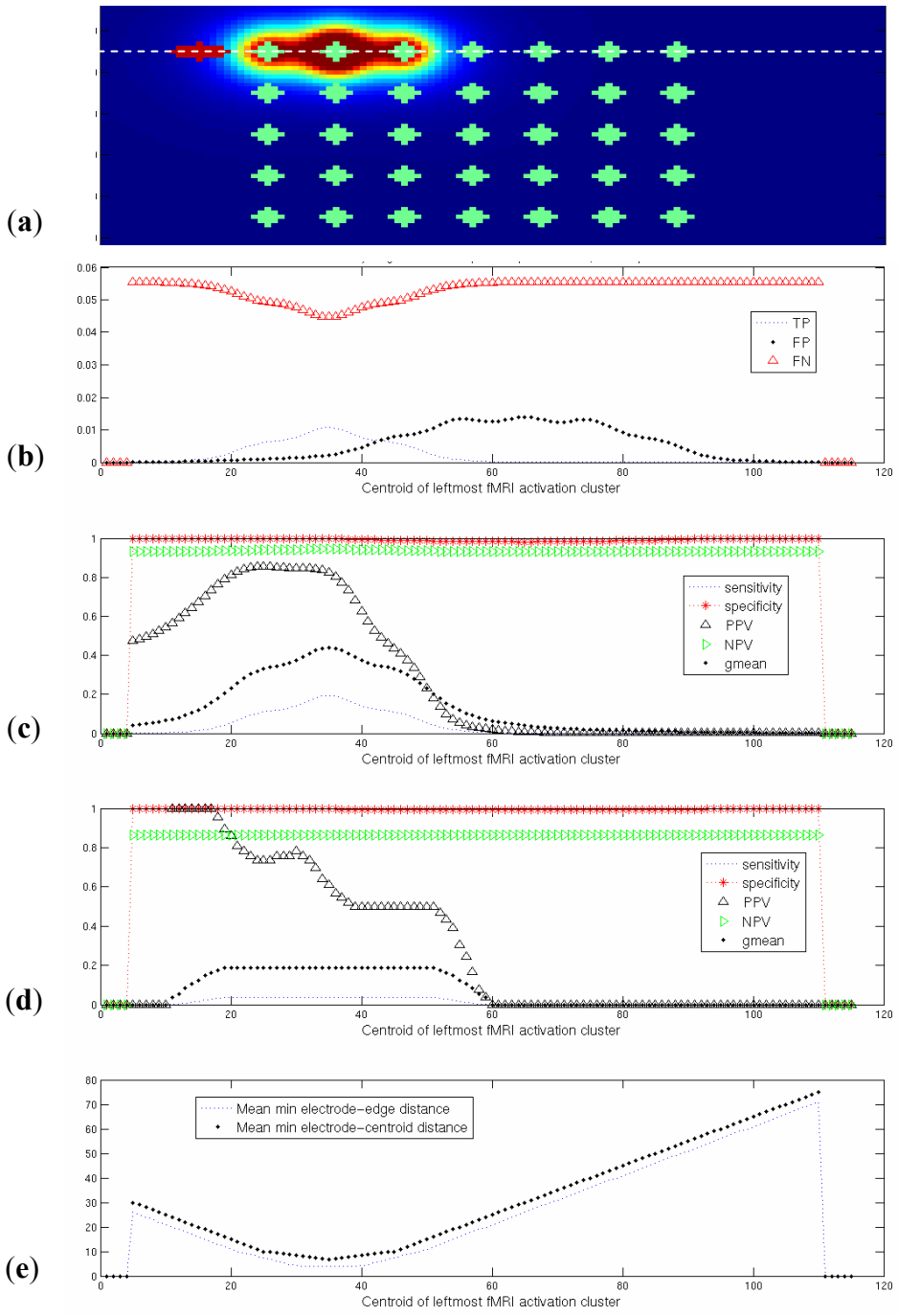

Figure 6.12: Simulated dataset E3-F1-S1. This test case is identical to Fig. 6.7 except for the addition of an adjacent ON electrode pair (rightmost). Parts (**a**) to (**e**) denote images and plots as described in Fig. 6.7.

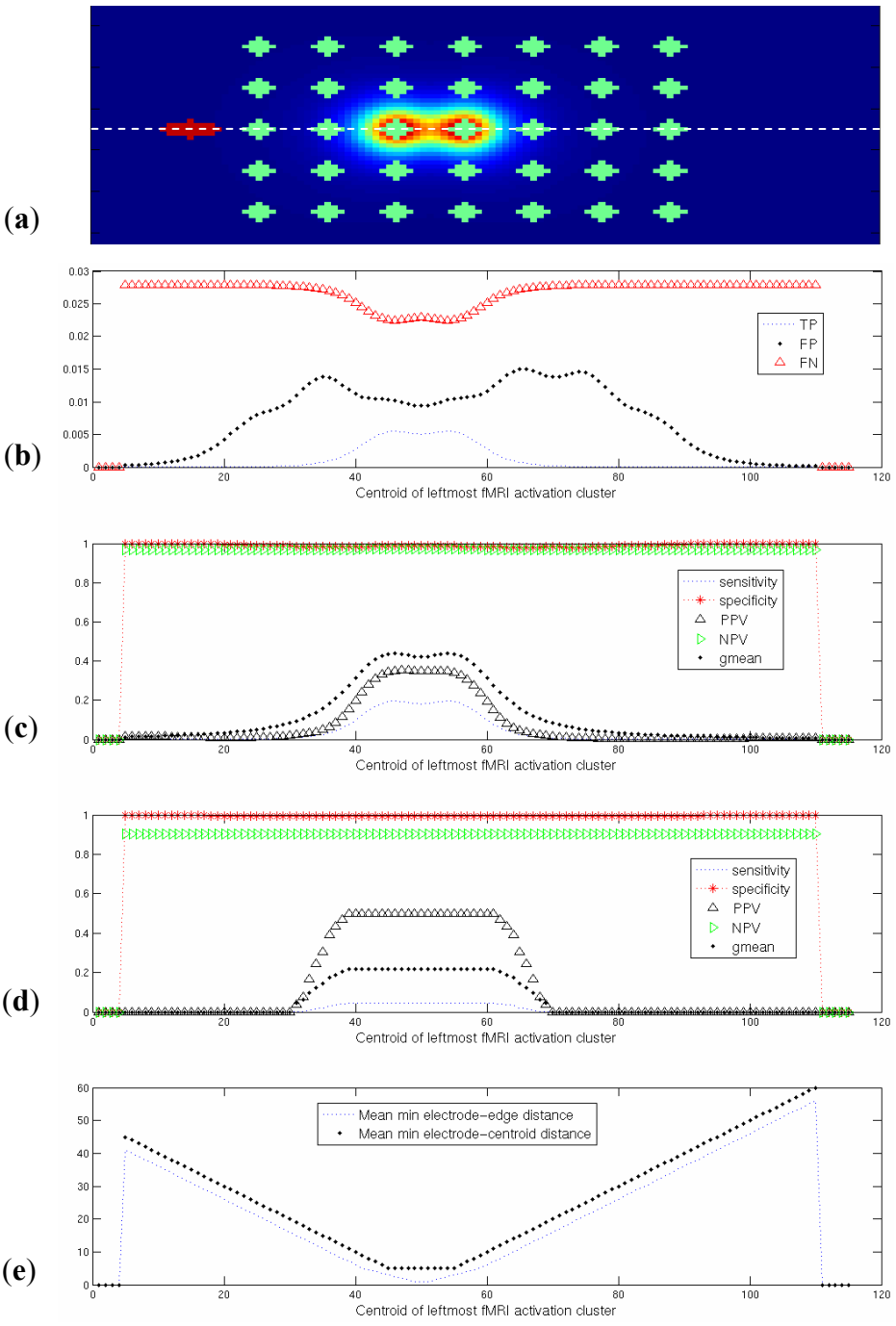

Figure 6.13: Simulated dataset E4-F1-S1. This test case is similar to Fig. 6.7 except that the ON electrode pair is now surrounded by OFF electrode pairs. Parts (**a**) to (**e**) denote images and plots as described in Fig. 6.7.

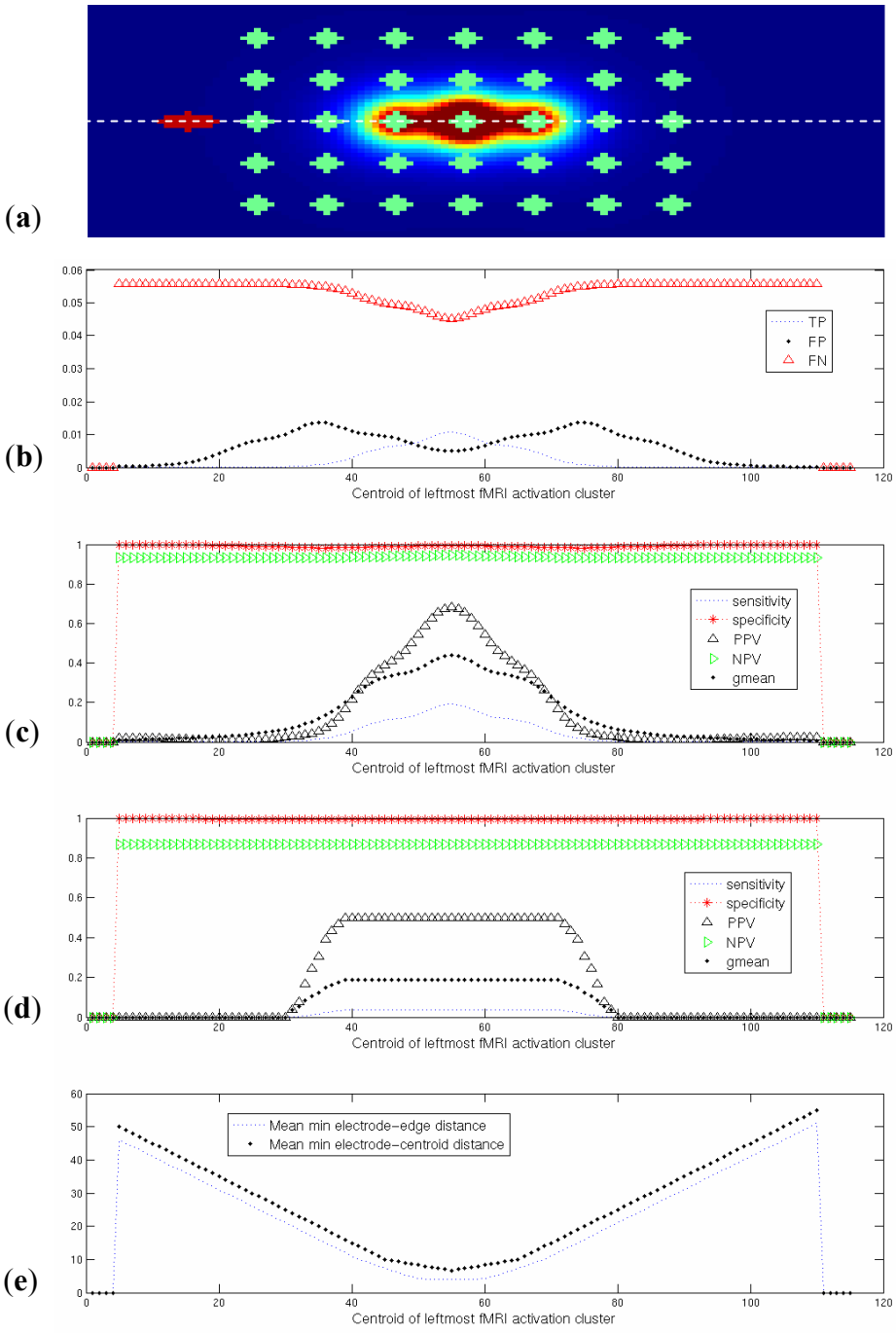

Figure 6.14: Simulated dataset E5-F1-S1. This test case is similar to Fig. 6.12 except that the ON electrode pairs are now surrounded by OFF electrode pairs. Parts (**a**) to (**e**) denote images and plots as described in Fig. 6.7.

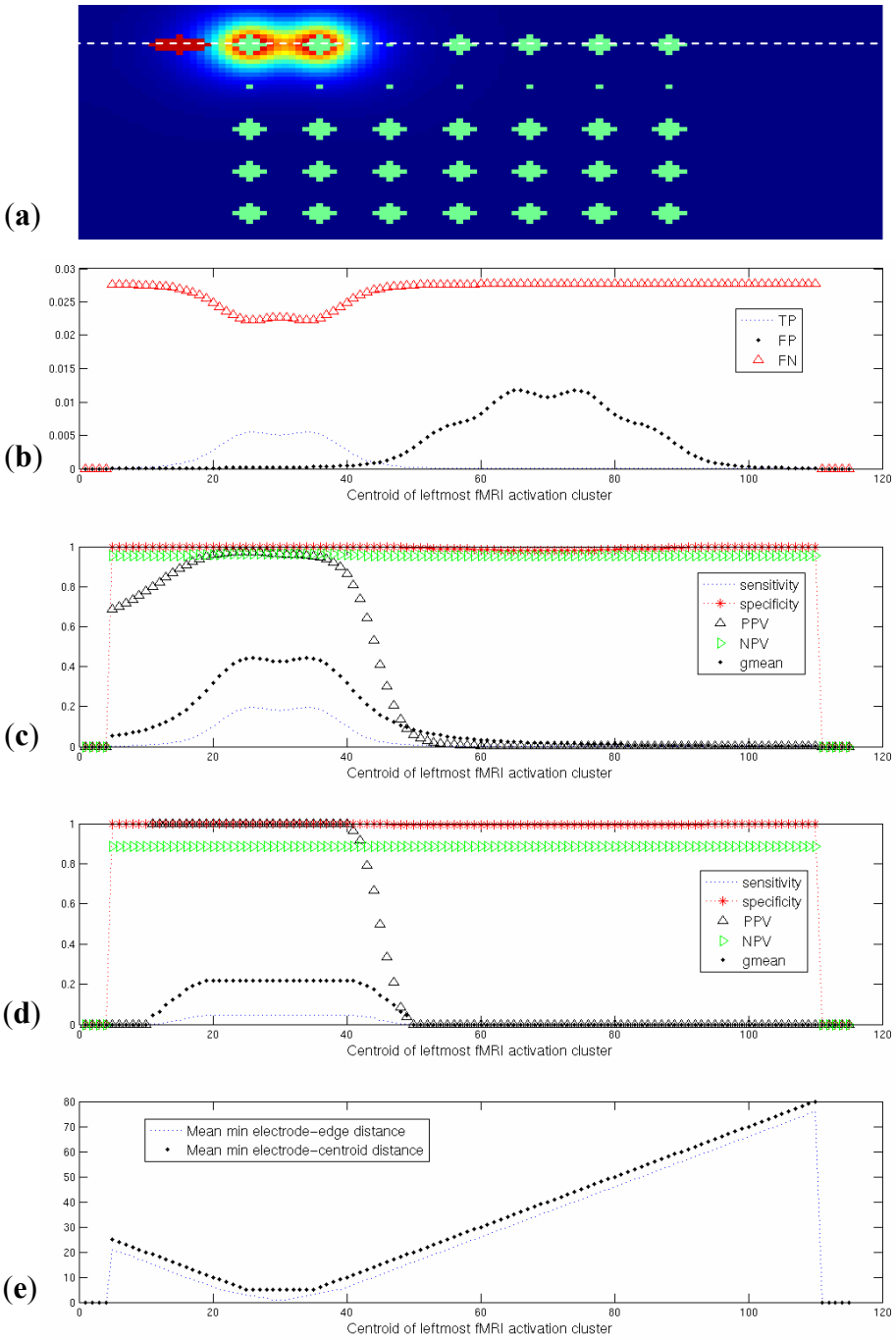

Figure 6.15: Simulated dataset E6-F1-S1. This test case is similar to Fig. 6.7 except that several electrode pairs around the ON electrode are not tested (dotted locations). Parts (**a**) to (**e**) denote images and plots as described in Fig. 6.7.

6.3.2 Clinical Human Data

Fig. 6.16 shows a cross-sectional view of the ECS current density distributions for three patients overlaid on non-linearly registered post-grid CT images. The current density weighted correspondence indices for all three patients are shown in Tables 6.1 to 6.3. The maximum possible *gmean* values, with which *gmean(%)* values in Tables 6.1 to 6.3 were computed, are approximately the same for all three patients (0.78, 0.80 and 0.80, respectively) so it is reasonable to use either *gmean* or *gmean(%)* when comparing ECS-fMRI correspondence across these patients. Fig. 6.17 shows the picture and responsive naming fMRI activation maps, and electrode grids, overlaid on the anatomical MR datasets for all three patients. In Table 6.1, the *gmean* and sensitivity values (0.26 and 0.07, respectively) for the picture naming paradigm for patient 1 are the largest among all other datasets. Fig. 6.17(a) (patient 1 - picture naming) shows that a dense cluster of fMRI activation occurs in the proximity of at least two ON electrodes while Fig. 6.17(b) (patient 1 - responsive naming) has a smaller fMRI cluster in close proximity to one ON electrode. Thus, recalling the results of the simulation test cases in Fig. 6.7 and Fig. 6.8 where the activation cluster in the latter was increased in size and covered more of the high energy regions of the current density distribution, it is expected that the sensitivity and *gmean* values for Fig. 6.17(a) would be higher than those for Fig. 6.17(b). In Fig. 6.17(c) (patient 2 - picture naming) and Fig. 6.17(d) (patient 2 - responsive naming), hardly any fMRI activation was detected in the vicinity of ON electrodes. Also, Figs. 6.17(c) and 6.17(d) have five more ON electrode pairs than Figs. 6.17(a) and 6.17(b), i.e., the former would require more activated voxels than the latter to achieve the same sensitivity score. It is thus expected that the sensitivity and *gmean* values for patient 2 (Table 6.2) would be very much smaller than those for patient 1 (Table 6.1). For patient 3, Fig. 6.17(e) (picture naming) shows hardly any activation near ON electrodes and thus the associated *gmean* value in Table 6.3 is small. Fig. 6.17(f) (patient 3-responsive naming) shows a fMRI cluster just under the top rightmost ON electrode, which, as expected, yielded a higher *gmean* value in Table 6.3 than for the fMRI map in Fig. 6.17(e).

Table 6.1: Current density weighted ECS-fMRI correspondence indices for picture naming, responsive naming and combined (OR operation) picture-responsive naming fMRI maps for **patient 1**. Approximate value of maximum possible gmean is 0.78.

fMRI Task	***TP***	***TN***	***FP***	***FN***	***accuracy***	***sensitivity***	***specificity***	***gmean***	***gmean (%)***
picture naming	0.41	14.95	0.27	5.56	0.73	0.07	0.98	0.26	33.33
responsive naming	0.07	15.18	0.04	5.89	0.72	0.01	1.00	0.11	14.10
combined	0.47	14.91	0.31	5.49	0.73	0.08	0.98	0.28	35.90

Table 6.2: Current density weighted ECS-fMRI correspondence indices for picture naming, responsive naming and combined (OR operation) picture-responsive naming fMRI maps for **patient 2**. Approximate value of maximum possible gmean is 0.80.

fMRI Task	***TP***	***TN***	***FP***	***FN***	***accuracy***	***sensitivity***	***specificity***	***gmean***	***gmean (%)***
picture naming	0	14.28	0	7.64	0.65	0	1.00	0.01	1.25
responsive naming	0.01	14.28	0.01	7.64	0.65	0	1.00	0.03	3.75
combined	0.01	14.28	0.01	7.64	0.65	0	1.00	0.03	3.75

Table 6.3: Current density weighted ECS-fMRI correspondence indices for picture naming, responsive naming and combined (OR operation) picture-responsive naming fMRI maps for **patient 3**. Approximate value of maximum possible gmean value is 0.80.

fMRI Task	***TP***	***TN***	***FP***	***FN***	***accuracy***	***sensitivity***	***specificity***	***gmean***	***gmean (%)***
picture naming	0.01	29.52	0.51	3.02	0.89	0	0.98	0.05	6.25
responsive naming	0.10	29.96	0.07	2.93	0.91	0.03	1.00	0.18	22.50
combined	0.10	29.46	0.58	2.92	0.89	0.03	0.98	0.18	22.50

The preceding comparisons of correspondence indices for fMRI maps from separate picture and responsive naming paradigms showed that the indices behaved in a manner consistent with notions of what constitutes good and bad ECS-fMRI correspondence. As shown in the use of

identical ECS ON electrode configurations for different fMRI paradigms in each patient in Fig. 6.17, the clinical ECS language maps show a combination of tasks, i.e., mapping of language tags using both picture and naming tasks. In these cases, it would be more accurate to first combine the picture naming and responsive naming fMRI maps using a logical OR operation, and then compute correspondence indices of the resultant combined fMRI map. This is computed for all three patients in the third rows of Tables 6.1 to 6.3. However, since our purpose was to demonstrate the application of the current density weighted indices on real data, and to compare different fMRI maps for the same patient and between different patients, it was more informative to analyze the correspondence indices for the separate fMRI maps (first and second rows of Tables 6.1 to 6.3) with the pictures in Fig. 6.17.

The class imbalance problem, discussed in the Methods section, is reflected in the relatively constant accuracy index values for each patient in Tables 6.1 to 6.3. For example, even though Fig. 6.17(a) exhibits better ECS-fMRI correspondence (qualitatively) than Fig. 6.17(b), the *accuracy* values are approximately the same in Table 6.3. This is because each patient's ECS map had many OFF electrode pairs that gave rise to larger numbers of true negatives compared to true positives, especially when only a few fMRI activation voxels are detected. Thus, the numerator of the accuracy measure in Eqn. 5 is dominated by *TN*, as observed in the large *TN* values in Tables 6.1 to 6.3, which makes the accuracy index relatively insensitive to small changes in *TP*. This makes the accuracy index less reliable for intra-patient ECS-fMRI correspondence comparisons with different fMRI activation maps.

The purpose of computing the proposed correspondence indices for three human datasets is to illustrate that the method can be applied to real data. It is not our intention, at this time, to make any statistical conclusions about ECS-fMRI validation based on the limited patient data available in this report. A more comprehensive statistical analysis of the current density weighted indices with multiple patients and different fMRI data correction/ processing methods is planned for future work.

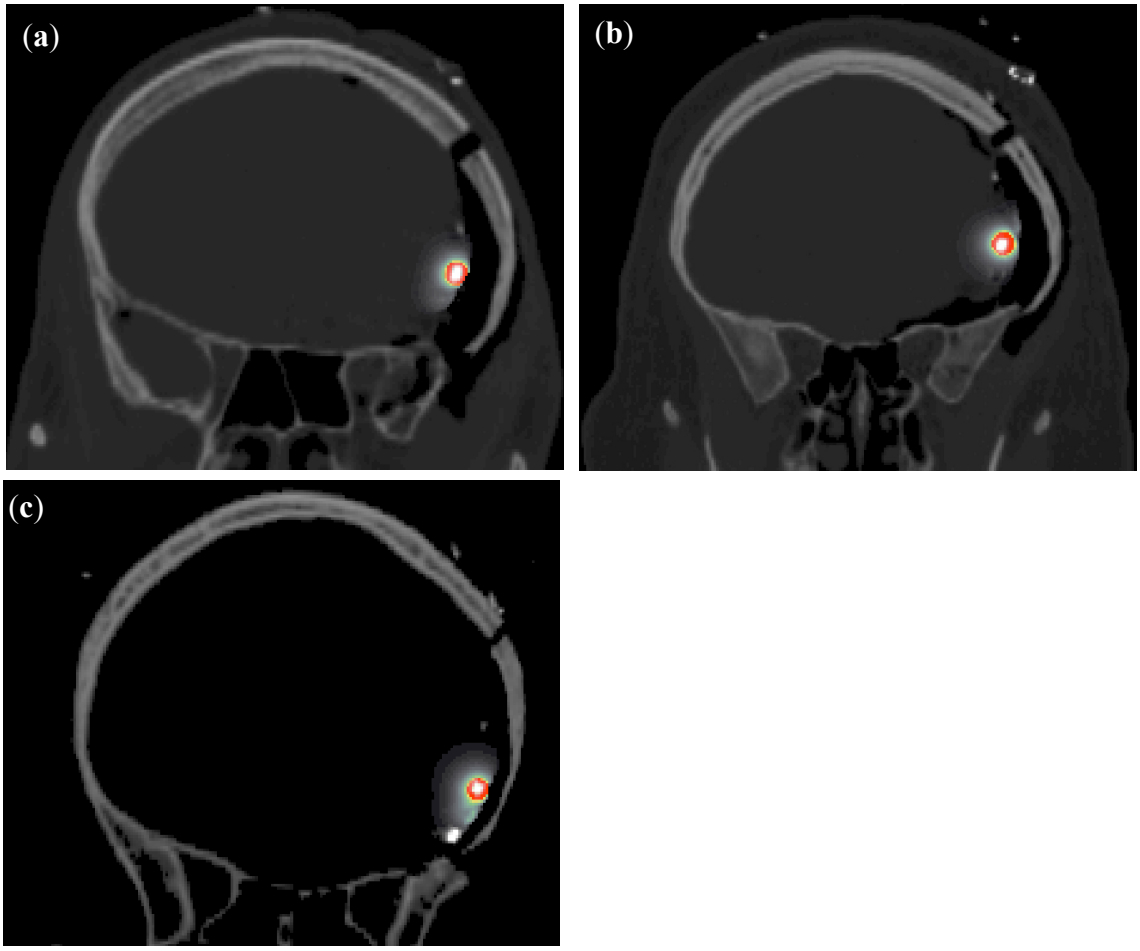

Figure 6.16: Coronal view of human CT datasets with overlaid current density maps (red indicates higher values) for (**a**) patient 1, (**b**) patient 2, and (**c**) patient 3. Each image shows the cross-sectional view of the current density distribution around one stimulated electrode (of a pair of them). The second electrodes of the stimulated pairs lie in different coronal slice planes and thus are not visible in these images. To calculate the current density weighted ECS-fMRI indices, the 3D current density distributions for each pair of stimulated ON and OFF electrodes were computed.

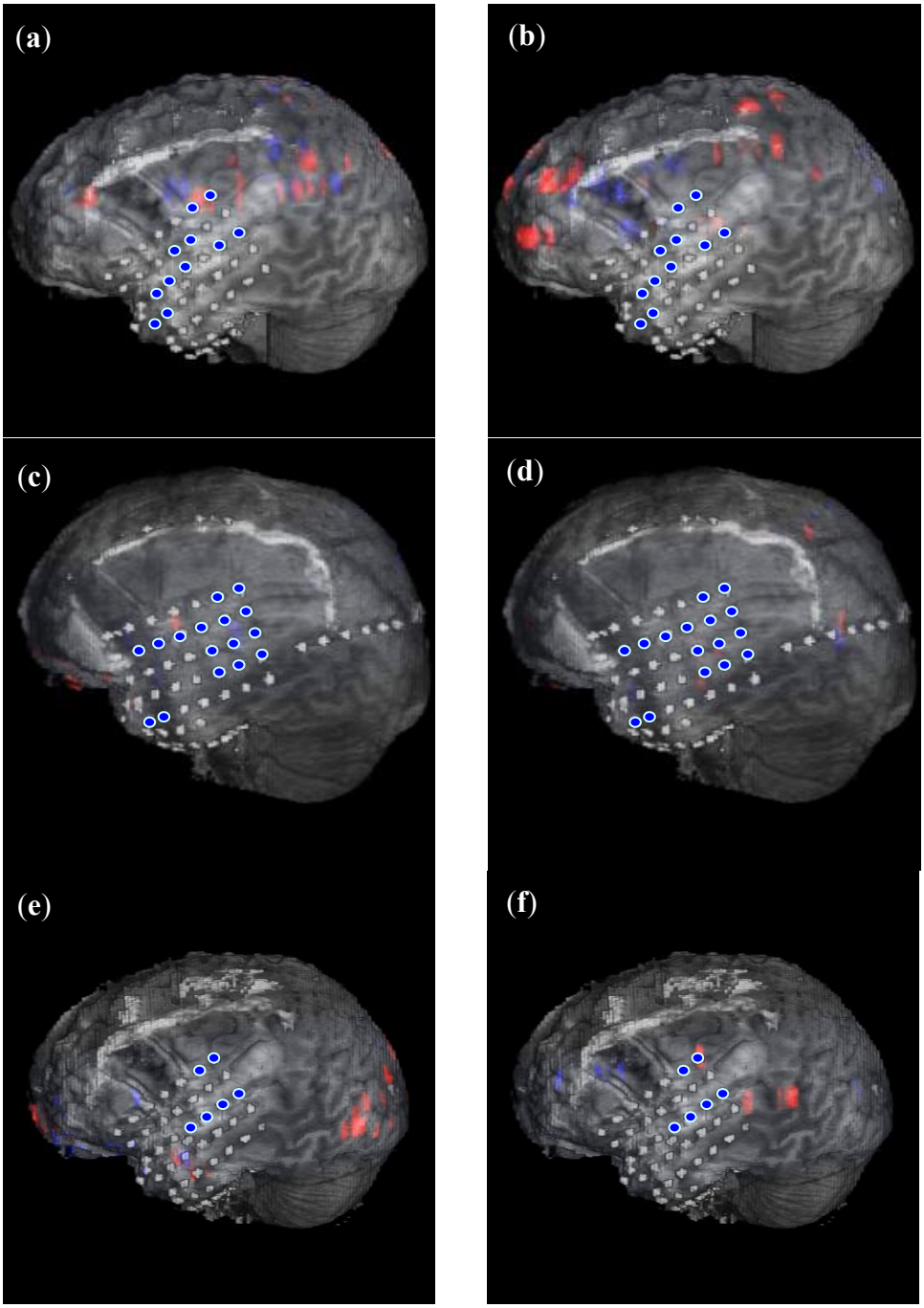

Figure 6.17: Composite 3D MR anatomical, CT electrode grid and fMRI activation datasets (red for positive fMRI activation) for (**a**) patient 1 picture naming task, (**b**) patient 1 responsive naming task, (**c**) patient 2 picture naming task, (**d**) patient 2 responsive naming task, (**e**) patient 3 picture naming task, and (**f**) patient 3 responsive naming task. Solid shaded dark blue circular tags on electrode grid denote ON electrodes.

6.4 Discussion

ECS, in itself, is a surface map of a limited area of the brain (under the electrode grid) and maps essential language regions while fMRI is a 3D functional map of the entire brain. Thus, it may not be accurate to compare an ECS surface map to 3D fMRI directly. The current density weighted method effectively extends the ECS surface map into a 3D map using electrostatic principles in electrical stimulation. It was shown with simulated data that the current density weighted sensitivity and *gmean* indices had higher values when fMRI activation voxels occur near ON electrodes, which is expected for good ECS-fMRI correspondence. Unlike the voxel-based fixed radii and Euclidean distance indices, the current density weighted indices were able to measure correspondence levels while taking into account contextual information such as the number of surrounding ON electrodes (Fig. 6.12(c)) as well as different electrode stimulus levels (Fig. 6.11(c)). Also, unlike the voxel-based fixed radii method, the current density weighted indices can track incremental improvements in ECS-fMRI correspondence when fMRI activated voxels, which are already near ON electrodes, move even closer to these ON electrodes. All these advantages were achieved without direct computation of Euclidean distances while taking into account variations in electrode grid and brain tissue geometry in the computation of the current density maps.

Simulated data were used to characterize the correspondence indices because they consist of fixed ECS and fMRI maps. If a real patient-task ECS map was chosen and fMRI activation locations were artificially shifted, the behavior of the indices with respect to activation location may be unnecessarily difficult to interpret because of the additional complexity in the 3D electrode grid and brain geometries. The simulation results of the current density weighted indices depended primarily on the current density magnitudes at different voxel locations. Thus, if a patient's current density map is computed accurately, the indices would exhibit similar characteristics as observed in the simulated data.

The proposed current density map indices can be used for intra-patient studies, and possibly for inter-patient comparisons as well, i.e., with *gmean(%)*. In future work, the current density weighted correspondence indices will be used to evaluate fMRI correspondence in a study involving a larger number of patients. In addition to ECS-fMRI validation in general, an ECS-fMRI correspondence index that incorporates contextual information provided by a given set of active/ inactive stimulated electrode pairs can be very useful when comparing data processing algorithms in fMRI, e.g., motion correction, activation detection. Functional MRI maps from different but relevant stimuli paradigms, or single paradigm fMRI datasets that are processed

differently, may be evaluated and compared for best ECS-fMRI correspondence. This can aid in the validation of fMRI data processing algorithms.

It is important to note that although fMRI and ECS are similar in function, they are not necessarily identical. This may explain why it is not likely that one would observe perfect ECS-fMRI correspondence for human data. In our patient data, the highest (relative to three patient datasets) current density weighted *gmean* and *gmean(%)* values (Table 6.1) are 0.26 and 35.9%, respectively. These values are large compared to the other two patients (Tables 6.2 and 6.3), but small relative to the maximum values attainable, i.e., 1.00 and 100.0% for *gmean* and *gmean(%)*, respectively. These relatively small values may have arisen from a combination of data processing errors, inconsistent patient response in fMRI tasks, and the inherent physiological differences in ECS and fMRI paradigms. The current density weighted indices may be used to investigate these individual issues in future work with more human data.

It should be noted that for true negative counts, the criteria with which OFF electrodes are defined may have an impact on computing the correspondence indices. In our simulations, the OFF electrodes were defined as stimulated electrodes that did not yield responses. Alternatively, OFF electrodes could be defined as stimulated electrodes that yielded non-function related responses [54]. For our validation purposes, the ECS stimulated electrode pairs that elicited motor or sensory responses have been classified as ON electrodes. Thus, verbalized language tasks, without further consideration of stimulus paradigm designs that activate only the language region, would show activations in motor, language or sensory areas. However, the definition of OFF electrodes does not affect the overall formulation of the current density weighted correspondence indices, which are of primary interest of this study.

The accuracy of numerically computed current density maps depends on the accuracy of electrodes and brain tissue geometries and the modeling of electrical conductivity within the brain. A more accurate way of modeling the complex brain geometry would be to use the finite element method (FEM) to compute the current density map, but at a much higher computational cost in terms of time and memory. Another approach to improving accuracy is to model the tensorial electrical conductivity of brain tissue using MR diffusion tensor imaging (DTI) data.

6.5 Conclusions

With simulated data, the current density weighted sensitivity, specificity and gmean indices were found to measure ECS-fMRI correspondence in a consistently predictable manner with expected notions of good and poor ECS-fMRI correspondence. These indices are more sensitive to incremental improvements in ECS-fMRI correspondence that were not detected by the voxel-

based fixed radii method. In addition, the current density weighted indices were able to reflect certain contextual information provided by surrounding electrodes. While the correspondence results computed for three human datasets were not sufficient to make conclusions about ECS-fMRI validation in general, they demonstrate the applicability of the current density correspondence method to analysis of human data. This work provides a systematic way to quantify 3D ECS-fMRI correspondence.

CHAPTER 7

Summary and Future Work

7.1 Summary

We developed an affine phase correction technique that facilitated the use of a dual-echo bipolar readout gradient protocol for motion robust static field map estimation. The zeroth order phase error term was found to be constant for a given MR scanner. The first order phase term varies across scanners, but can be approximated empirically. We also developed a concurrent motion and B_0 field inhomogeneity correction framework and evaluated it with simulated EPI time series data with known motion, geometric distortion and activation. Dynamic field maps were approximated by resampling a spatially transformed static field map. Empirical convergence of the algorithm was observed under the simulated conditions. However, the correction framework did not address field map changes due to large out-of-plane rotations. To address this challenge, we proposed a novel retrospective dynamic field map estimation technique by applying a quadratic penalized weighted least squares (QPWLS) approach to solve the inverse susceptibility voxel convolution problem. This is similar to regularized image restoration in image processing. In this work, our goal was to estimate a susceptibility map from a high resolution, noisy, susceptibility-induced field map. Rigid body motion was applied to the estimate and a new dynamic field map was computed using the forward susceptibility voxel convolution method. Compared with simpler image restoration algorithms such as thresholded inverse filtering and Wiener filtering, preliminary results with realistically simulated data suggest that the QPWLS method would yield the most accurate field map estimates, while requiring the least amount of object-specific prior information, e.g., object power spectra. In another separate project, we formulated a current density weighted approach to quantify the correspondence between subdural electrocortical stimulation (ECS) and fMRI maps for brain lesion presurgical planning. Detailed experiments were performed on simulated electrode grids and fMRI activation to characterize the

behavior of the index before the technique was applied to three patient datasets. The proposed index may provide a more systematic and physiologically correct way to quantify ECS-fMRI correspondence, as opposed to the commonly used Euclidean distance based methods.

7.2 Future Work

The following are several suggestions for future work:

- The SVC impulse response is similar to a finite difference operator in the z direction, i.e., it has a larger response to abrupt transitions of χ in the z direction than a constant χ. Thus, an edge preserving regularization function, e.g., Huber function, may be used in Chapter 5. This scheme favors smoothly varying susceptibility map estimates within soft tissue, air and bone regions while allowing for abrupt changes in χ at tissue interfaces.
- A potential limitation of the proposed method in Chapter 5 may arise because $\Delta\boldsymbol{\omega}_{sys}$ was ignored in Eq. (5.11). Methods to reliably measure this non-χ induced field inhomogeneity may be developed to facilitate the use of the proposed technique.
- The segmentation-SVC approach for dynamic field map estimation, as described in Chapter 5, should be implemented and its performance compared with the proposed QPWLS method.
- Upon validation, the proposed technique in Chapter 5 may replace the field map update stage in the CFMMSV framework of Chapter 4. The performance of the improved CFMMSV algorithm can then be evaluated with data of an MR phantom in motion.
- Having characterized the ECS-fMRI correspondence indices in Chapter 6 with simulated datasets, and having demonstrated clinical feasibility by applying them to three patient datasets, the indices should now be computed for a larger number of patients to assess clinical ECS-fMRI correspondence.

BIBLIOGRAPHY

BIBLIOGRAPHY

[1] Mansfield P. Multi-planar image formation using NMR spin-echoes. J. Phys. C: Solid State Phys. 1977;10:L55-L58.

[2] Jezzard P, Balaban RS. Correction for geometric distortion in echo planar images from B0 field variations. Magn Reson Med 1995;34:65-73.

[3] Kadah YM, Hu X. Algebraic reconstruction for magnetic resonance imaging under B0 inhomogeneity. IEEE Trans on Med Imaging 1998;17:362-370.

[4] Cusack R, Brett M, Osswald K. An evaluation of the use of magnetic field-maps to undistort echo-planar images. Neuroimage 2003;18:127-142.

[5] Sutton BP, Noll DC, Fessler JA. Fast, iterative image reconstruction for MRI in the presence of field inhomogeneities. IEEE Trans on Med Imaging 2003;22:178-188.

[6] Zeng H, Constable RT. Image distortion correction in EPI: Comparison of field mapping with point spread function mapping. Magn Reson Med 2002;48:137-146.

[7] Munger P, Crelier GR, Peters TM, Pike GB. An inverse problem approach to the correction of distortion in EPI images. IEEE Trans on Med Imaging 2000;19:681-689.

[8] Schomberg H. Off-resonance correction of MR images. IEEE Trans on Med Imaging 1999;18:481-495.

[9] Roopchansingh V, Cox RW, Jesmanowicz A, Ward BD, Hyde JS. Single-shot magnetic field mapping embedded in echo-planar time-course imaging. Magn Reson Med 2003;50:839-843.

[10] Sutton BP, Noll DC, Fessler JA. Dynamic field map estimation using a spiral-in/spiral-out acquisition. Magn Reson Med 2004;51:1194-1204.

[11] Yeo DTB, Chenevert TL, Fessler JA, Kim B. Zero and First Order Phase Shift Correction for Field Map Estimation with Dual-Echo GRE Using Bipolar Gradients. Magn Reson Imag 2007;25:1263-1271.

[12] Chen N, Oshio K, Panych LP. Application of k-space energy spectrum analysis to susceptibility field mapping and distortion correction in gradient-echo EPI. Neuroimage 2006;31:609-622.

[13] Yeo DTB, Fessler JA, Kim B. Concurrent Correction of Geometric Distortion and Motion Using the Map-Slice-to-Volume Method in Echo-Planar Imaging. Magn Reson Imag 2008 (In Press).

[14] Schneider E, Glover G. Rapid in vivo proton shimming. Magn Reson Med 1991;18:335-47.

[15] Park H, Kim Y, Cho Z. Fast gradient-echo chemical-shift imaging. Magn Reson Med 1988;7:340-45.

[16] Webb P, Macovski A. Rapid, fully automatic, arbitrary-volume in vivo shimming. Magn Reson Med 1991;20:113-22.

[17] Fessler JA, Yeo DTB, Noll DC. Regularized Fieldmap Estimation in MRI. In: Proceedings of IEEE International Symposium of Biomedical Imaging (ISBI). p. 706-709, 2006.

[18] Reber PJ, Wong EC, Buxton RB, Frank LR. Correction of off-resonance-related distortion in echo-planar imaging using EPI-based field maps. Magn Reson Med 1998;39:328-30.

[19] Thilaka S, Sumanaweera TS, Glover GH, Binford TO, Adler JR. MR susceptibility misregistration correction. IEEE Trans on Med Imaging 1993;12:251-259.

[20] Haacke EM, Brown RW, Thomson MR, Venkatesan R, Magnetic resonance imaging: physical principles and sequence design. New York: Wiley-Liss; 1999.

[21] Hutton C, Bork A, Josephs O, Deichmann R, Ashburner J, Turner R. Image distortion correction in fMRI: a quantitative evaluation. Neuroimage 2002;16;217-240.

[22] Poncelet BP, Wedeen VJ, Weisskoff RM, Cohen MS. Brain parenchyma motion: measurement with cine echoplanar MR imaging. Radiology 1992;185:645-651.

[23] Vajda I. Theory of Statistical Inference and Information, Dordrecht, Netherlands: Kluwer; 1989.

[24] Meyer CR, Boes JL, Kim B, Bland PH, et al. Demonstration of accuracy and clinical versatility of mutual information for automatic multimodality image fusion using affine and thin plate spline warped geometric deformations. Medical Image Analysis 1997;1:195-206.

[25] Kim B, Boes JL, Bland PH, Chenevert TL, Meyer CR. Motion correction in fMRI via registration of individual slices into an anatomical volume. Magn Reson Med 1999;41:964-972.

[26] Yeo DTB, Bhagalia RR, Kim B. Improved Map-Slice-to-Volume Motion Correction with B0 Inhomogeneity Correction: Validation of Activation Detection Algorithms Using ROC Curve Analyses. In: Larsen R, Nielsen M, Sporring J, eds. Medical Image Computing and Computer-Assisted Intervention. Lecture Notes in Computer Science 4191:276-283. Springer Verlag;2006.

[27] Wirestam R, Salford LG, Thomsen C, Brockstedt S, Persson BRR, Stahlberg F. Quantification of low-velocity motion using a navigator-echo supported MR velocity-mapping technique: Application to intracranial dynamics in volunteers and patients with brain tumours. Magn Reson Imag 1997;15(1):1-11.

[28] Ghiglia DC, Pritt MD. Two-dimensional phase unwrapping: Theory, algorithms, and software. Wiley: New York; 1998.

[29] Cusack R, Papadakis N. New robust 3-D phase unwrapping algorithms: Application to magnetic field mapping and undistorting echoplanar images. Neuroimage 2002;16:754-64.

[30] Friston KJ, Ashburner J, Frith CD, Poline JB, Heather JD, Frackowiak RSJ. Spatial registration and normalization of Images. Hum Brain Map 1995;2:165–189.

[31] Bullmore E, Brammer M, Williams SCR, Rabe-Hesketh S, Janot N, David A, Meller J, Howard R, Sham P. Statistical methods and estimation and inference for functional MR image analysis. Magn Reson Med 1996;35:261–277.

[32] Hu X, Le TH, Parrish T, Erhard P. Retrospective estimation and correction of physiological fluctuation in functional MRI. Magn Reson Med 1995;34:201–212.

[33] Hajnal JV, Myers R, Oatridge A, Schwieso JE, Young IR, Bydder GM. Artifacts due to stimulus correlated motion in functional imaging of the brain. Magn Reson Med 1994;31:283–291.

[34] Andersson JLR, Hutton C, Ashburner J, Turner R, Friston K. Modeling geometric deformations in EPI time series. Neuroimage 2001;13:903-919.

[35] Jezzard P, Clare S. Sources of distortion in functional MRI data. Human Brain Mapping 1999;8:80-85.

[36] Andersson JLR, Skare S, Ashburner J. How to correct susceptibility distortions in spin-echo echo-planar images: application to diffusion tensor imaging. Neuroimage 2003;20:870-888.

[37] Chang H, Fitzpatrick JM. A technique for accurate magnetic resonance imaging in the presence of field inhomogeneities. IEEE Trans on Med Imaging 1992;11:319-329.

[38] Kim B, Bland PH, Meyer CR. Correction of local deformations in fMRI by 3D non-linear warping in map-slice-to-volume approach. In: Proceedings of the 7th Annual Meeting of ISMRM, Philadelphia, USA, 2000. p 1765.

[39] Kim B, Chenevert TL, Meyer CR. Motion correction with a non-linear warping solution for activations in temporal region. In: Proceedings of the 10th Annual Meeting of ISMRM, Honolulu, USA, 2002. p 2304.

[40] Nichols TE, Holmes AP. Nonparametric permutation tests for functional neuroimaging: A primer with examples. Hum Brain Map 2002;15:1-25.

[41] Good P. Permutation tests. New York: Springer-Verlag; 1994.

[42] de Munck JC, Bhagwandien R, Muller SH, Verster FC, Van Herk MB. The computation of MR image distortions caused by tissue susceptibility using the boundary element method. IEEE Trans on Med Imaging 1996;15:620-627.

[43] Truong TK, Clymer BD, Chakeres DW, Schmalbrock P. Three-dimensional numerical simulations of susceptibility-induced magnetic field inhomogeneities in the human head. Magn Reson Imag 2002;20:759-770.

[44] Yoder DA, Zhao Y, Paschal CB, Fitzpatrick JM. MRI simulator with object-specific field map calculations. Magn Reson Imag 2004;22:315-328.

[45] Lim JS. Two-dimensional signal and image processing. New Jersey: Prentice Hall; 1990.

[46] J A Fessler, Image Reconstruction Toolbox, 2007. Available from http://www.eecs.umich.edu/~fessler.

[47] Ojemann G, Sutherling W, Lesser R, Dinner D, Jayakar P, Saint-Hilaire J. Cortical stimulation. In Engel J Jr. (Ed) Surgical Treatment of the Epilepsies. New York: Raven Press; 1993.

[48] Møller AR. Intraoperative Neurophysiological Monitoring. New Jersey: Humana Press; 2006.

[49] Nathan SS, Sinha SR, Gordon B, Lesser RP, Thakor NV. Determination of current density distributions generated by electrical stimulation of the human cerebral cortex. Electroencephalography and Clinical Neurophysiology 1993;86:183-192.

[50] Hill DLG, Smith ADC, Simmons A, Maurer CR Jr., Cox TCS, Elwes R, Brammer M, Hawkes DJ, Polkey CE. Sources of error in comparing functional magnetic resonance imaging and invasive electrophysiological recordings. J Neurosurg 2000;93:214-223.

[51] Krings T, Schreckenberger M, Rohde V, Spetzger U, Sabri O, Reinges MHT, Hans FJ, Meyer PT, Möller-Hartmann W, Gilsbach JM, Buell U, Thron A. Functional MRI and 18F FDG-positron emission tomography for presurgical planning: Comparison with electrical cortical stimulation. Acta Neurochir 2002;144:889-899.

[52] Pirotte B, Neugroschl C, Metens T, Wikler D, Denolin V, Voordecker P, Joffroy A, Massager N, Brotchi J, Levivier M, Baleriaux D. Comparison of functional MR imaging guidance to electrical cortical mapping for targeting selective motor cortex areas in neuropathic pain: A study based on intraoperative stereotactic navigation. Am J Neuroradiol 2005;26:2256-2266.

[53] O'Shea JP, Whalen S, Branco DM, Petrovich NM, Knierim KE, Golby AJ. Integrated image- and function-guided surgery in eloquent cortex: a technique report. The Intl Journal of Medical Robotics and Computer Assisted Surgery 2006;2:75-83.

[54] FitzGerald DB, Cosgrove GR, Ronner S, Jiang H, Buchbinder BR, Belliveau JW, Rosen BR, Benson RR. Location of language in the cortex: A comparison between functional MR imaging and electrocortical stimulation. Am J Neuroradiol 1997;18:1529-1539.

[55] Kubat M, Holte RC, Matwin S. Machine learning for the detection of oil spills in satellite radar images. Machine Learning 1998;30:195–215.

[56] Hastie T, Tibshirani R, Friedman J. The Elements of Statistical Learning: Data Mining, Inference, and Prediction. New York : Springer-Verlag; 2001.

[57] Ojemann GA, Creutzfeldt OD, Lettich E. Neuronal activity in human temporal cortex related to naming and short-term verbal memory. In Engle J Jr, (Ed) Fundamental Mechanisms of Human Brain Function. New York: Raven Press pp. 61-68; 1987.

[58] Yeo DTB, Meyer CR, Parent JM, Minecan DN, Sagher O, Kluin KJ, Kim B. Formulation of current density weighted indices for correspondence between fMRI and electrocortical stimulation maps. In: Proceedings of the 16th Scientific Meeting of International Society for Magnetic Resonance in Medicine (ISMRM), Toronto, Canada, 2008.